STRUCTURE OF THE EARTH'S CORE AND LOWERMOST MANTLE FROM SEISMIC PKP WAVES

Thesis by

Xiaodong Song

In Partial Fulfillment of the Requirements

for the Degree of

Doctor of Philosophy

California Institute of Technology

Pasadena, California

1994

(Submitted May 18, 1994)

Acknowledgements

I am grateful to the Seismo Lab for having me and to Run Run Shaw Foundation, Don Helmberger (NSF grants), and the lab (Clarence Allen) for supporting me during my entire stay here. It's been an incredible and rewarding experience. Caltech is a great institution.

I thank my thesis advisor, Don Helmberger for advice, encouragement, inspiration and extreme patience with me. Don provided help that in no way could I ask for more.

The knowledge, wisdom and enthusiasm of the faculty is my constant source of inspiration. Thanks to Don Anderson for commenting on every one of our papers and forcing me to think seismology in broad context, Tom Ahrens for sharing his impression on China with me, Toshiro Tanimoto for many stimulating discussions, Hiroo Kanamori for bringing all those seismograms to the Coffee Break, Rob Clayton for introducing Kernighan and Richie's C to me at the first day of my arrival at the lab, Dave Harkrider for the stories back in the Old Days, Leon Silver and Bob for encouragement and for showing me what geology is all about, Yuk Young for alerting me to the societal aspect of science, Don Anderson and Clarence Allen for serving as my academic advisors and, Don Helmberger also, for giving me the liberty of

To *My Parents*

VIII

Abstract

Xiaodong Song, Ph.D.

California Institute of Technology 1994

This thesis addresses the fine structure, both radial and lateral, of compressional wave velocity and attenuation of the Earth's core and the lowermost mantle using waveforms, differential travel times and amplitudes of PKP waves, which penetrate the Earth's core.

The structure near the inner core boundary (ICB) is studied by analyzing waveforms of a regional sample. The waveform modeling approach is demonstrated to be an effective tool for constrainning the ICB structure. The best model features a sharp velocity jump of of 0.78km/s at the ICB and a low velocity gradient at the lowermost outer core (indicating possible inhomogeneity) and high attenuation at the top of the inner core.

A spherically symmetric P-wave model of the core, is proposed from PKP differential times, waveforms and amplitudes. The ICB remains sharp with a velocity jump of 0.78km/s. A very low velocity gradient at the base of the fluid core is demonstrated to be a robust feature, indicating inhomogeneity is practically inevitable. The model also indicates that the attenuation in the inner core decreases with depth. The

velocity at D'' is smaller than PREM.

The inner core is confirmed to be very anisotropic, possessing a cylindrical symmetry around the Earth spin axis with the N-S direction 3% faster than the E-W direction. All of the N-S rays through the inner core were found to be faster than the E-W rays by 1.5 to 3.5s. Exhaustive data selection and efforts in insolating contributions from the region above ensure that this is an inner core feature.

The anisotropy at the very top of the inner core is found to be distinctly different from the deeper part. The top 60km of the inner core is not anisotropic. From 60km to 150km, there appears to be a transition from isotropy to anisotropy.

PKP differential travel times are used to study the P velocity structure in D''. Systematic regional variations of up to 2s in AB-DF times were observed, attributed primarily to heterogeneities in the lower 500km of the mantle. However, direct comparisons with tomographic models are not successful.

Table of Contents

List of Figures

List of Tables

Chapter 1

Introduction

The fact that the vast bulk of the Earth is completely inaccessible to direct sampling puts seismology in a unique position in studying the internal structure of the Earth. The inference about the composition and physical state of the Earth interior is critically dependent on the accurate assessment of seismic parameters (velocity, attenuation and density), which is, in turn, critical to our ultimate understanding of the dynamics and the evolution of the planet. The principal features of the Earth internal structure were rapidly discovered and characterized in the first part of this century of the beginning era of seismology, primarily due to the pioneering works by Wiechert, Oldham, Gutenberg, Jeffreys, Lehmann, Bullen and Birch. By the year 1939, *Jeffreys* [1939a,b] had developed an Earth model, which is still used as a standard reference today (known as JB table from a later summary by *Jeffrey and Bullen* [1940]). However, significant improvement has been made, notably in two aspects. One aspect is the identification of a number of discontinuities and modification of velocity gradients in the upper mantle where a series of mineral phase changes have been identified. The other aspect is the recognition and mapping of

1

significant aspherical structure at all depths: large scale lateral variations in the upper mantle (can be linked to surface geology), sizable velocity discontinuity and heterogeneity in the lowermost mantle, and anisotropy in the inner core just recently revealed. Three-dimensional models (velocity and attenuation) of both regional and global scales have been generated. These results, coupled with experimental advances in near real Earth conditions (high pressure and temperature), have shaped and reshaped our knowledge and views on the constitution and the dynamics of the Earth.

This thesis is a continuing effort to refine the structure (P-wave velocity and attenuation) of the Earth's inner core (solid), outer core (fluid) and the lowermost mantle, both radially and laterally, from seismic body waves PKP, which penetrate the Earth's core.

Our data set primarily consists of waveforms, differential travel times and amplitude ratios of the PKP phases. Since the branches of PKP phases are very close together in the upper mantle, these relative observations allow us to isolate contributions in the lower mantle and the core from the potential biases from the source, receiver and upper mantle structure For PKP notation, raypaths, travel time curves, see section 2.3, Figure 3.1 and Figure 3.2. We adopt a forward modeling approach, a trial-and-error procedure. We are greatly aided in this approach by the development of techniques in synthesizing seismograms (Chapter 2). The waveform modeling approach, as described in Chapter 2, is an important tool in this thesis because of its higher resolution compared with traditional travel time and amplitude analysis. It is essential in describing diffraction and attenuation phenomena and critical in defining structure near a discontinuity because of propagational effects. A typical

problem of this kind is determining the sharpness of the boundary and velocity gradients near the boundary, such as the inner core boundary (ICB) investigated in this thesis. Competing models are often used in a same study in the thesis. They not only provide clues to what structure controls what part(s) of seismograms, but also can serve as a measure of uncertainties since statistical analysis on waveform fitting is virtually impossible.

The main body of the thesis is divided into five chapters. Although all of the chapters can stand as their own, they are mutually related. They contain the same kind of data set (PKP waveforms, travel times, amplitudes). For any observation we have at the surface, it includes contributions from all the elements along the ray path from different depths. Thus, not until we can isolate or at least estimate contributions from each element, can we resolve the deep structure of the Earth with certain confidence. This is particular true for core phases because of the trade-off between mantle contributions and core contributions. This point is reiterated, but more specifically, in the following discussion. The following is an overview on each chapter. The focus is not on presenting summaries of results, which can be found in each individual chapter, but on conveying the motivations, methodology, and limitations, along with major results and their implications.

Chapter 2 presents results near the ICB from modeling both long-period (20s) and short-period (1s) waveforms of a regional sample. The problem on the velocity structure near the ICB is a classical one. Soon after the inner core was discovered by Lehmann in 1936, two Earth models were proposed by *Gutenberg and Richter* [1938] and *Jeffreys* [1939a], independently, which included an inner core. For an account and discussion of the early models, see for example, *Bullen and Bolt* [1985], *Birch* [1952],

Brush [1980], *Bolt* [1982, 1987]. The biggest difference between the two competing models is near the ICB. Gutenberg and Richter favored a transitional boundary with a gradual velocity increase while Jeffreys favored a sharp discontinuity but with a decrease of velocity just above the discontinuity. Improvement was made in the later years but the nature of the boundary remains controversial (see a review by *Bolt* [1982] and introduction in Chapter 2). Our choice of a regional sample is deliberate. This is made so that only one sample of the Earth is obtained since the Earth is clearly aspherical. In this study, the waveform modeling approach, which involves discriminating models and readjusting model parameters, is demonstrated to be a valuable tool in determining the structure of the ICB. The study provides a sound base of methodology, which is largely followed in the entire thesis work. For this particular sample, the best model features a sharp P velocity jump of 0.78 km/s at the ICB, a low velocity gradient at the lowermost outer core, and high attenuation at the top of the inner core. The low velocity gradient indicates possible inhomogeneity at the base of the outer core following *Bullen*'s calculation [1963].

The above study is extended in Chapter 3 to derive a spherically symmetric average P velocity model of the core from added global samples using differential travel times, amplitude ratios of the PKP phases as well as waveform modeling techniques at a distance range of 130° to 165°. The proposed model, PREM2, is based on PREM [*Dziewonski and Anderson*, 1981] with major revisions near the ICB and the core-mantle boundary (CMB). A very low velocity gradient at the base of the fluid core (nearly constant over lower 100km) is demonstrated to be a robust feature from fitting the differential travel times, amplitude ratios and waveforms of BC or BC_{diff}, highly sensitive to the gradient, and DF phases. This result indicates that

inhomogeneity at the base of the outer core is practically inevitable. The model also features a strong depth dependent Q-structure in the inner core that the attenuation decreases monotonically with depth. Of all the PKP branches, AB is most susceptible to velocity variations in the lowermost mantle since it grazes the region the most. The velocity of PREM in the D'' is reduced to fit the average of $AB - DF$ and $AB - BC$ differential times, but with a notion that D'' is so varying that it can hardly be represented by a spherically symmetric model.

While we were concerning about small deviations near the ICB, evidence for large amplitude of anisotropy in the inner core emerged, which is presented in Chapter 4. In a systematic search, all of the paths traveling in the North-South direction in the inner core were found to be 1.5s to 3.5s faster than the East-West paths from every observation: differential travel times, absolute travel times, short-period waveforms (1s) and long-period waveforms (20s). Exhaustive data selection and tremendous efforts in insolating contributions from the mantle and outer core is made to ensure this is a feature of the inner core. The presence of anisotropy in the inner core is now well established. But the fact that it took more than half a century to identify this prominent feature of the inner core clearly demonstrates: (1) Our ability of mapping the internal structure of the Earth is critically limited by the adequacy of our data. In this case, the only way to get polar samples is from events at high latitudes in the southern hemisphere to stations at high latitudes in the northern hemisphere or vice versa. Samples like these are of course rare because of station and earthquake distributions. (2) Our ability is further limited by the complex trade-off between various parts that contribute to the signals, such as arrival times, that we observed at the surface. It is believed that the inner core is primarily made of anisotropic iron

crystals (hexagonally close-packed ε-iron) [*Jephcoat and Olson*, 1987; *Jeanloz*, 1990]. The inner core anisotropy has been proposed to result from the lattice preferred orientation of this ε-iron due to plastic deformation [*Jeanloz and Wenk*, 1988] or the solidification of iron in the presence of a magnetic field [*Karato*, 1993]. The later study, if true, would predict a strong toroidal magnetic field in the core.

Chapter 5 is an extension of the last chapter to include data from wider distance ranges to define the depth dependence of the inner core anisotropy. Particular attention is focused on the top 150km of the inner core. This region is difficult to resolve from travel times but can be adequately constrained by waveform analyses. The top 60km of the inner core is found, surprisingly, to be not anisotropic at all. From 60km to 150km, there appears to be a transition from isotropy to anisotropy. The immediate implication is the process, whatever that is, responsible for the inner core anisotropy is prevented at the very top for some reasons. This distinction between the very top of the inner core and the rest of it might have important bearing on the constitution and the formation of the inner core to be investigated.

Chapter 6 examines the impact of the lowermost mantle (D'') structure on the PKP phases. The purpose is twofold. Firstly, it provides a sensitivity study of using PKP differential travel times to map the lateral variations of P velocity in D''. Secondly, to constrain the structure of the core, all the elements above it that contribute to the observations must be understood, including effects from three-dimensional velocity structure. Systematic regional variations of up to 2s in AB − DF times were observed (same data set as in Chapter 3), which are attributed primarily to heterogeneities in the lower 500km of the mantle. However, direct corrections from tomographic models do not reduce data scatter, casting doubts on the practice of

using body waves to examine core anomalies after the "removal" of mantle anomalies from tomographic models. The ability of mapping out three-dimensional structure in the lowermost mantle, again, critically depends on the adequacy of the data. With the rapid development of global and regional seismic digital networks, it is foreseeable that higher resolution images of the lowermost mantle will come in the near future.

In all of the studies above, constraints are primarily on the P-wave velocity and attenuation although there's direct trade-off between attenuation and S-wave velocity (see discussion in Chapter 2). S velocity and density are assumed (from PREM) because of the lack of sensitivity of our data (see discussion in Chapter 2). The best constraints on the S velocity in the inner core and density in the inner core and outer core still come from free-oscillation data, although there are few body wave studies. For recent reviews on the subject, see *Masters and Shearer* [1990], *Masters* [1991].

The material presented in this thesis has been either published or submitted for publications, with some modification. Chapter 2, 3, 4, 5, 6 can be found in *Song and Helmberger* [1992, 1994a, 1993b, 1994b, 1993a], respectively.

8

Chapter 2

Velocity Structure Near the Inner Core Boundary From Waveform Modeling

2.1 Abstract

A velocity model of the inner core boundary (ICB) region is developed from broadband waveform modeling. The data consist of long period and short period record sections gathered from the U.S. arrays, WWSSN, and LRSM. Deep events beneath Indonesia were used; these sampled the ICB structure beneath the North Pacific. The Cagniard-de Hoop technique was used to generate the synthetics, which allowed considerable flexibility in forward modeling these individual PKP phases. Our preferred model was developed from modifications of the Preliminary Reference Earth Model (PREM). It contains a relatively low velocity gradient above the ICB, a sharp jump at the ICB of about 0.78 km/s, and a relatively large gradient underneath. These features are constrained largely by the differential travel times and amplitude ratios of PKIKP and PKiKP of the short period section. Further modification of

PREM in the fluid core was required to explain the long-period observations associated with PKP waveforms. Our modeling results suggest a low-velocity gradient at the bottom (roughly 400 km) of the fluid core. A low Q zone at the top of the inner core is required to fit the relative amplitudes of PKIKP phases similar to earlier studies. This model indicates possible inhomogeneity above the ICB, as suggested by other authors.

2.2   Introduction

The nature of the inner core boundary (ICB) has remained controversial since its discovery in 1936 [*Lehmann*, 1936]. The only direct information about the structure near the boundary comes from seismic waves. However, interpretations of observations by various authors differ significantly. Figure 2.1 shows a collection of proposed P-wave velocity models, which were derived mainly from two categories of data: (1) travel time data and/or free oscillation data, such as *Jeffreys* [1939a,b], C2 [*Anderson and Hart*, 1976], Parametric Earth Models (PEM) [*Dziewonski et al.*, 1975], and Preliminary Reference Earth Model (PREM) [*Dziewonski and Anderson*, 1981]; (2) a combination of waveform and travel time data, such as M2 [*Müller*, 1973] and KOR5 [*Qamar*, 1973]. *Bolt*'s [1962,1964] transition zone model was proposed to explain the short-period precursors to PKIKP. The key issues have been the sharpness of the boundary, the velocity jump at the boundary, the velocity gradient above and below the boundary, the Q structure near the boundary, the frequency dependence of the radius of the inner core, and the density jump at the boundary. The variety of models displayed indicates the richness of possible interpretations.

It appears that the most detailed resolution of this discontinuity will come from

Figure 2.1: P velocity models of the Earth's core previously proposed: *Jeffreys* [1939a,b], C2 [*Anderson and Hart*, 1976], PEM [*Dziewonski et al.*, 1975], PREM [*Dziewonski and Anderson*, 1981], M2 [*Müller*, 1973], KOR5 [*Qamar*, 1973], and model by *Bolt*'s [1962,1964].

Models of Earth Core

the waveform modeling approach which will be followed in this study. This basic method relies on fitting observations with synthetics based on a model where the wave equations are satisfied. The earliest ideas about this subject can be traced back to *Lamb* [1904]. The method experienced rapid development in the 1960s and 1970s and has been used in modeling the fine structure and anelasticity of the Earth at all depths; see *Richards* [1985] for a historical review of the development and practice of numerical modeling.

For the ICB case, there are a few excellent theoretical waveform modeling studies which examine a few seismograms at key distances, essentially sensitivity studies. Most of these efforts implicitly assume a one-dimensional Earth in that paths from events to various continents are typically folded into the same record section. However, recent travel time studies indicate that the lower mantle, and perhaps the core as well, is heterogeneous [*Poupinet et al.*, 1983; *Morelli et al.*, 1986; *Creager and Jordan*, 1986; *Cormier and Choy*, 1986; *Souriau and Poupinet*, 1990; *Shearer and Toy*, 1991]. Thus, it is clear that the deep structure of the Earth is not spherical and must be sampled accordingly. Thus, we will undertake a regionalization analysis with a detailed investigation of a particular sample of the lower mantle and core. To this end, we assembled waveform profiles across the United States for events beneath Indonesia, including a long-period WWSSN section and a short-period LRSM section.

There are several disadvantages to using this approach, namely, the need to digitize records and the general inferior quality of the timing resolution. Fortunately, there are more advantages. First, by modeling a record section, we are able to use the same source function and do not need to be concerned with uncertainties of source

location, origin time, source duration, etc. Second, both the take-off angles and azimuths are confined to a few degrees so that the radiation pattern and path complexities are common to all the data. By modeling the short-period and long-period waveforms simultaneously we can place strong constraints on the structure.

The purpose of this paper is to examine these constraints on the velocity structure near the ICB by modeling these waveforms. As a result, a new model, PMNA, is proposed, which is compared with PREM and PEM in Figure 2.2. The P velocity parameters are given in Table 2.1. The S velocity, density in the core, and all the parameters in the mantle are assumed from PREM. Our preferred model contains a very small gradient above the ICB, and a gradient underneath the ICB larger than PEM and PREM with a sharp jump of 0.78 km/s at the ICB. In the following, we first present the method and the data we used. Then, we show our waveform modeling results. This will be followed by a comparison of our results with some previous modeling studies.

2.3 Cagniard-de Hoop Method and Notation

Most of the waveform techniques applied to the core phases are based on an asymptotic method proposed by *Richards* [1973] and discussed at length in *Aki and Richards* [1980]. Synthetics from this approach have been checked against reflectivity synthetics from Earth-flattened models and found to be quite satisfactory [*Müller*, 1973]. Synthetics based on still another approach using generalized rays and the Cagniard-de Hoop method are displayed in Figure 2.3.

This broadband section from 132° and 152° shows all the major branches of core phases. They are phases going through the top of the outer core, PKP-AB or simply

15

Figure 2.2: Comparisons of three P velocity models used in construction of synthetics. Model PMNA fits the short- and long-period waveform data better than two reference models.
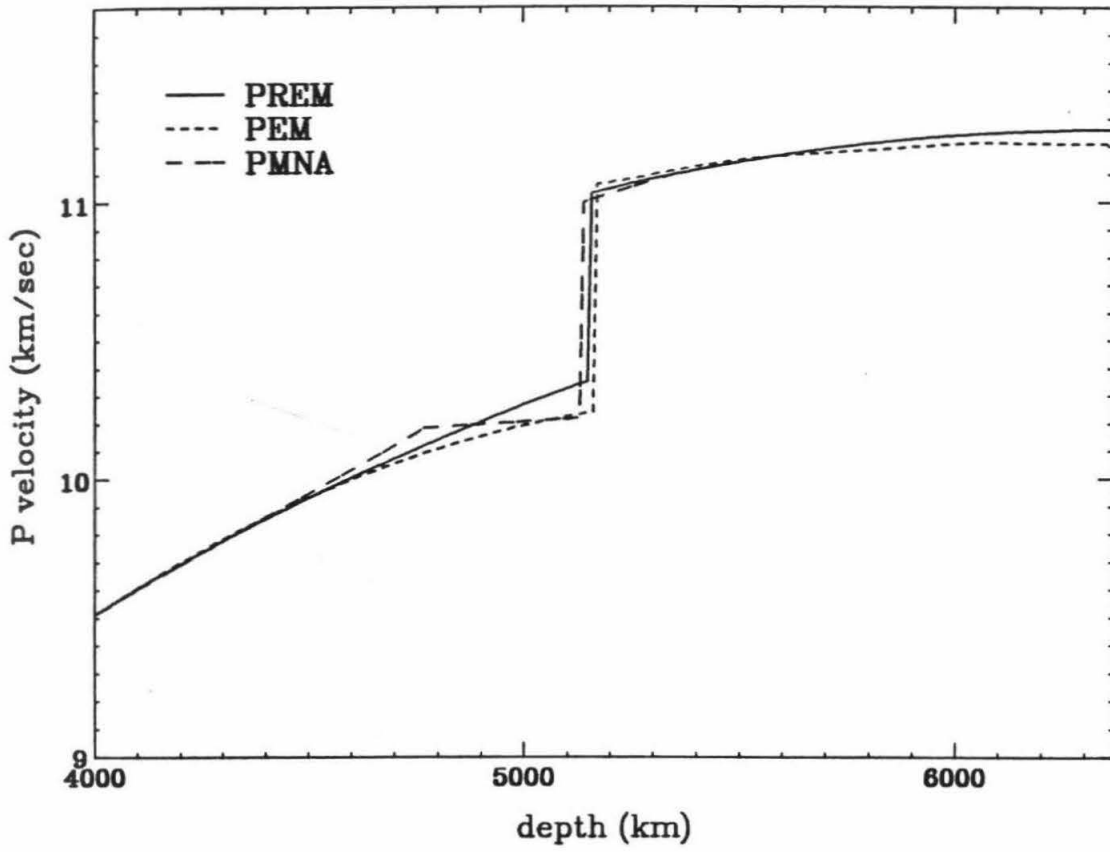
Table 2.1. P Velocity Parameters of the Proposed Earth Core Model (PMNA)

Radius, km	V_p, km/s	Radius, km	V_p, km/s	Radius, km	V_p, km/s	Radius, km	V_p, km/s
0.0	11.26219	400.0	11.23696	800.0	11.16156	1200.0	11.01437
10.0	11.26211	410.0	11.23569	810.0	11.15905	1210.0	11.00958
20.0	11.26201	420.0	11.23438	820.0	11.15651	1220.0	11.00479
30.0	11.26188	430.0	11.23304	830.0	11.15393	1230.0	11.00000
40.0	11.26173	440.0	11.23167	840.0	11.15133	1230.0	10.22000
50.0	11.26155	450.0	11.23027	850.0	11.14870	1240.0	10.21906
60.0	11.26135	460.0	11.22884	860.0	11.14603	1250.0	10.21811
70.0	11.26113	470.0	11.22737	870.0	11.14333	1260.0	10.21717
80.0	11.26087	480.0	11.22587	880.0	11.14061	1270.0	10.21622
90.0	11.26059	490.0	11.22434	890.0	11.13785	1280.0	10.21528
100.0	11.26029	500.0	11.22278	900.0	11.13505	1290.0	10.21434
110.0	11.25995	510.0	11.22119	910.0	11.13223	1300.0	10.21339
120.0	11.25959	520.0	11.21957	920.0	11.12938	1310.0	10.21245
130.0	11.25920	530.0	11.21791	930.0	11.12649	1320.0	10.21151
140.0	11.25878	540.0	11.21622	940.0	11.12357	1330.0	10.21056
150.0	11.25833	550.0	11.21450	950.0	11.12062	1340.0	10.20962
160.0	11.25785	560.0	11.21275	960.0	11.11763	1350.0	10.20867
170.0	11.25734	570.0	11.21097	970.0	11.11461	1360.0	10.20773
180.0	11.25681	580.0	11.20916	980.0	11.11156	1370.0	10.20679
190.0	11.25624	590.0	11.20732	990.0	11.10848	1380.0	10.20584
200.0	11.25564	600.0	11.20544	1000.0	11.10536	1390.0	10.20490
210.0	11.25501	610.0	11.20354	1010.0	11.10220	1400.0	10.20396
220.0	11.25434	620.0	11.20160	1020.0	11.09901	1410.0	10.20301
230.0	11.25365	630.0	11.19964	1030.0	11.09579	1420.0	10.20207
240.0	11.25293	640.0	11.19764	1040.0	11.09100	1430.0	10.20112
250.0	11.25217	650.0	11.19561	1050.0	11.08621	1440.0	10.20018
260.0	11.25138	660.0	11.19355	1060.0	11.08142	1450.0	10.19924
270.0	11.25056	670.0	11.19147	1070.0	11.07663	1460.0	10.19829
280.0	11.24971	680.0	11.18935	1080.0	11.07184	1470.0	10.19735
290.0	11.24882	690.0	11.18720	1090.0	11.06705	1480.0	10.19641
300.0	11.24791	700.0	11.18502	1100.0	11.06226	1490.0	10.19546
310.0	11.24696	710.0	11.18281	1110.0	11.05747	1500.0	10.19452
320.0	11.24598	720.0	11.18057	1120.0	11.05268	1510.0	10.19357
330.0	11.24496	730.0	11.17830	1130.0	11.04789	1520.0	10.19263
340.0	11.24392	740.0	11.17600	1140.0	11.04311	1530.0	10.19169
350.0	11.24284	750.0	11.17367	1150.0	11.03832	1540.0	10.19074
360.0	11.24173	760.0	11.17131	1160.0	11.03353	1550.0	10.18980
370.0	11.24058	770.0	11.16892	1170.0	11.02874	1560.0	10.18886
380.0	11.23941	780.0	11.16650	1180.0	11.02395	1570.0	10.18791
390.0	11.23820	790.0	11.16405	1190.0	11.01916	1580.0	10.18697

(continued on next page)

Table 2.1 (continued from previous page)

Radius, km	V_p, km/s	Radius, km	V_p, km/s	Radius, km	V_p, km/s	Radius, km	V_p, km/s
1590.0	10.18602	1980.0	9.85564	2370.0	9.51202	2760.0	9.09587
1600.0	10.18508	1990.0	9.84721	2380.0	9.50251	2770.0	9.08374
1610.0	10.17586	2000.0	9.83877	2390.0	9.49296	2780.0	9.07151
1620.0	10.16670	2010.0	9.83032	2400.0	9.48335	2790.0	9.05921
1630.0	10.15758	2020.0	9.82187	2410.0	9.47370	2800.0	9.05015
1640.0	10.14850	2030.0	9.81341	2420.0	9.46399	2820.0	9.02538
1650.0	10.13947	2040.0	9.80494	2430.0	9.45423	2840.0	9.00062
1660.0	10.13048	2050.0	9.79645	2440.0	9.44442	2860.0	8.97585
1670.0	10.12152	2060.0	9.78796	2450.0	9.43454	2880.0	8.95109
1680.0	10.11260	2070.0	9.77945	2460.0	9.42462	2900.0	8.92632
1690.0	10.10372	2080.0	9.77092	2470.0	9.41463	2920.0	8.90020
1700.0	10.09487	2090.0	9.76238	2480.0	9.40459	2940.0	8.87408
1710.0	10.08606	2100.0	9.75383	2490.0	9.39449	2960.0	8.84797
1720.0	10.07728	2110.0	9.74525	2500.0	9.38432	2980.0	8.82185
1730.0	10.06852	2120.0	9.73665	2510.0	9.37410	3000.0	8.79573
1740.0	10.05980	2130.0	9.72804	2520.0	9.36381	3020.0	8.76819
1750.0	10.05111	2140.0	9.71940	2530.0	9.35346	3040.0	8.74066
1760.0	10.04244	2150.0	9.71074	2540.0	9.34305	3060.0	8.71312
1770.0	10.03379	2160.0	9.70205	2550.0	9.33257	3080.0	8.68559
1780.0	10.02517	2170.0	9.69334	2560.0	9.32202	3100.0	8.65805
1790.0	10.01657	2180.0	9.68460	2570.0	9.31141	3120.0	8.62904
1800.0	10.00800	2190.0	9.67583	2580.0	9.30073	3140.0	8.60002
1810.0	9.99944	2200.0	9.66704	2590.0	9.28998	3160.0	8.57101
1820.0	9.99090	2210.0	9.65821	2600.0	9.27916	3180.0	8.54199
1830.0	9.98237	2220.0	9.64935	2610.0	9.26828	3200.0	8.51298
1840.0	9.97387	2230.0	9.64047	2620.0	9.25731	3220.0	8.48242
1850.0	9.96537	2240.0	9.63154	2630.0	9.24628	3240.0	8.45186
1860.0	9.95689	2250.0	9.62259	2640.0	9.23518	3260.0	8.42131
1870.0	9.94842	2260.0	9.61359	2650.0	9.22400	3280.0	8.39075
1880.0	9.93996	2270.0	9.60456	2660.0	9.21274	3300.0	8.36019
1890.0	9.93151	2280.0	9.59550	2670.0	9.20141	3320.0	8.32803
1900.0	9.92307	2290.0	9.58639	2680.0	9.19000	3340.0	8.29587
1910.0	9.91463	2300.0	9.57724	2690.0	9.17852	3360.0	8.26371
1920.0	9.90620	2310.0	9.56806	2700.0	9.16695	3380.0	8.23155
1930.0	9.89777	2320.0	9.55883	2710.0	9.15531	3400.0	8.19939
1940.0	9.88934	2330.0	9.54956	2720.0	9.14359	3420.0	8.16575
1950.0	9.88092	2340.0	9.54024	2730.0	9.13178	3440.0	8.13209
1960.0	9.87249	2350.0	9.53088	2740.0	9.11989	3460.0	8.09846
1970.0	9.86407	2360.0	9.52147	2750.0	9.10793	3480.0	8.06482
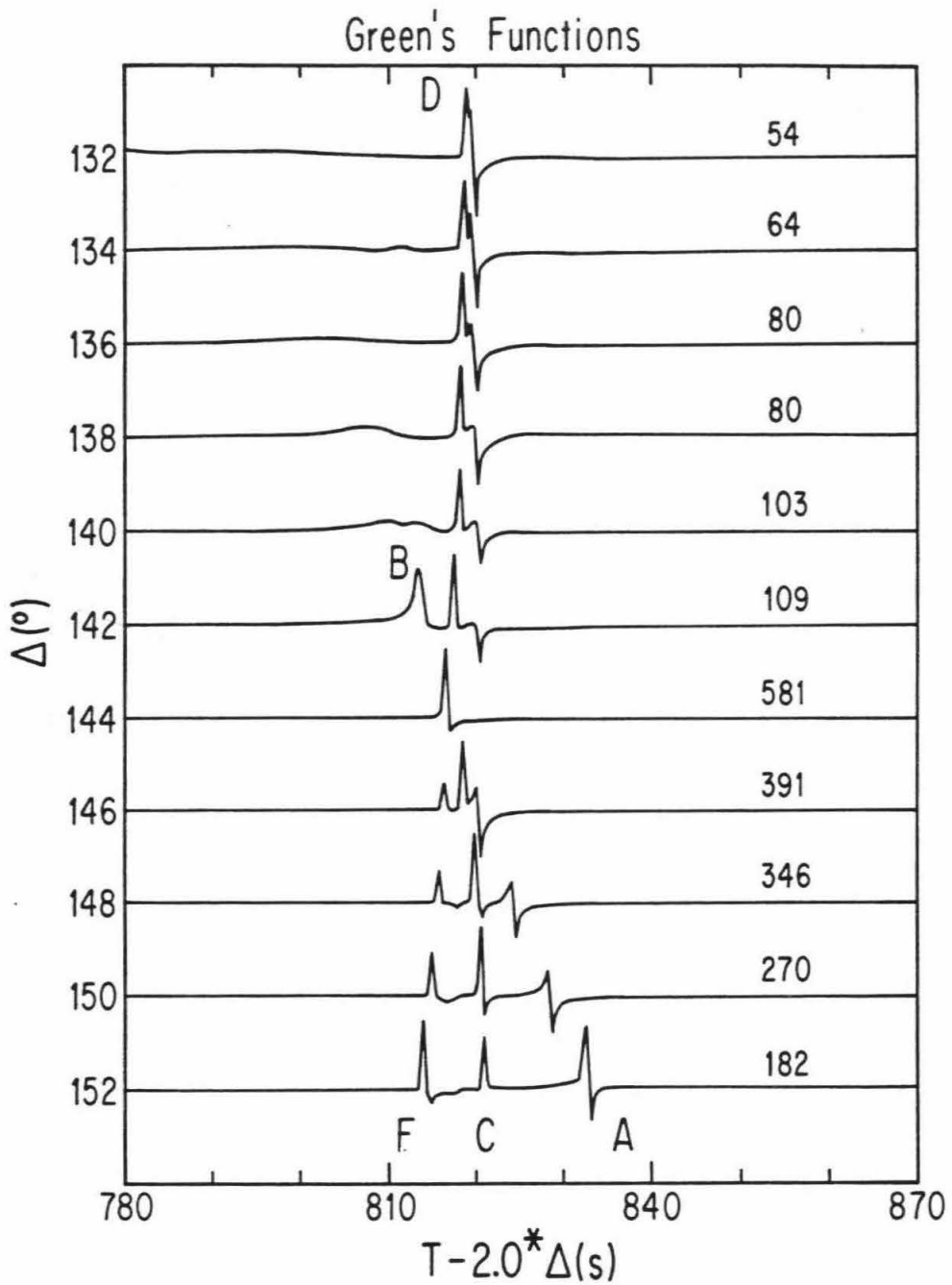
Figure 2.3: Broadband responses for a deep focus (600 km) showing the PKP triplications. The numbers on the right are the relative peak-peak amplitudes of the PKP phases.

AB; phases going through the bottom of the outer core, PKP-BC or BC; phases reflected back from ICB, PKiKP or CD; and phases refracted from the inner core, PKIKP or DF. Furthermore, PKP-B_{diff} and PKP-C_{diff} denote diffraction from the tip of the B-cusp and the C-cusp, respectively. These diffractions are very sensitive to the velocity gradient at the bottom of the outer core, as we will see later. When the ratio of two phases is used, we implicitly mean the amplitude ratio of the two phases; for example, BC/AB means the amplitude ratio of BC over AB. Likewise, when the difference of two phases is used, we implicitly mean the differential travel time of these two phases; for example, AB − DF means the travel time of AB minus the travel time of DF.

The generalized ray theory approach has been used in previous modeling efforts at the core-mantle boundary and has been found to be quite useful [*Lay and Helmberger*, 1983b]. One particular advantage of this method is the ability to isolate contributions associated with specific paths as displayed in Figure 2.4. Some sample ray paths displayed are associated with reflections from the various interfaces simulating the velocity structure after Earth flattening.

The responses displayed in Figure 2.4, at 136°, are broken into contributions from the outer core (CD) and the inner core (DF). The upper set of synthetics contain those generalized rays reflecting from the outer core, including the rays reflecting from the ICB boundary (CD). Four sample ray paths bottoming in the outer core are displayed to indicate those generalized rays contributing to the response. The middle set of synthetics contain those generalized rays returning from the inner core (DF). Seven sample ray paths bottoming in the inner core are displayed to indicate those generalized rays contributing to the response.

Figure 2.4: Raypaths reflecting off the various layers in a stratified model, indicating contributions from PKiKP (reflected, outer core) and PKIKP (refracted, inner core). The synthetics (136°) are constructed by summing up the contributions from these two regions. The long-period energy from the B-caustic is shown to come from the diffraction in the outer core.
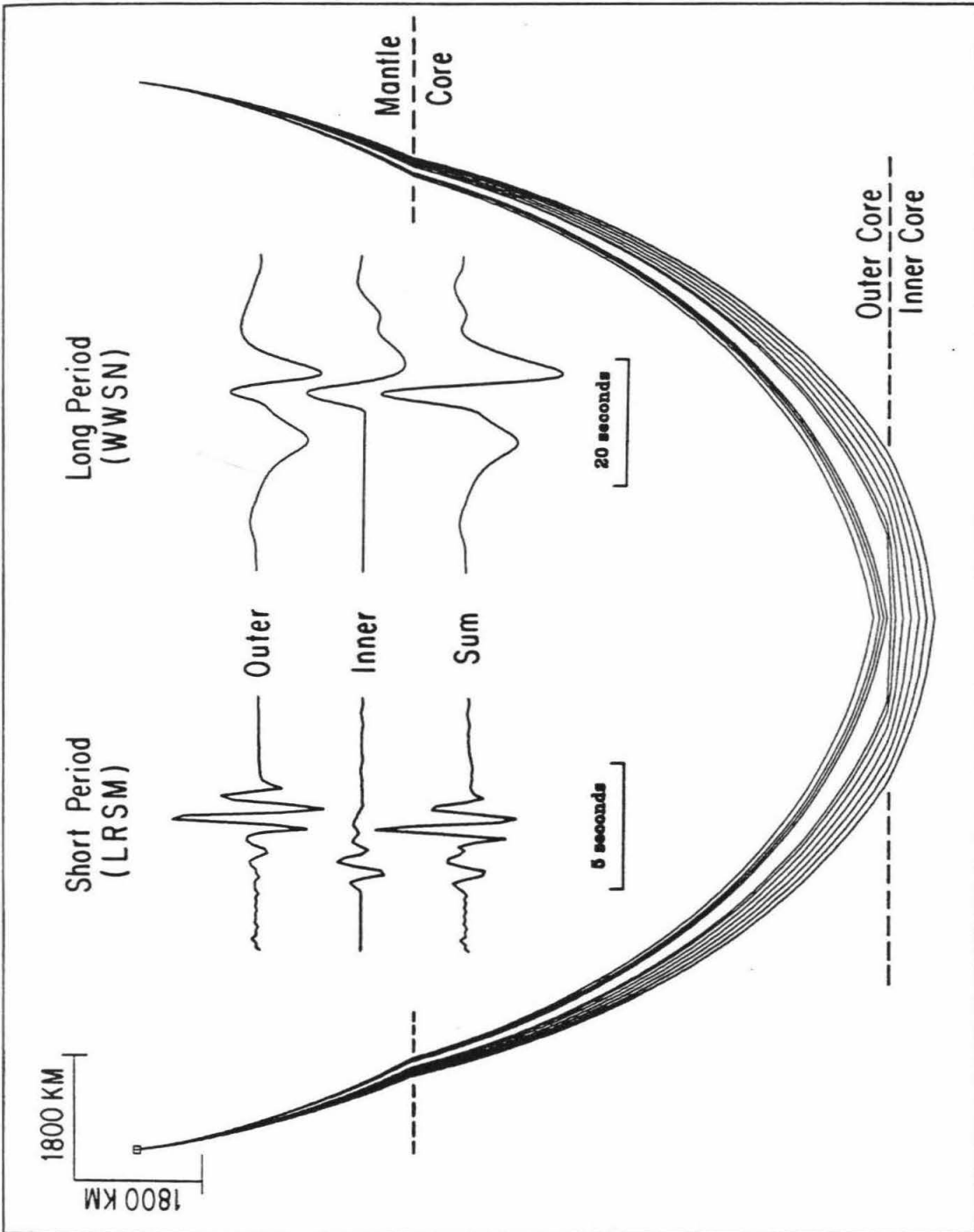
These two geometric arrivals are separated in the short-period simulation but simply reinforce each other in the long-period response. Thus, the short-period data are most useful in resolving the time separation, as pointed out by *Cummins and Johnson* [1988]. Working with the differential timing between isolated pulses proves useful in forward modeling these PKP triplications, as in previous modeling efforts. On the other hand, the long-period synthetics display the earlier arriving diffracted signals coming from the outer core, which can be used to constrain the velocity gradient at the bottom of the outer core. Computing these diffractions requires the treatment of complex ray parameters, since the energy must tunnel through the highest velocity layers to appear in the shadow. The treatment of complex ray parameters is given in terms of full-wave theory by *Richards* [1973] and in terms of Cagniard-de Hoop theory by *Mellman and Helmberger* [1974]. We will discuss the diffracted PKP wave field produced by these two methods next.

Comparisons of synthetics generated by our approach against those presented in *Aki and Richards* [1980, Figure 9.31], show a better agreement with each other than with observed waveforms. A sample comparison is given in Figure 2.5, where we also included some truncation effects which must be understood to avoid confusion. The format is similar to that used by *Cormier and Richards* [1977], where the delta function response for the model PEM at $\Delta=136°$ is given on the left and the long-period synthetic on the right. Our synthetics have been convolved with various triangles to smooth out high-frequency numerical noise, since no attenuation has been included. It appears that these full-wave theory results have also been smoothed, since we can no longer resolve DF from DC. Thus, the comparison displayed as an overlay was made with a triangular time function of rise time and fall time of 0.8 s.

Figure 2.5: Comparisons between generalized ray theory (GRT) and full-wave theory results from *Cormier and Richards* [1977] at $\Delta=136°$. The column on the left displays Green's functions with different equal triangular time functions for PEM model. The column on the right shows the corresponding long-period WWSSN response. The δt_i denotes the rise time. Numbers indicate energy reflected from different depths; see text for detailed discussion. On the very bottom is an overlay of GRT results with $\delta t_i=0.80$ s and full-wave results. Note the close resemblance of the long-period diffraction as well as two pulses, PKIKP and PKiKP, shown on GRT Green's functions.
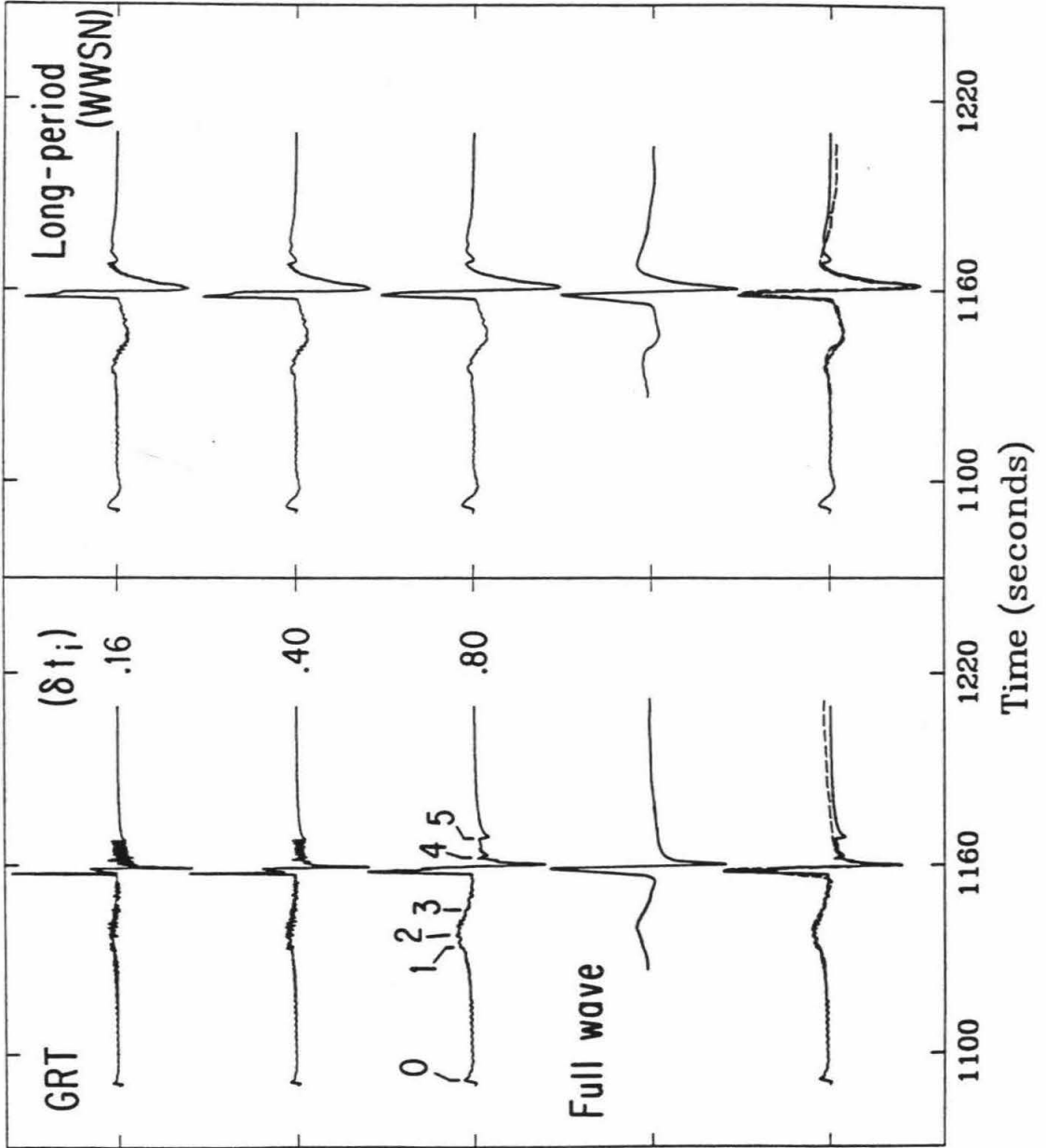
The generalized ray response starts at a depth of 3200 km and produces a trunca-tion pulse, labeled "0", caused by the presence of the complex transmission coefficient across the CMB. The phase labeled "5" is associated with the deepest reflection in the inner core (depth of 5500 km) and is also a truncation phase. These two pulses can be moved about by adjusting the sampling depth parameters, depending on the domain of interest. The small pulse labeled "4" is an artifact caused by a small change in velocity gradient in the inner core. The layer thickness was assumed to be 10 km before applying the Earth flattening approximation. Since multiples have not been included, we can assume as many layers as necessary to resolve details. However, given the high-frequency cut-off of observed seismograms, we generally do not include model details smaller than detectable.

The numbers 1, 2, and 3 indicate contributions at depths around 4000, 4400, and 4800 km, respectively, where the long-period B diffractions are produced. According to our calculations, the velocity gradient from the depths of 4000 km to 5000 km contributes to this arrival. This response is strongly influenced by the fastest layers encountered along the ray paths, which includes the structure in D''. In this particu-lar case, we did not include multiples in this zone, so our calculation is not complete. However, based on previous experience in tunneling [see *Helmberger*, 1983], we ex-pect our results to be a good approximation. The agreement with full-wave theory results appears adequate.

2.4 Data

We selected two events for this study based on the data coverage available (Ta-ble 2.2. Event 1 produced a long-period Worldwide Standardized Seismograph Net-

Event No.	Date	Origin Time (UT)	Epicenter	Depth (km)	m_b
1	May 21,1967	18:45:11.7	1.0°S/101.5°E	173	6.3
2	April 7,1964	13:18:18.9	0.1°N/123.2°E	150	6.3

Table 2.2: Two events used in this study.

work (WWSSN) section with very good station coverage in the United States (see Figure 2.6). Some of the records from these stations were used by *Müller* [1973] and *Cormier and Richards* [1977]. The distances range from 130° to 150°, which is ideal for sampling the various branches displayed earlier in Figure 2.3. Unfortunately, the short-period observations for this event are too complex to be useful, since this earthquake proved to be a double event as addressed later.

Event 2 produced a short-period Long Range Seismic Measurements (LRSM) section; see Figure 2.6 for station coverage. Figures 2.7 and 2.8 show the observed waveforms for distances ranging from 107° to 136°. The stations and epicentral distances are marked on the left-hand side. The differences of absolute travel time relative to PREM are marked on the right-hand side with a reduced time scale calculated according to PREM shown in the bottom. These are relatively clear records. From 107° to 123° in Figure 2.7, we see one arrival, namely, the reflection from the ICB (PKiKP). Although DF comes in a distance of about 120°, there is no distinguishable change in the waveform in these short-period data, also indicated in synthetics [e.g.,*Cormier and Richards*, 1977]. From 130° to 136° in Figure 2.8, we see two arrivals, PKIKP and PKiKP, which are marked according to the geometric

Figure 2.6: Locations of WWSSN and LRSM stations for the two events used in this study.
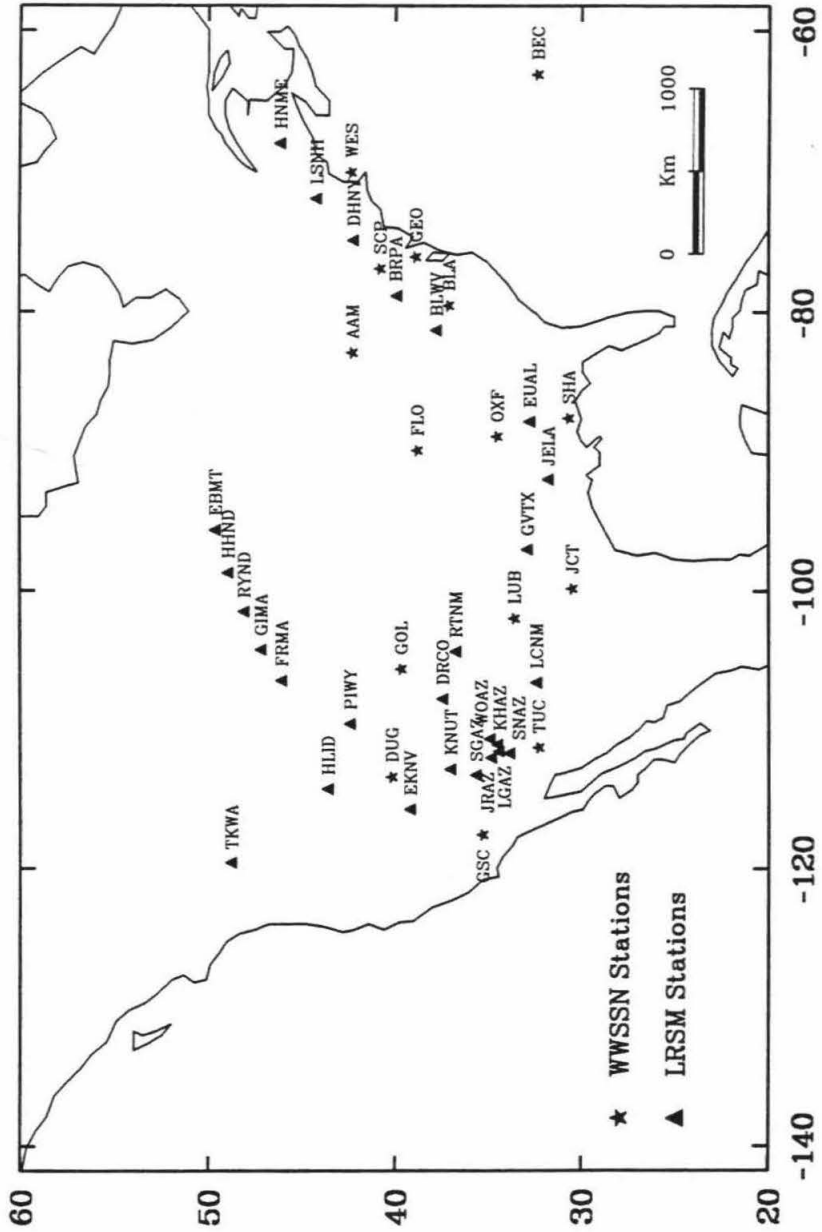
arrivals from PMNA. Note that there are large disparities in absolute travel time in the records. The difference is about 1.5 s between records for the tectonic region in the Southwestern United States and for the shield region in the Northern and Northeastern United States. There is also a tendency for basin-and-range observations to be longer periods than those received along the profile from FRMA to EBMT. Previous studies by *Helmberger and Wiggins* [1971] have shown that the coda associated with shallow receiver structure is particularly small for the FRMA to EBMT profile as well as for most of the stations along the HNME to BLWA profile. These disparities are generally attributed to differential attenuation in the shallow mantle [see *Grand and Helmberger*, 1984]. Thus, they do not affect the results of this study. We shall, however, incorporate upper mantle models to correct these discrepancies in future studies.

At distances beyond 130°, starting with GVTX, we see some earlier arrivals or precursors. These precursors have been interpreted as due to inner core transition-zone structure, roughly 420 km above the ICB [*Bolt*, 1962, 1964], scattering from the D'' region by *Haddon* [1972], and topographic relief of the core-mantle boundary by *Doornbos* [1988]. The Haddon interpretation supposes that small scale features near the CMB allow ray-parameter variation, which brings some of the strong caustic energy at about 144° to nearer distances along the extension of the AB branch (see Figure 2.3). The shapes of these scatterers and their possible variation with location have not been addressed to our knowledge. Broadband data should be particularly useful for this purpose.

With the recently developed scanner technology, short-period LRSM observations such as this are easily digitized. Also, the rapid paper recording rate allows easy and

Figure 2.7: Short-period LRSM observations of the April 7, 1964 Indonesia event (No.2). On the left are stations and distances. The seismograms were shifted to align with PREM time predictions by the amounts shown on the right.

32

STA Δ(°)		T-T PREM
TKWA 107.5		5.9
HLID 112.9		7.0
EKNV 113.6		6.9
PIWY 116.5		6.7
KNUT 116.5		7.5
SGAZ 116.7		7.4
FRMA 116.7		6.2
GIMA 117.4		6.5
JRAZ 118.0		7.4
RYND 118.4		6.1
LGAZ 118.5		7.3
SNAZ 118.5		6.9
KHAZ 118.8		7.8
EBMT 119.3		6.5
HHND 119.4		5.2
DRCO 120.0		7.5
RTNM 122.7		7.0
LCNM 123.0		7.0

865   870   875

$T-2*\Delta(s)$
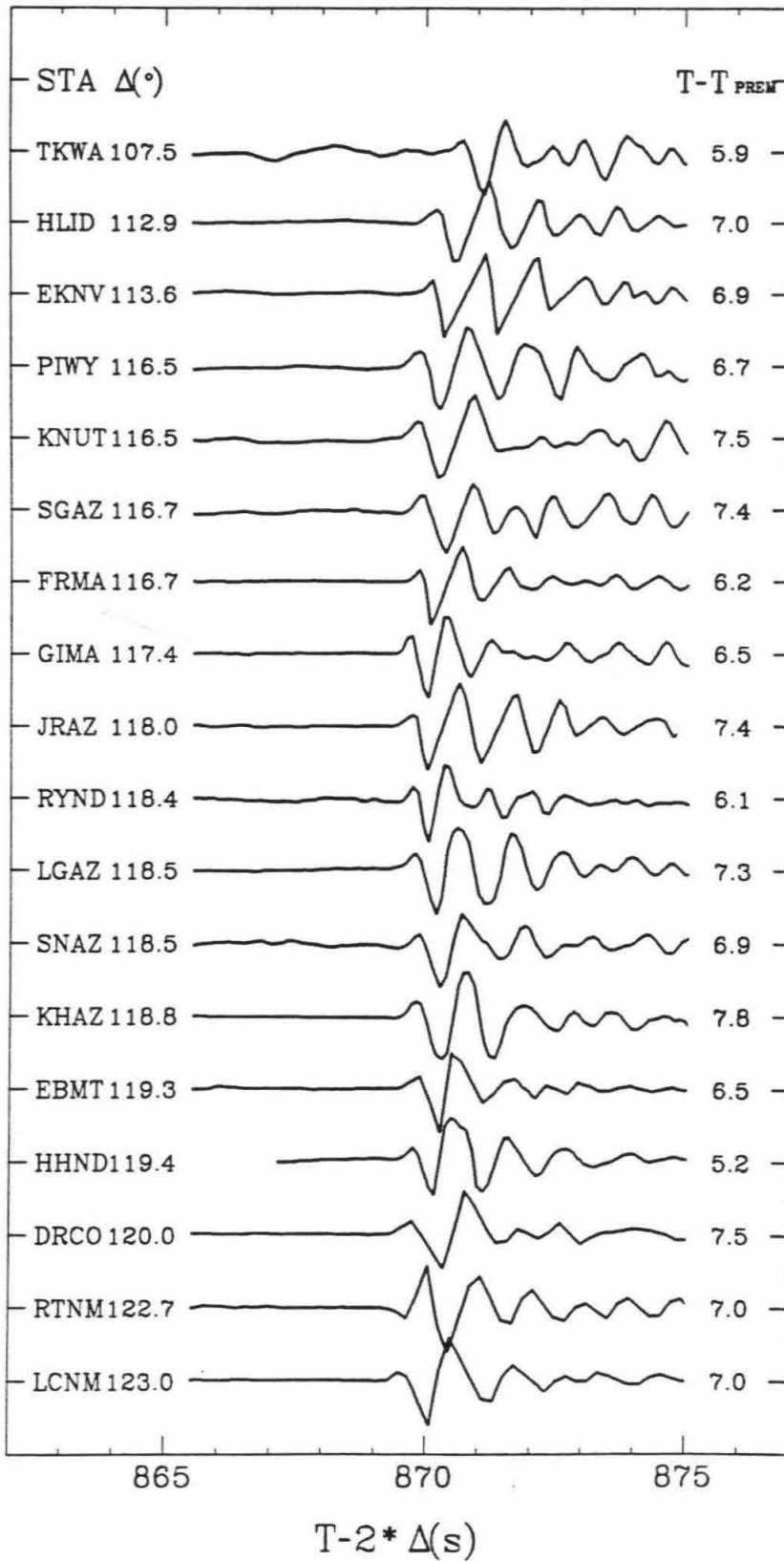
Figure 2.8: Short-period LRSM observations from Event 2 at ranges 130° to 136°. The seismograms were shifted to align with PREM time predictions by the amounts shown on the right. Note distinct PKIKP and PKiKP arrivals as well as PKP precursors are observed. The separation between the PKIKP and PKiKP arrivals are marked according to the model of this study (PMNA).

STA Δ(°)

T-T PREM

GVTX 129.9 ... 6.4

HNME 132.9 ... 5.0

LSNH 133.8 ... 5.6

JELA 134.0 ... 6.6

DHNY 134.8 ... 5.5

BRPA 135.4 ... 5.6

BLWV 136.0 ... 5.2

PKIKP PKiKP

855   860   865   870   875

$T - 2 * \Delta(s)$
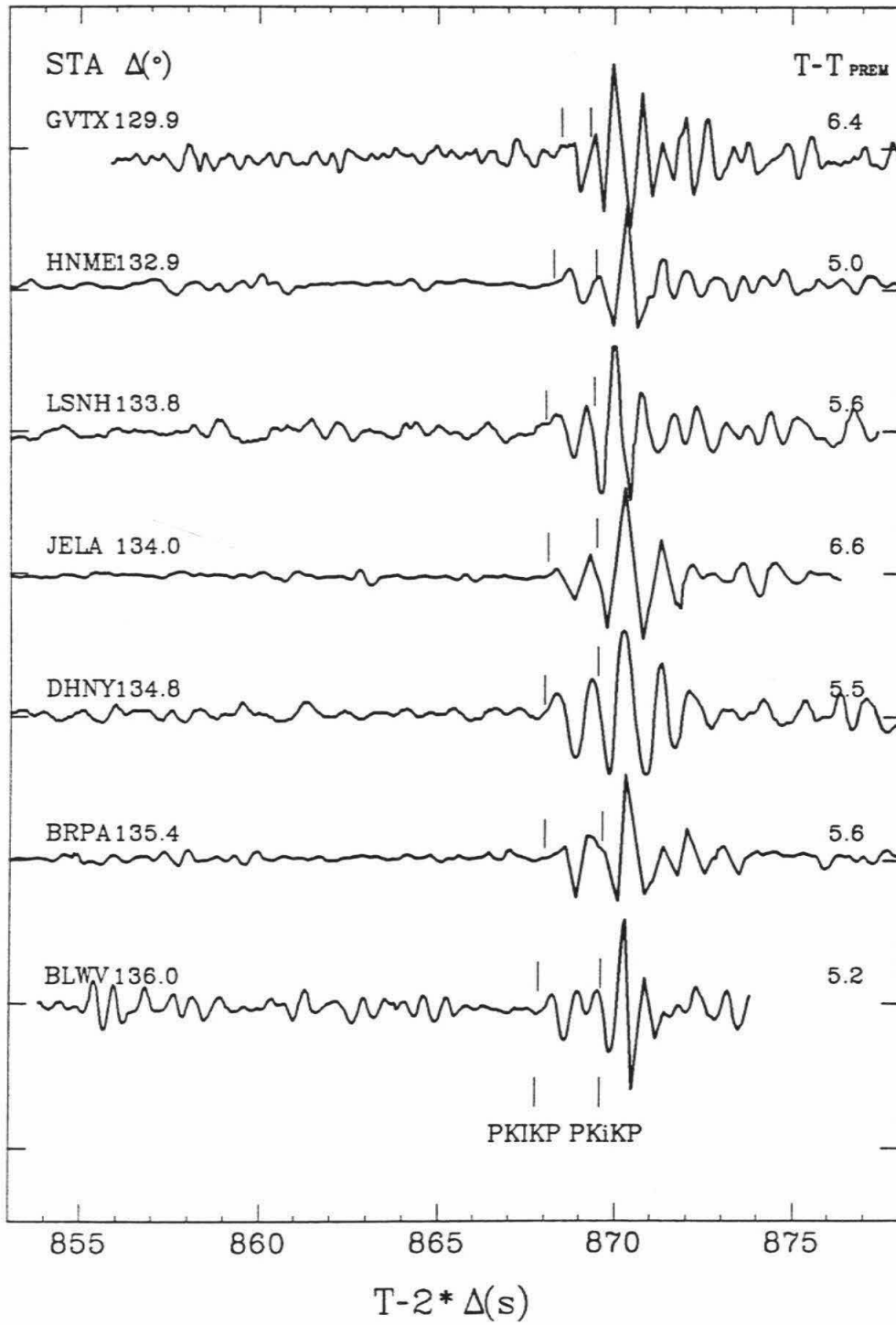
accurate reading of travel times as compared to the WWSSN recording system.

Because the epicenters of these two events are near each other and the stations for both events are almost all in the continental United States, the ray paths are confined to a relatively narrow azimuth range (within 60°) and sample a small portion of the ICB (a cone with a semi-vertical angle of about 15°) beneath the northwestern Pacific. This helps us eliminate the effect of the seismic sources and minimize possible lateral variation near the ICB, as discussed earlier.

The reasons we selected a long-period section and a short-period section need some explanation. Waves with different wavelengths have different sensitivities to the structure they sample. The application of these waves to modeling Earth structures produces different resolution and limitations [see *Müller*, 1973]. Modeling short-period and long-period records simultaneously is not equivalent to working with the latest IRIS data, where the Green's function displayed in Figure 2.3 can be used directly. Unfortunately, their density and lack of recording history render them less useful. Thus, we rely on conventional observations to provide the coverage needed to constrain the structure near the ICB in this study.

2.5 Waveform Modeling

We proceed, as in previous forward modeling exercises, to explore the model space following a trial-and-error procedure. That is, when we see discrepancies between observed waveforms and synthetics, we modify the model until they fit in an overlay sense. We are aided in this endeavor by working with the decomposed wavefield, as discussed earlier. The starting models are PREM and PEM, as mentioned earlier. These two models, in fact, bracket the model PMNA which appears appropriate for

this particular sample of the Earth. Thus, to convey the sensitivity of the model parameters in the vicinity of the ICB, we will include long-period and short-period synthetics for these three models.

2.5.1 Long-Period Sections

The three long-period record section comparisons are given in Figures 2.9, 2.10, and 2.11. Each seismogram is aligned and normalized with respect to the peak amplitude of the synthetic for easier comparison. The source used in generating these synthetics is shown on the upper-left corner of Figure 2.11. This effective source contains the convolution of the source time function with the long-period WWSSN instrument response. Note that it is a double source. The time function consists of two trapezoids with rise-time, duration and fall-time of 1.0, 1.8 and 1.0 s, respectively, separated by 3.6 s and with relative amplitudes of 10 to 8. This source model was obtained by modeling NUR, Nurmijarvi, Finland, at a distance of 84°, where the direct arrival is undisturbed by other phases. This double source is clear in many other records from western Canada and Alaska. We were not aware of this source complexity until deeply involved in these modeling exercises since previous investigators had modeled it as a single source [*Müller*, 1973; *Cormier and Richards*, 1977]. Working with a simple source has obvious advantages, but since this double source is common to all the waveforms, we can still obtain valuable constraints.

Starting with the PREM comparisons displayed in Figure 2.9, we see that the synthetics agree with the data very well at distances larger than 140°. At smaller distances (e.g., TUC and WES), however, the diffracted energy off the tip of the B-cusp seems smaller in the synthetics than in the data. Likewise, the synthetics

Figure 2.9: Comparisons of synthetics (dashed lines) for PREM and long-period observations (solid lines) of Event 1. On the left are the peak-peak amplitudes (in cm) of data with the station names. On the right are the relative amplitudes of the synthetic predictions.

38

MODEL PREM

Figure 2.10: Comparisons of synthetics (dashed lines) for PEM and long-period observations (solid lines) of Event 1. On the left are the peak-peak amplitudes (in cm) of data with the station names. On the right are the relative amplitudes of the synthetic predictions.

MODEL PEM

41
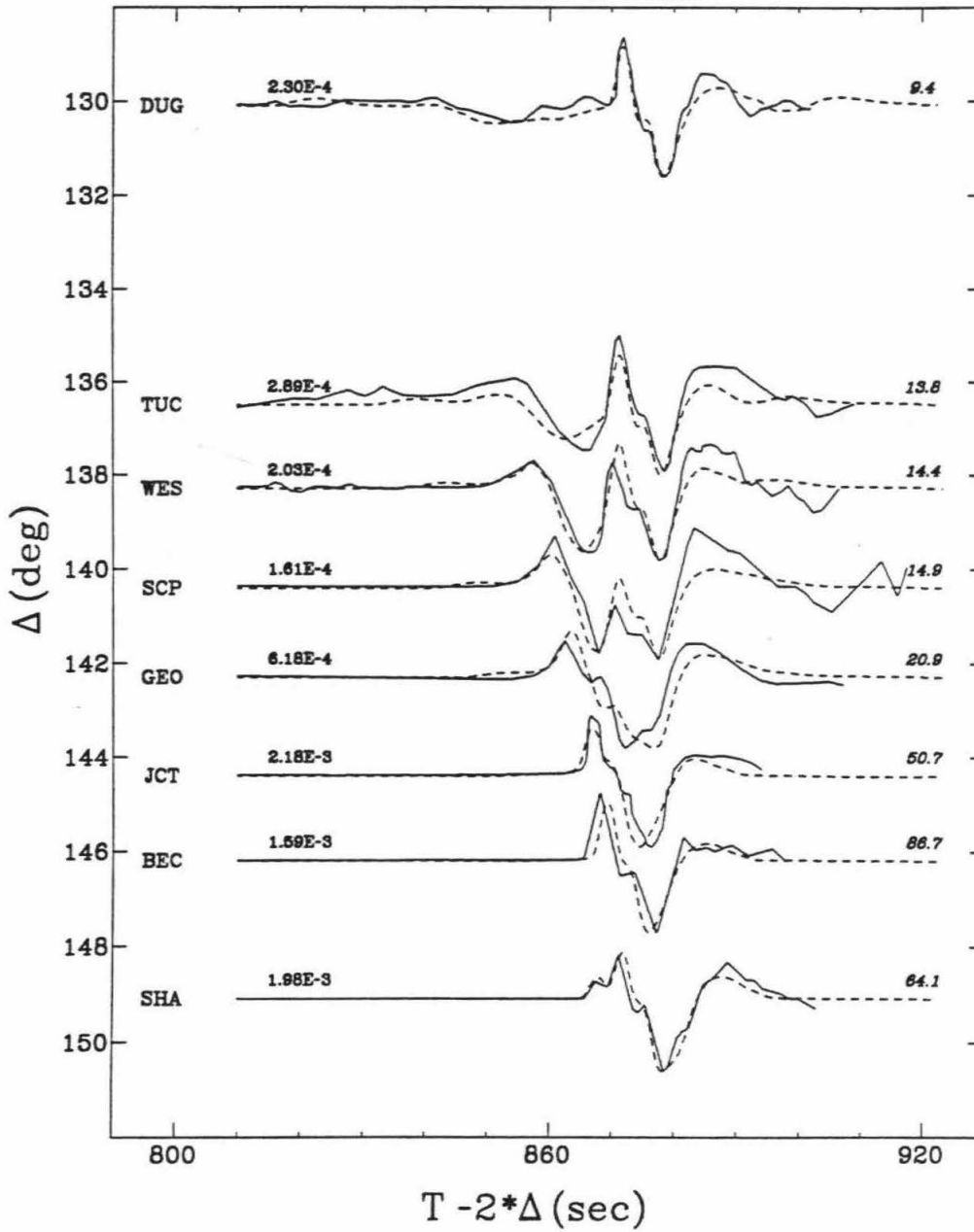
Figure 2.11: Comparisons of synthetics (dashed lines) for PMNA and long-period observations (solid lines) of Event 1. On the left are the peak-peak amplitudes (in cm) of data with the station names. On the right are the relative amplitudes of the synthetic predictions. The low-velocity gradient in the model at the bottom of the outer core is responsible for the excellent waveform fit in the 136° to 142° range. The source function was obtained by studying this event at ranges 30° to 90°.

MODEL PMNA
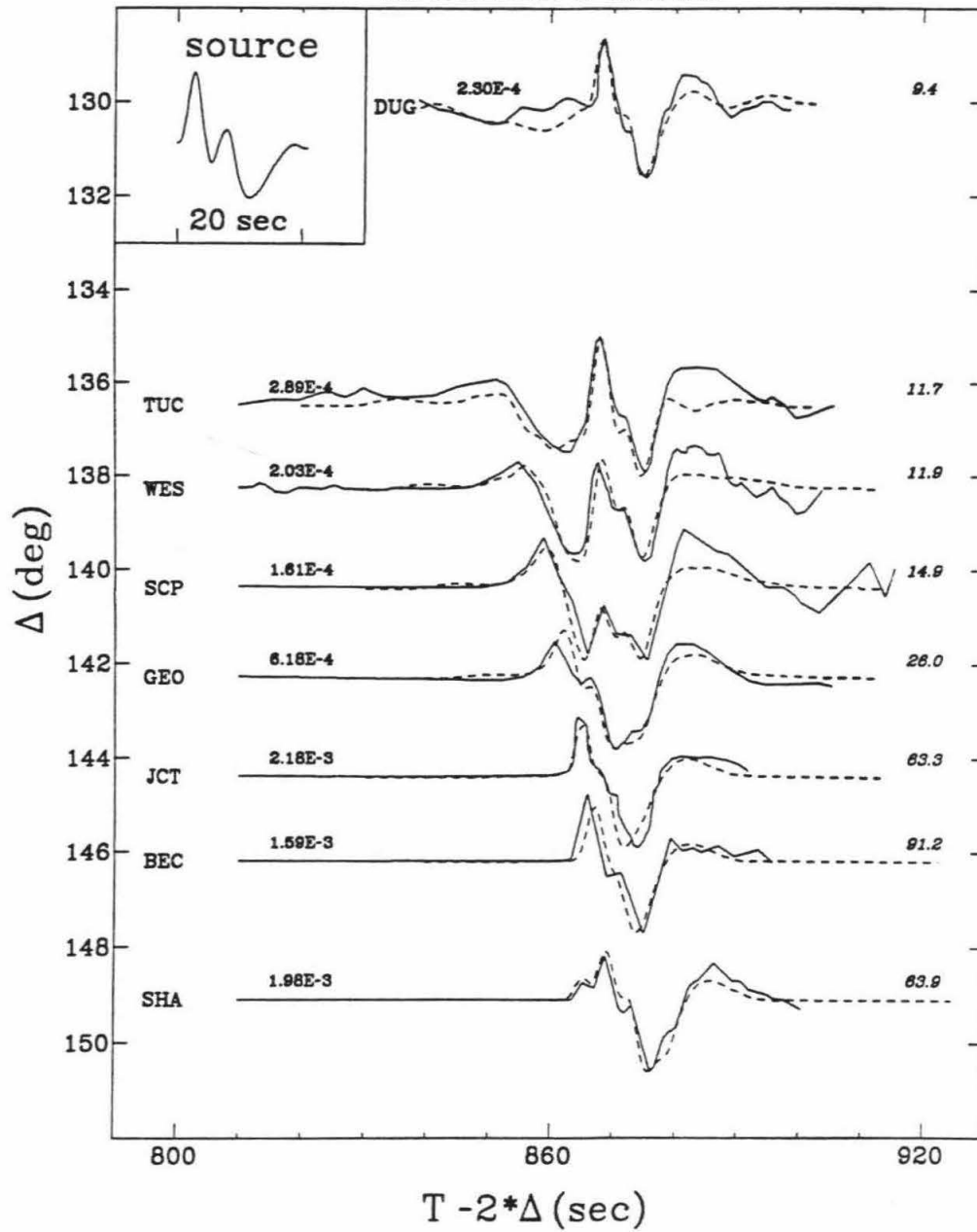
for PEM (Figure 2.10) agree with the data well at distances larger than 144°. But at distances between 136° and 142°, where several core phases (PKIKP, PKiKP, PKP-B$_{\text{diff}}$, PKP-BC) interfere, the synthetics seem to be out of phase with the data. Agreements between the synthetics and the data for our preferred model PMNA, in Figure 2.11, are better at the important distances of 136° to 140°. Model PMNA, as mentioned before, has a small gradient roughly 400 km above the ICB. We find this small gradient necessary to account for the PKP-B$_{\text{diff}}$ diffraction as in shown the TUC record.

The amplitudes of the observations are displayed on the left side of Figures 2.9, 2.10, and 2.11, while the relative amplitudes of the synthetics are displayed on the right edge of each figure. In Figure 2.12, the relative amplitudes of the synthetics are normalized to fit the observations around B-caustics (between 143° and 149°) in the least squares sense; this assumes that the B-caustic is caused by structure at depths around 4400 km, which is thought to be smoothly varying [*Müller*, 1973]. Because of the large scatter of the amplitudes of the data, the models can only be weakly constrained. Nevertheless, model PEM predicts anomalously large amplitudes in the range 130° to 140° due to the large jump at the ICB of 0.83 km/s. Thus, we can set this number to be the upper bound of the velocity jump at the boundary.

2.5.2 Short-Period Sections

Modeling the short-period LRSM section, more specifically, the matching of differential travel times and relative amplitudes of PKIKP and PKiKP, for distances 130° to 136°, puts a strong constraint on the velocity jump at the ICB as displayed in Figure 2.13. We did not include records for smaller distances in our modeling exer-

Figure 2.12: Comparisons of the amplitudes of the long period data of Event 1 to those predicted by the three models.
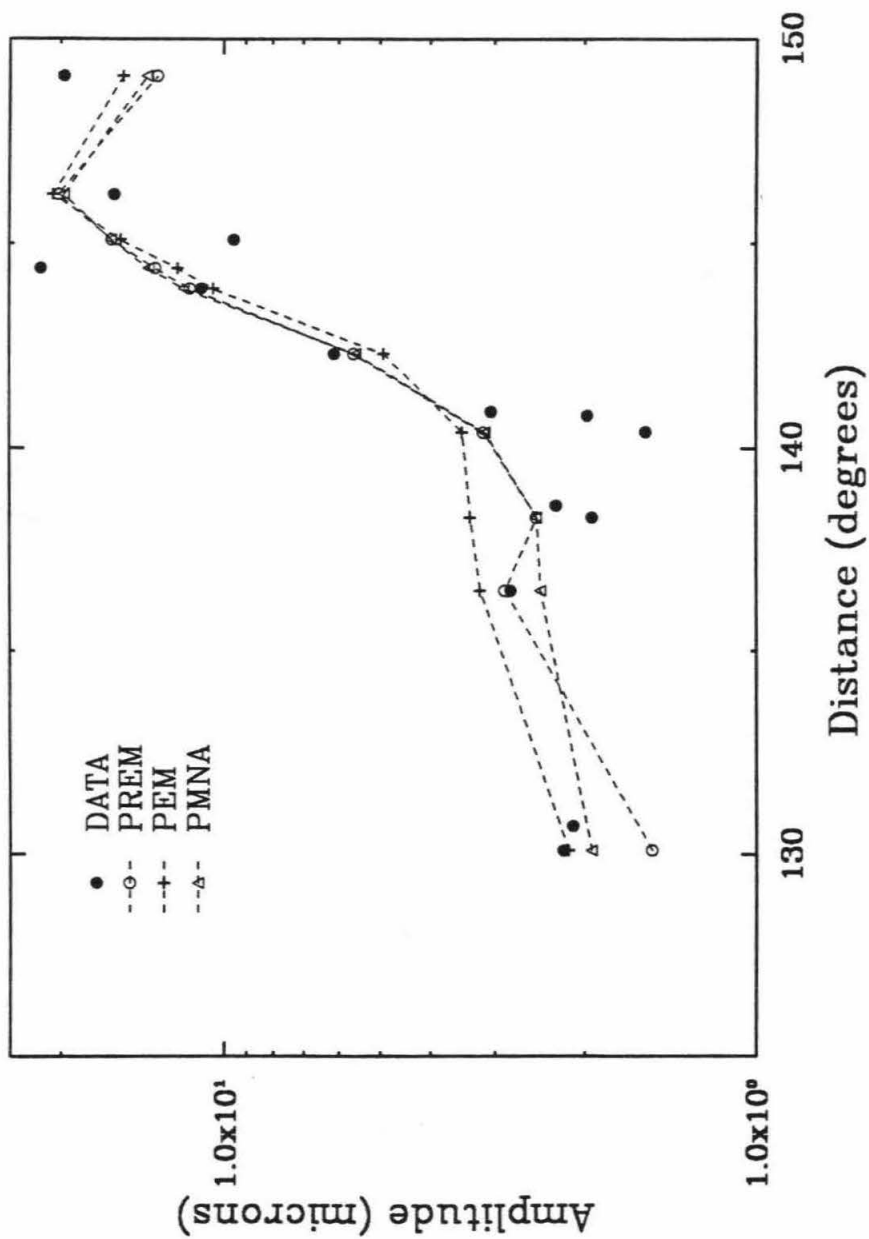
cise when there were no two discernible arrivals. The seismograms are aligned with respect to the phase PKiKP of the synthetics, and each seismogram is normalized to its peak amplitude. These synthetics contain a convolution with an effective source function as displayed in the upper right hand corner, namely, the observation of GIMA. The choice of GIMA as an empirical source function was somewhat arbitrary but was based on several judgments. Since some researchers find evidence for waveform distortions at ranges less than 120° [see *Cummins and Johnson*, 1988], we should choose a record at smaller distances, perhaps TKWA. However, since stations such as HNME have lower attenuation than TKWA, we would be forced to correct for this feature. Thus, GIMA was chosen because of its duration and simplicity. On the other hand, since we are primarily interested in identifying the triplication position, this empirical source function is probably satisfactory.

Comparing the synthetics displayed in Figure 2.13, we see that the differential travel time between PKiKP and PKIKP is too small for PREM compared with the data, but too large for PEM. The differences are about 0.3s for both models. This differential travel time is sensitive to the velocity jump at the ICB and the gradient at the top of the inner core. Adjustments in these parameters lead to model PMNA, which fits these short-period waveforms quite well.

The relative amplitudes of the synthetics are labeled on the left side of each column in Figure 2.13, and those of the data are shown along the right edge of the figure. The synthetics are nearly constant in this range, while the data vary by about a factor of *2*. This variation is probably caused by receiver structure and hence provides no meaningful constraint.

A constant $\Delta t^* = 0.4$s was applied to the PKIKP portion of the synthetics to

Figure 2.13: Comparisons of synthetics (dashed lines) of the three models (Figure 2.2) and the short-period observations (solid lines) of Event 2. The data have been shifted slightly to align with the synthetics. The relative amplitudes of the data are shown on the right of the right panel with the relative amplitudes of the synthetics for each model are shown on the left of the corresponding panel. Note that the separations between PKIKP and PKiKP are not far apart enough in PREM, too far apart in PEM, and about right in PMNA.
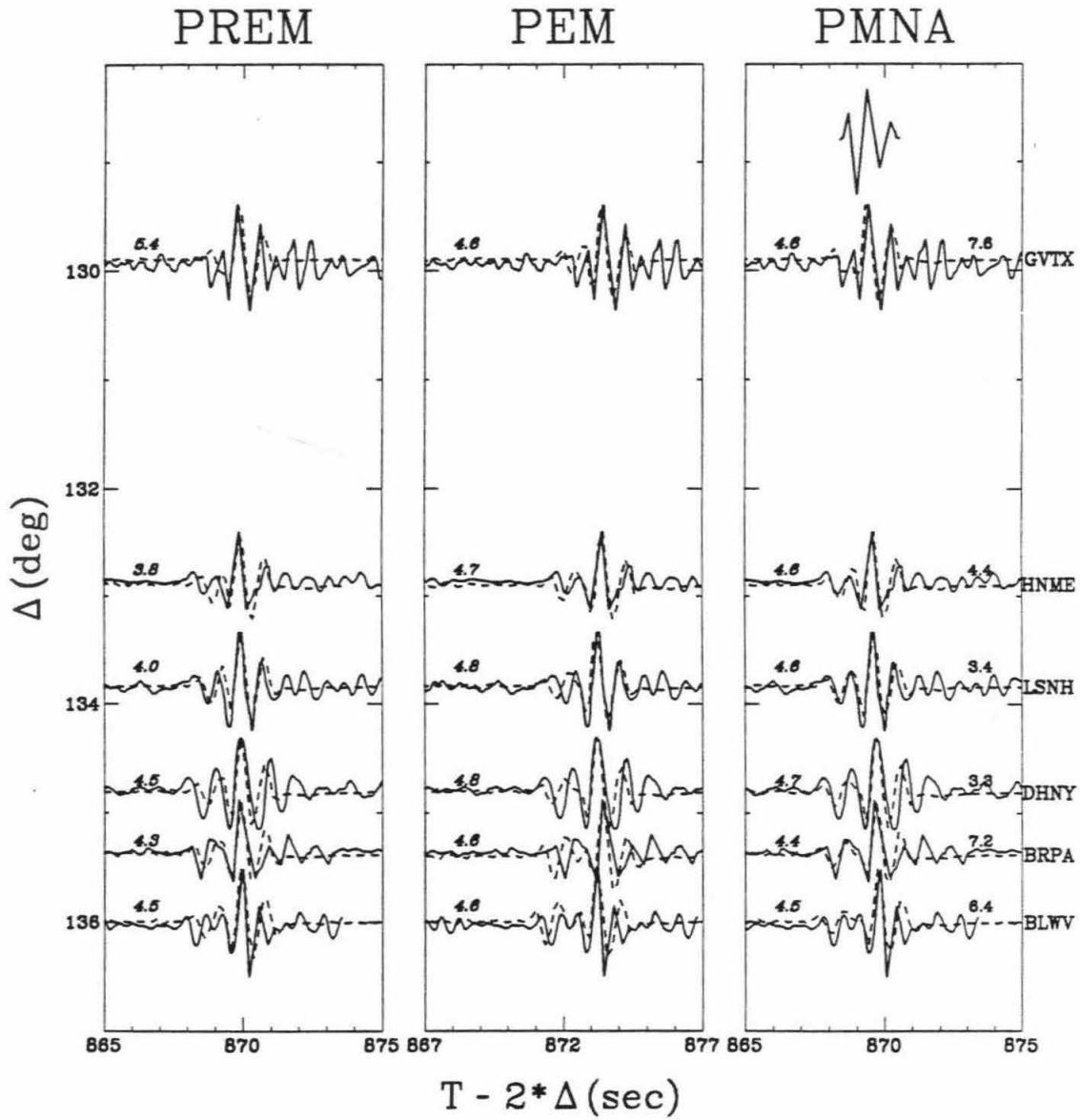
correct for the extra attenuation in the inner core. Sensitivity of waveforms to the applied Δt^* is shown in Figure 2.14. The attenuation operators of $\Delta t^* =0.1$, 0.3, 0.4, 0.5s were applied to PKIKP in synthetics at 136° for the three different models. The record at station BLWV with the same distance is also shown for comparison. Note that no matter what model one assumes, Δt^* should be larger than 0.3s or, equivalently, Qsmaller than 300 in order to fit the relative amplitude of PKIKP/PKiKP. The separations of these two phases for Δt^* from 0.3 to 0.5s, however, are too small for PREM and too big for PEM, compared to the record. Model PMNA, with $\Delta t^* =0.4$s, seems to fit the waveform of the record best. Δt^* $=0.4$s at this distance is equivalent to Q=200 at the top of the outer core, which is consistent with *Doornbos* [1983]. Note that the bottoming depths of this distance range (130-136°) are very shallow (less than 40 km) into the inner core. The trade-off between shear velocity and Qin the inner core has been discussed at length by *Cummins and Johnson* [1988]. The pair (Q=200, V_s=3.5 km/s) assumed here falls very close to their trade-off curve. Note again, however, that this set of data does not tell us the Qstructure deeper than 40 km, which the data did not sample.

Before we move to the discussion section, it is interesting to note that this kind of short-period record section is useful in exploring heterogeneity at the core-mantle boundary (CMB) or anomalies in the inner core. Raypaths of PKiKP and PKIKP are separated by about 200 km when crossing the CMB (see Figure 2.4). A 2% P velocity variation across this distance through D'' would generate 0.3s variation in the differential travel time of these two phases. On the other hand, the inner core has been confirmed to be very anisotropic (see detailed discussion in Chapter 4,5). A 1% of anisotropy at the very top of the inner core will produce the same amount
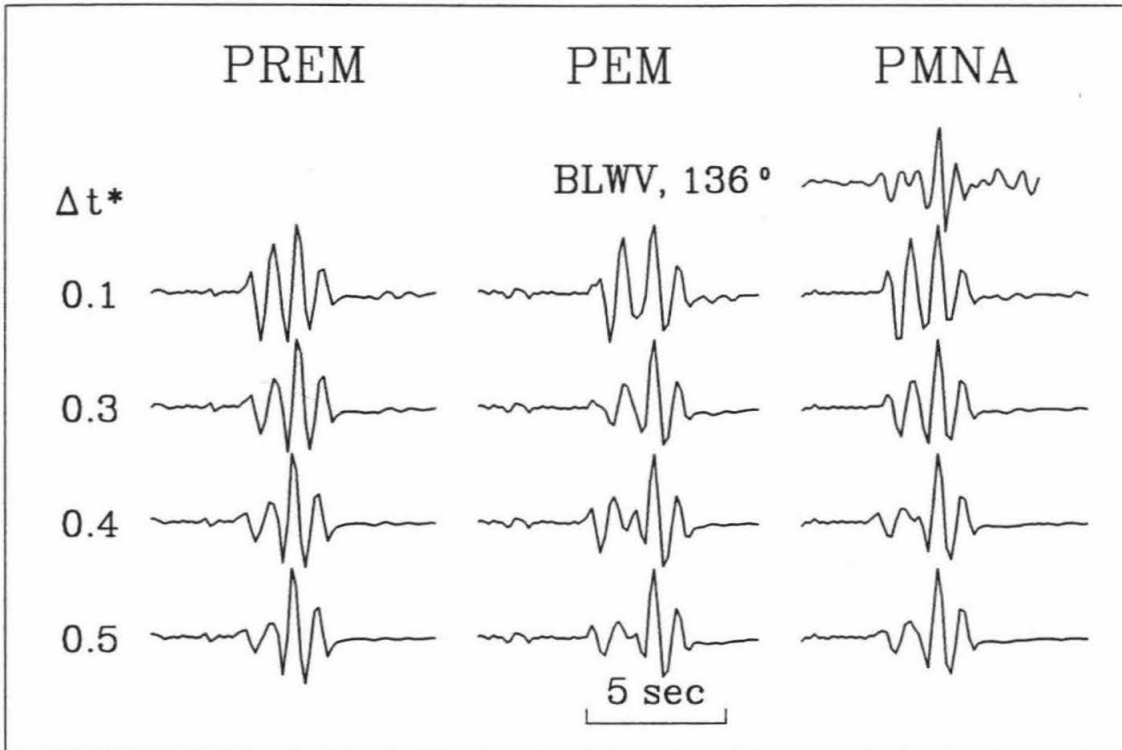
Figure 2.14: sensitivity of waveforms to Δt^* . Various Δt^* values were applied to PKIKP in synthetics from three different models. This study favors strong attenuation at the top of the inner core.

of variation in the PKiKP-PKIKP differential time. This magnitude of variation should be readily detectable from short-period LRSM record sections. However, it might be difficult to distinguish one from the other.

2.6 Discussion

Our long-period studies are consistent with *Müller* [1973], in that there is only one discontinuity separating the outer and inner core. We also agree that the density and shear velocity jumps at this boundary are only weakly constrained by this type of triplication data. Essentially, the critical angle effects dominate, and they are controlled by the P velocities in this case. Thus, we assumed density and shear velocities from the PREM model, which are compatible with the free-oscillation data and internal inner core reflections from *Rial and Cormier* [1980], as well as PKiKP/PcP data from the recent studies by *Shearer and Masters* [1990]. The radius of the inner core in model PMNA is slightly raised from PREM to compensate for the delay in travel time caused by the lower velocity structure in the bottom of the outer core, assuming the average travel time in PREM is good. This, however, should have no significant effect on our conclusions.

Our values for the upper and lower sides of the ICB, 10.22 km/s and 11.0 km/s, respectively, with a jump of 0.78 km/s, fall within the bounds established by *Cummins and Johnson* [1988] from short-period RSTN data. These two studies look at roughly the same sample of the Earth. *Choy and Cormier* [1983] report a jump of 0.52 km/s from broadband waveform modeling of an event in South America to stations in Asia and Australia. This low value is similar to Qamar's 0.6 km/s obtained by modeling short-period travel times. The latter two models estimate the velocity

at the top of the inner core to be 10.82 km/s which is outside the global travel time extremal bounds reported by *Johnson and Lee* [1985]. Thus, we conclude that the P velocity at the top of the inner core should be larger and, consequently, the large anomalous velocity gradient underneath ICB should be smaller than proposed in KOR5. The above low values should be considered anomalous, as pointed out by *Cormier and Choy* [1986] as well as *Cummins and Johnson* [1988]. The relatively large gradient below the ICB in model PMNA is only approximate for the very top of the inner core and may be modified for a larger data set.

The lower velocity gradient structure above the ICB in our model has also appeared in the literature. *Müller* [1973] did not discuss this feature but he used it in his model M2 (see also Figure 2.1). *Qamar* [1973] obtained it from short-period travel time and amplitude studies. A more recent study by *Souriau and Poupinet* [1991] on differential travel times of PKP data (ISC) provides further evidence for a low-velocity gradient at the base of the fluid core. This lower velocity gradient predicts that the *Bullen* [1963] parameter, an index of inhomogeneity, in the lower outer core to be 3.0 to 3.4, indicating possible phase or chemical changes in the region.

As mentioned before, this structure was needed to account for the long-period diffraction off the B-caustic in the WWSSN records. This gradient also has a strong effect on the termination of the BC branch (see Figure 2.3). A weak velocity gradient above the ICB will increase the diffraction beyond the C-cusp. *Choy and Cormier* [1983] found that a low gradient, as in KOR5, predicts anomalously large BC/DF and BC/AB ratios, which is inconsistent with an actual record at SHIO (Δ=156.3°). They concluded that the best Earth model should have a higher gradient, between PEM and PREM, which implies that the best Earth model should be homogeneous,

since both gradients of PEM and PREM are consistent with a homogeneous lower outer core model. This is an interesting and important result. However, this still could be due to regional effects, since their SHIO record samples a completely different region of the ICB (beneath the eastern Atlantic) from this study (beneath the northwestern Pacific). Unfortunately, there are no available short-period data at distances around 155° for the events in this paper. Nevertheless, we included a record at a similar distance (Δ=156.8°) for a sample beneath the south polar region (see Figure 2.15). The record is the short-period vertical component of WWSSN station ARE (Arequipa, Peru) for the Java Sea event on January 17, 1965, with a source depth of 246 km. The amplitude ratios of BC over DF and BC over AB in this record are much larger than the ratios in the Choy and Cormier's record. The difference of about 400 km in source depths of these two events can only generate slight changes in the ratios in synthetics, which can hardly account for the differences in the amplitude ratios of these two records. This demonstrates that the ratios are laterally varying. It is hoped that a stronger constraint on the velocity gradient can be reached by modeling high-quality broadband or short-period record section sampling a small region of the inner core at distances beyond the triplication.

Figure 2.15 shows the comparisons of the ARE record with synthetics (dashed lines) for the three different models. Note that the amplitude ratio BC/AB is too small in PREM, slightly too small in PEM, and slightly too large in PMNA. Thus the velocity gradient at the bottom of the outer core should be somewhere between PEM and PMNA. Comparing the differential travel times between different pulses, we find that all three models are about right for AB − DF. But both PEM and PMNA are too small for AB − BC, while PREM is good. Possible explanations for

Figure 2.15: Comparisons of synthetics (dashed lines) of the three models (Figure 2.2) and the short period WWSSN record (solid lines) at station ARE (Δ=156.8°) from January 17, 1965, Java Sea event. The data are shifted to align with the synthetics. Note that the amplitude ratio BC/AB is too small in PREM, slightly too small in PEM, and slightly too large in PMNA. Also note that differential travel time AB $-$ BC is too large in both PEM and PMNA.
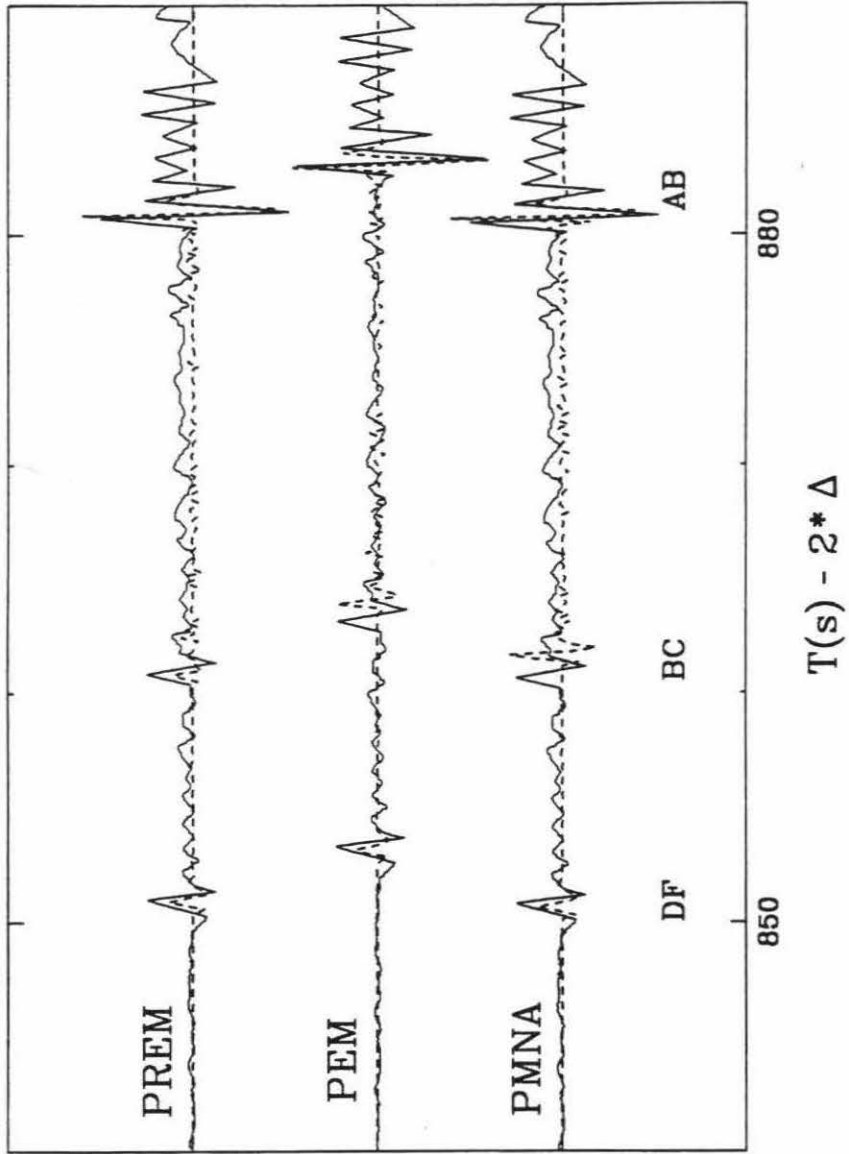
these differential travel time discrepancies are as follows. (1) The velocity at the bottom of the outer core is too small in PEM and PMNA, so that BC is delayed with little effect on DF and AB. (2) PEM and PMNA are right for BC (i.e., if we line up with BC), but wrong for both DF and AB. In this case, both the velocity at the top of the outer core and in the inner core should be reduced. Note that the raypath of this record sampled a slow region in the inner core from *Cormier and Choy* [1986]. On the other hand, there are strong suggestions that PREM's outer core is too fast in general [*Hales and Roberts*, 1971; *Lay and Helmberger*, 1983c]. (3) Lateral variation in D'' could be causing these differential travel times to scatter, since the raypaths cross D'' in different places, as discussed earlier. All of these issues can be addressed with more complete record sections, which will be reported in future efforts.

2.7 Conclusions

Waveform modeling of seismic sections has proved to be a valuable tool in defining the structure of the ICB. As an exercise of this approach, a model near the ICB is developed based on comparisons of synthetic and observed long-period and short-period PKP seismic sections for a sample of the ICB beneath the North Pacific. The model requires no transition zones. P velocity is 10.22 km/s on the upper side and 11.0 km/s on the lower side with a jump of 0.78 km/s at the boundary. A low P velocity gradient occurs above ICB, and a relatively high P velocity gradient occurs underneath. This model indicates inhomogeneous stratification in the lower part of the outer core. Possible heterogeneity near the ICB exists. Many more investigations have to be carried out to establish the exact nature of the boundary as opposed to the lateral variation in shallower structure near the CMB.

Chapter 3

A P-wave Velocity Model of the Earth's Core

3.1 Abstract

Present Earth core models derived from the retrieval of global Earth structure are based on absolute travel times, mostly from the International Seismological Center (ISC), and/or free-oscillation eigenfrequencies. Much core phase data is left out in these constructions, e.g., PKP differential travel times, amplitude ratios and waveforms. This study is an attempt to utilize this additional information to construct a consistent core model which fits the average of all the data. As a result, a one-dimensional P-wave velocity model of the core, PREM2, is proposed. This model, modified the Preliminary Reference Earth Model (PREM) [*Dziewonski and Anderson*, 1981], shows a significantly better fit to the combined data set than any of the existing core models. Major features of the model include a sharp velocity discontinuity, with a large jump (0.78 km/s), and a low velocity gradient at the base of

the fluid core. The velocity is nearly constant over the lower 100km of the outer core, indicating inhomogeneity is practically inevitable. The model features a strong depth dependent Q-structure in the inner core such that a constant t* for the inner core fits amplitude ratios and waveforms of short-period waves moderately well. This means the top of the inner core is more attenuating than deeper part of the inner core. In addition, the P velocity in the lowermost mantle is reduced from PREM to satisfy the separation of DF and AB branches at large distances.

3.2 Introduction

Recent studies show that waveforms and differential travel times of PKP phases provide a useful means to constrain the detailed structure of the core and the lowermost mantle [*Song and Helmberger*, 1992; 1993a]. In this paper we propose a spherically symmetric one-dimensional (1-D) P-wave velocity model of the lowermost mantle and the core along with a simple P-wave attenuation model of the inner core from these PKP phases. We use PREM [*Dziewonski and Anderson*, 1981] as the starting model and derive a consistent 1-D model that satisfies, simultaneously, differential travel times, amplitude ratios and waveforms of all branches of the PKP phases from the data we analyzed. As a first geometric ray arrival after the core shadow zone, PKP is observed throughout the distance range of around 120° to 180°, thus providing a unique data set to study the structure the Earth's deep interior. Figure 3.1 shows the ray paths of various branches of PKP phases. The D'' region is highlighted to indicate the complex structure presently known. Figure 3.2 shows the travel time curve of these PKP phases for a surface focus: PKP-AB, PKP-BC, PKIKP (or PKP-DF) and PKiKP (or PKP-CD). The dashed line beyond the C-cusp is the diffracted

wave PKP-C$_{diff}$ which propagates along the inner core boundary (ICB). It consists of an important data set in constraining the structure above the ICB, which will be discussed later. The distance range is limited to 130° to 165° in this study.

This work is motivated by the fact that present Earth core models, derived in the framework of global Earth structure, are based on absolute travel times (mostly from ISC) and/or free-oscillation eigenfrequencies. The addition of differential travel time, amplitude and waveform information proves crucial in testing and refining detailed structure of the Earth's core, particularly near the inner core boundary and the core-mantle boundary. Recent studies suggest that there is ample room to improve model parameters, e.g., a regional waveform study of PKP phases from *Song and Helmberger* [1992].

Our data contain a mixed set of digital and analog records consisting of both short-period and long-period seismograms. Differential travel times and amplitude ratios are derived from short-period GDSN records in CD-ROM from 1980 to 1986. Waveform data include short-period GDSN seismograms and short and long-period WWSSN record sections from two events. Fig 3.3 shows the ray coverage of the data used. The dashed lines indicate GDSN paths for which BC/DF amplitude ratios are derived. The solid lines are GDSN paths for which differential PKP travel times are picked. They are a subset of paths used for defining amplitude ratios. The dotted lines show ray paths of WWSSN record sections for two events from Java and Tonga, respectively. The ray coverage is somewhat restricted because of distribution of earthquakes and stations and data quality. Only differential travel times with cross-correlation coefficients larger than 0.5 were used. Thus it should be realized that although the data quality is high, our modeling results could be biased by the

Figure 3.1: Ray paths of PKP phases used in this study.

Ray paths of PKP phases

PKiKP

PKP$_{AB}$

PKP$_{BC}$

(PKIKP)

PKP$_{DF}$

inner core

outer core

mantle
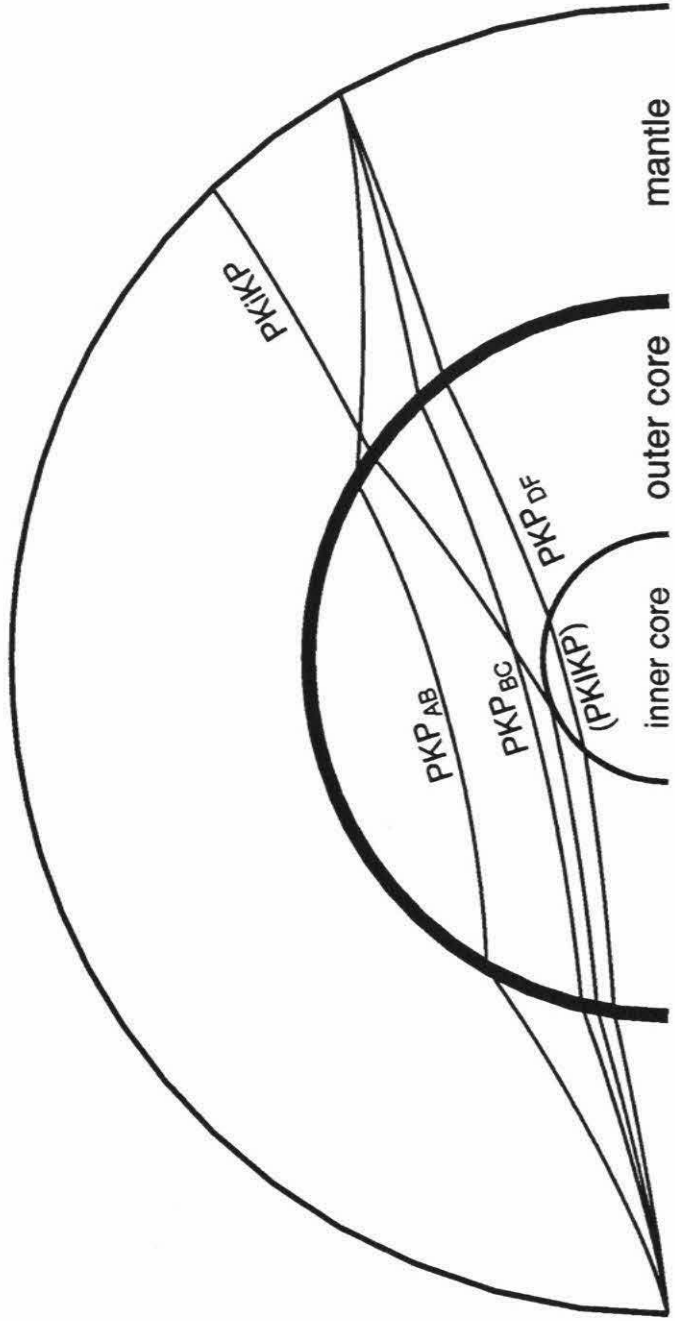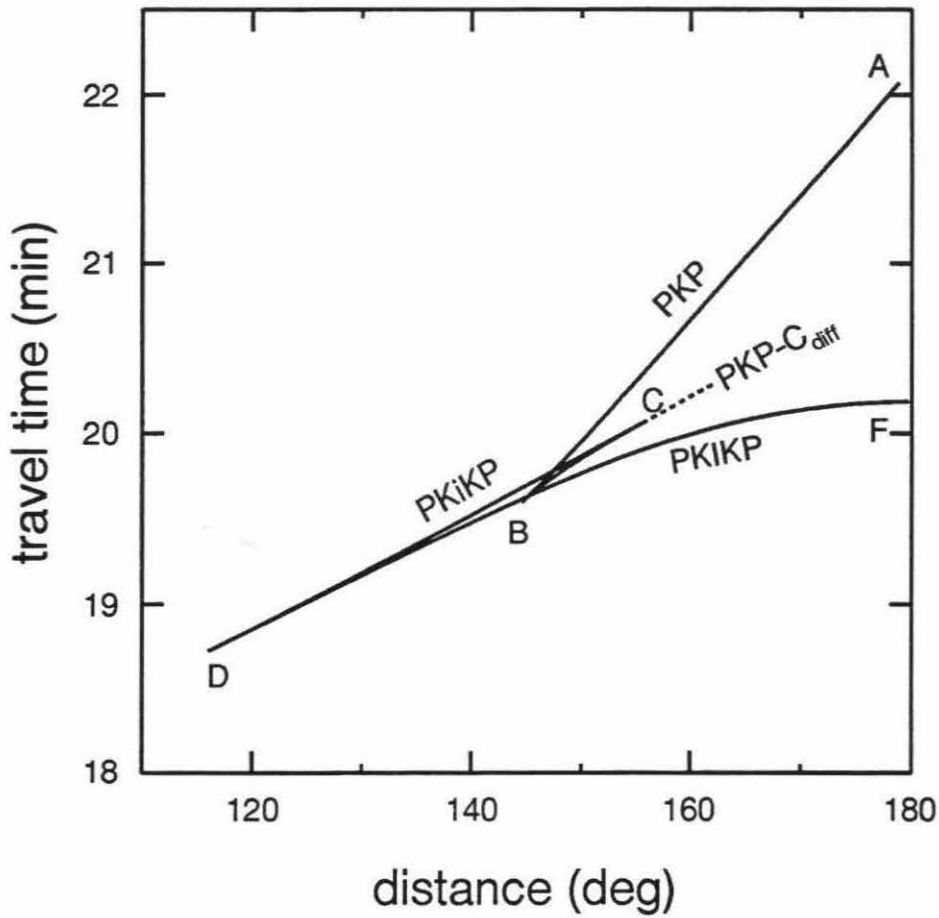
Figure 3.2: Travel time curves of PKP triplications from the Earth's core model of this study (PREM2) for a surface focus. The dashed line PKP-C$_{diff}$ is the diffraction propagating along the inner core boundary.

limited data set. However, the model developed largely from the GDSN data set appears to satisfy samples of the WWSSN data.

Figure 3.4 shows our model PREM2 in comparison with the starting model PREM. A variety of the observations, as mentioned above, were used not only as a way for checking the self-consistency of the model but also as an effective way to constrain the model due to the different sensitivities of the data to the velocities in various regions. This work pieces together our previous results near the ICB [*Song and Helmberger*, 1992] and the D'' [*Song and Helmberger*, 1993a] with modifications to fit the average of a larger data set. The major features of PREM2 include the following. (1) It has an average velocity lower than PREM in D''. The velocity is reduced by about 1.5% in the lowermost 350km of the mantle. $AB - DF$ differential travel times are very sensitive to the velocity in this region and have been used to explore possible lateral variations in D'' [*Song and Helmberger*, 1993a]. (2) It has a large velocity jump at the inner core boundary (0.78km/s). Short-period PKIKP and PKiKP waveforms from 130° to 140° are very sensitive to the jump at the boundary [*Cummings and Johnson*, 1988; *Song and Helmberger*, 1992]. This number is taken directly from the model PMNA by *Song and Helmberger* [1992], which fits a short-period LRSM record section from Indonesia to North America extremely well. Similar studies are required for other paths to investigate possible lateral variations. (3) The model has a near zero gradient at the bottom 150km of the fluid core. Travel times and amplitudes of PKP-BC and PKP-C_{diff} are very sensitive to the velocity gradient; thus, $BC - DF$ (or PKP-$C_{diff} - DF$) and BC/DF (or PKP-C_{diff}/DF) provide strong constrains. (4) It has a nearly constant $t^*=0.35$s for the inner core attenuation, which means a strong depth dependent Q-structure
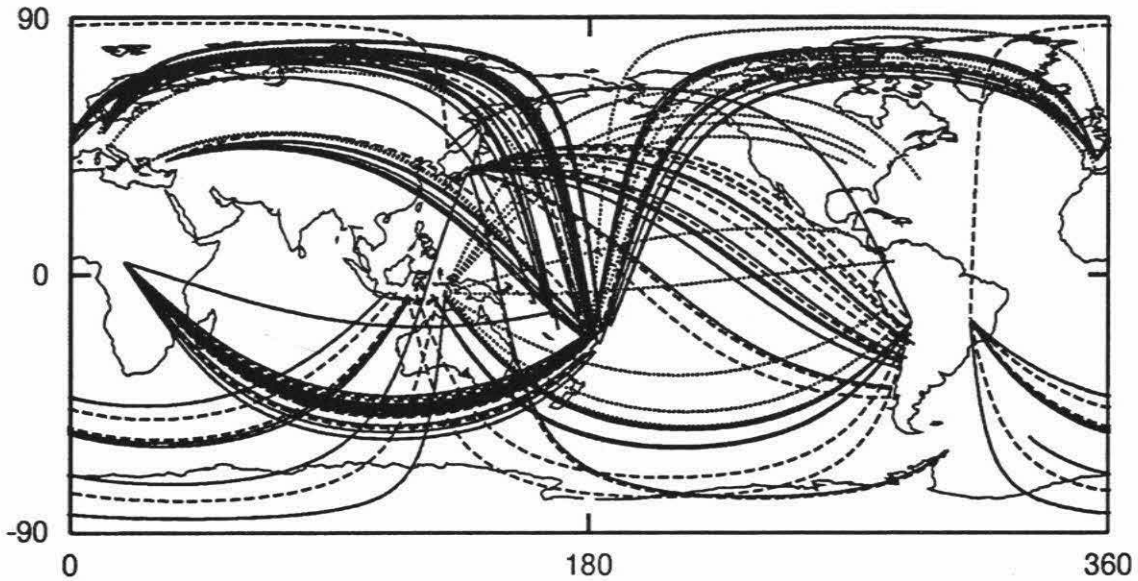
Figure 3.3: The ray coverage of the data used in this study. Dashed lines are GDSN paths for which PKP amplitude ratios are picked. Solid lines are GDSN paths for which differential PKP trav el times are picked. Dotted lines show ray paths of WWSSN record sections for two events from Java and Tonga, respectively.

in the inner core. Using this velocity model, the attenuation at the top of the inner core was estimated from the BC/DF amplitude ratios from 148° to 158°. A constant t*=0.35s fit the observations reasonably well.

Figure 3.5 shows our preferred model along with some other global models. The zero line is the reference model PREM. All the other models are plotted with respect to PREM to highlight the differences near the core-mantle boundary (CMB) and the inner core boundary (ICB). The models include PEM [*Dziewonski et al.*, 1975], derived from observations of eigenfrequencies, surface wave dispersion data and body wave travel times, IASP91 [*Kennett and Engdahl*, 1991] and SP6 [*Morelli and Dziewonski*, 1993], derived from body wave travel times from ISC. Note that IASP91 uses PEM core model.

In the following, we present the details of the model development and give justifications for the above conclusions and discuss limitations of any 1-D model in describing the Earth. One immediate problem is the anisotropy of the inner core. There is increasing evidence that the inner core is anisotropic with the direction parallel to the spin axis being fast [*Shearer et al.*, 1991; *Creager*, 1992; *Tromp*, 1993; *Song and Helmberger*, 1993b]. Our recent systematic search for data that samples paths nearly parallel to the spin axis confirms that these polar paths are indeed anomalous. Waves that travel parallel to the spin axis in the upper part of the inner core are on average 3% faster than waves that travel perpendicular to it. However, this anisotropic effect is apparent only for polar paths with ray angles from the spin axis less than about 40°. Because of limited earthquake and station distributions, these polar paths account for only a small portion of PKP recording. For non-polar paths, which include all the paths in this study, this effect is within the scatter of
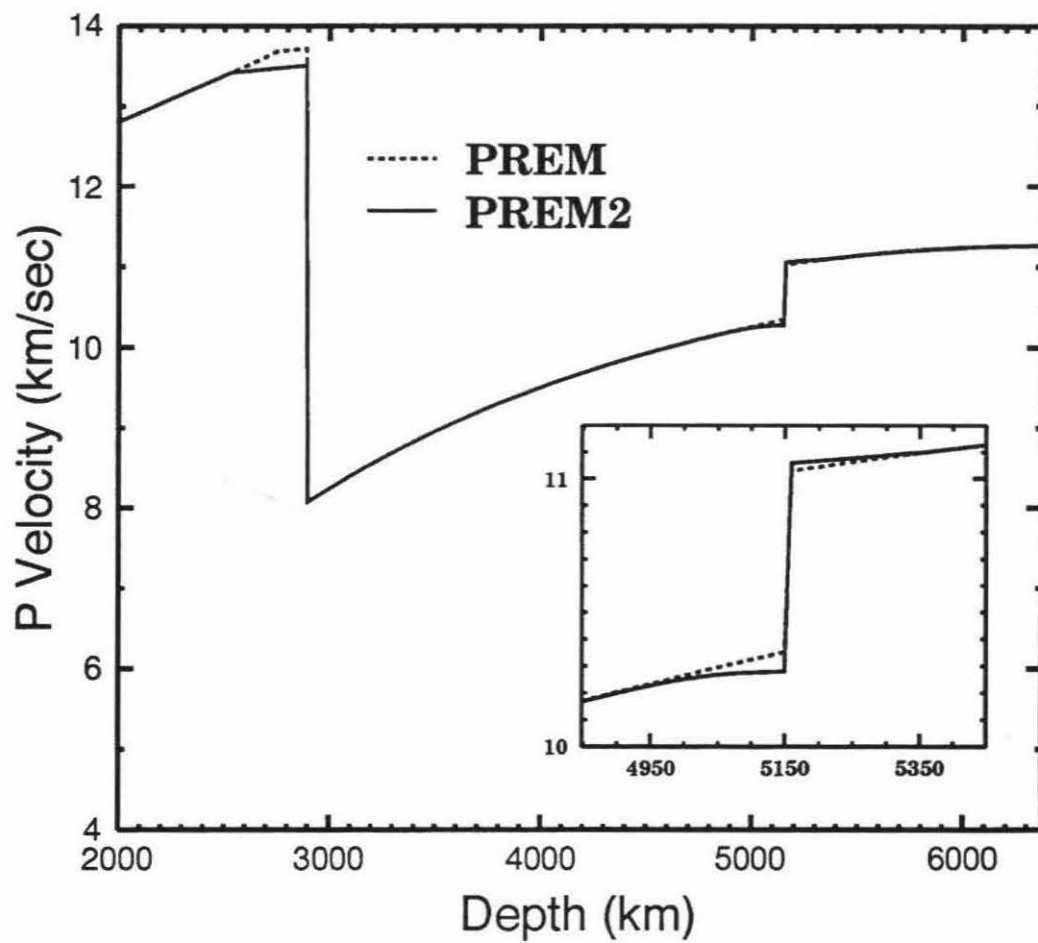
Figure 3.4: P-wave velocity model PREM2 of this study (solid) modified from PREM (dotted).

Figure 3.5:   P-wave velocity models used in this study, PEM [*Dziewonski et al.*, 1975], PREM [*Dziewonski and Anderson*, 1981], IASP91 [*Kennet and Engdahl*, 1991], SP6 [*Morelli and Dziewonski*, 1993]. The models are plotted relative to PREM.

the data. Thus, in this study, we are averaging only non-polar paths for the inner core.

3.3 Modeling Results

Our strategy in modeling the data is basically a three-step trial-and-error procedure. First, we determine preliminary models that satisfy the travel time differentials between the various branches of PKP. Secondly, we generate synthetics for these models and eliminate those models that do not fit the amplitude ratios of the corresponding three arrivals (DF, BC and AB). Thirdly, the waveform comparisons were used to re-examine the preferred model.

Like any other forward modeling approach, finding a model by trial-and-error that fits all observations can be tedious and time-consuming. To aid our modeling practice, an interactive model design software is developed, which allows us to manipulate velocity profiles easily. Particularly, Bézier curves are used to model smoothly varying velocity profile. Bézier curves are widely used in computer graphics and computer aided designs (CAD) because only a few points are needed to model a complex shape and the tangent vectors at end points can be easily modified by the control point or points in between [e.g., *Mortenson*, 1985]. A brief description of Bézier curves is given in Appendix A. Thus, they are very useful in fine-tuning the velocity gradient at the base of the outer core. Table 3.1 shows model parameters of PREM2 in the form of polynomials. The current model represents the best fitting model of dozens of test models. The lowermost mantle and the top of the outer core are linear fits. The Bézier curve for the velocity profile at the base of the outer core is approximated as a third order polynomial. Appendix B gives the control points of

the Bézier curve and the accurate values of the model in 10km intervals. The travel times predictions of the PKP phases for the PREM2 are given in Appendix C.

3.3.1 Differential Travel Times

The differential travel time results are summarized in Figures 3.6, 3.7, 3.8. The solid dots are the observed differential travel times. The data are averaged in two degree intervals with the error bars showing two standard deviations. The various lines show the predictions from different models as indicated in the legend boxes. In particular, predictions from our new model PREM2 are shown by solid lines. Note that the diffractions beyond the C-cusp (PKP-C_{diff}) are shown as long dash lines for all the models in Figure 3.6 and 3.8. The travel times of these diffractions are calculated from synthetic seismograms. We see that predictions from PREM2 fit the average of the observations fairly well for all the three data sets.

Figure 3.6 shows the comparisons of the observations and predictions from various models for $BC - DF$. As mentioned earlier, $BC - DF$ is useful in constraining the structure near the ICB. The predictions from PREM are smaller by about 0.3s than the data average at distances larger than 150°, whereas the predictions from IASP91 and PEM models are larger than the data by about 0.6s. The latter two models agree because the IASP91 model adopted the core model in PEM. The predictions from model SP6 are smaller than the data by 0.5s to 0.8s. The smaller core radius and lower velocity at the top of inner core of the model slows DF down, thus decreasing the $BC - DF$ differential times. The predictions from PREM2 and a sensitivity test model from *Souriau and Poupinet* [1991] (hereafter denoted as S-P91) fit the average of the data very well at larger distances. Both models have a similar flat

depth(km)	radius (km)	V_p (km/s)
2531.0 - 2891.0	3840.0 - 3480.0	14.2743 $-1.3998x$
2891.0 - 4749.5	3480.0 - 1621.5	11.0487 $-4.0362x$ $+4.8023x^2$ $-13.5732x^3$
4749.5 - 5149.5	1621.5 - 1221.5	4.0354 $+82.008x$ $-347.769x^2$ $+468.786x^3$
5149.5 - 5361.0	1221.5 - 1010.0	11.3041 $-1.2730x$
5361.0 - 6371.0	1010.0 - 0.0	11.2622 $-6.3640x^2$

Table 3.1: P velocity model of the Earth's core PREM2. The polynomial for the depth range of 4749.5 to 5149.5km just above the ICB was an approximaton to the velocity expressed by a Bézier curve. The control points of the Bézier curve and the velocity parameters are given in Appendix B.

velocity structure in the bottom 150km of the outer core. This velocity reduction effectively slows down BC relative to DF at larger distances, thus increasing BC − DF differentials. The velocity reduction in S-P91 model from PREM is proposed to fit BC and PKP-C_{diff} residuals at distances larger than 152°. However, the fits of S-P91 to BC − DF times at distances smaller than 150⁰ are less satisfactory. Some compensation is needed at the top of the inner core to speed up DF when BC is not affected by the reduced velocity at smaller distances.

Figure 3.7 shows the comparisons of the observations and predictions from various models on AB − DF. This data set is sensitive to the velocity in the lowermost mantle as well as the top of the inner core. We see that predictions from IASP91, PEM and PREM2 all fit the average of the data. SP6 underpredicts the average of the data by more than 0.5s while PREM underpredicts it by nearly a second. Because AB has a much greater incident angle than DF at the lowermost mantle, the velocity reduction in PREM2 in this region effectively slows down AB and thus significantly increases the AB − DF travel time. A simple linear structure is used in PREM2's lowermost mantle because the detailed velocity structure in this region, such as discontinuity and velocity gradient, is not constrained by the AB − DF differential times [*Song and Helmberger*, 1993a]. On the other hand, the velocity structure both in the lowermost mantle and the top of the inner core contributes to the differences between the PEM and PREM predictions. The velocity at the top of the inner core in PEM is significantly higher than in PREM which speeds up DF while the velocity in the lowermost mantle is significantly lower in PEM than in PREM which slows down AB. Similar reasoning can be applied to the comparison of IASP91 and PREM since IASP91 and PEM have the same core model. The only exception is that the

Figure 3.6: Comparisons of GDSN $BC - DF$ observations with predictions from various earth models. Compared with the data from 150° to 158°, predictions from PREM are too small while predictions from IASP91 and PEM are too big. SP6 underpredicts the data average by more than half a second. Both PREM2 and the model from *Souriau and Poupinet* [1991] (denoted as S-P91), which have a similar flat velocity gradient at the bottom of the outer core, fit significantly better than the other models.

$PKP_{BC} - PKP_{DF}$

PREM
IASP91
PEM
PREM2

Del (deg)

$T_{BC-DF} - 0.8(Del-150)$
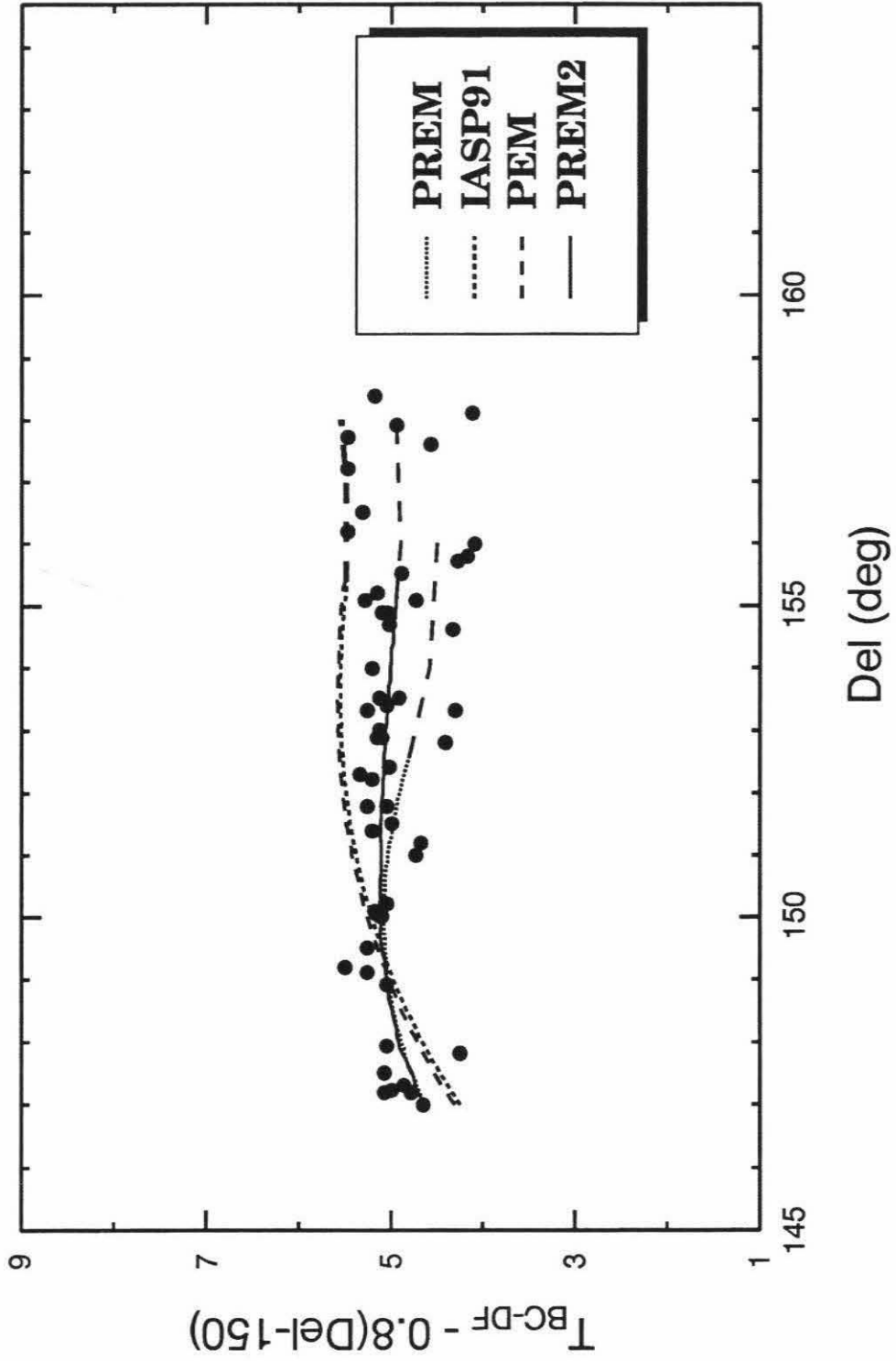
velocity structure in the lowermost mantle in IASP91 is closer to PREM than PEM. Comparing SP6 and PREM, although the slow velocity, negative gradient structure of SP6 in the lowermost mantle slows down AB considerably, it is partly offset by the slow velocity in the uppermost inner core.

Figure 3.8 displays the $AB - BC$ comparisons. This data set is sensitive to the velocity structure at the lowermost mantle and at the base of the outer core. It is impossible to judge which one contributes more from this data because of the trade-off in these two regions. This trade-off is made clear by comparing the predictions from PEM and PREM. The differences in $AB - BC$ from both models are much smaller than in $AB - DF$ because the velocity decease in the lowermost mantle in PEM is compensated by the velocity decrease at the base of the outer core. Furthermore, the two curves cross each other at about 152° because BC from PEM is slowed down considerably more at larger distances when it approaches the ICB.

3.3.2 Amplitude Ratios

Figures 3.9a,b show the amplitude ratios of BC/DF from the GDSN short-period records and synthetic predictions from PREM2. The observed amplitude ratios (shown by dots) are divided into two groups according to focal depths, shallower than 400km and deeper than 400km, to distinguish slight variations in amplitude ratios at different depths from synthetic predictions. While travel times primarily depend on velocity structure, amplitude ratios depend on attenuation structure as well as velocity. Assuming a velocity structure of the lowermost outer core and the inner core, it is possible to invert for the depth dependence of Q at the top of the inner core from BC/DF amplitude ratios. A simple experiment is shown in these fig-

Figure 3.7: Comparisons of GDSN AB − DF observations with predictions from various earth models.

$PKP_{AB} - PKP_{DF}$
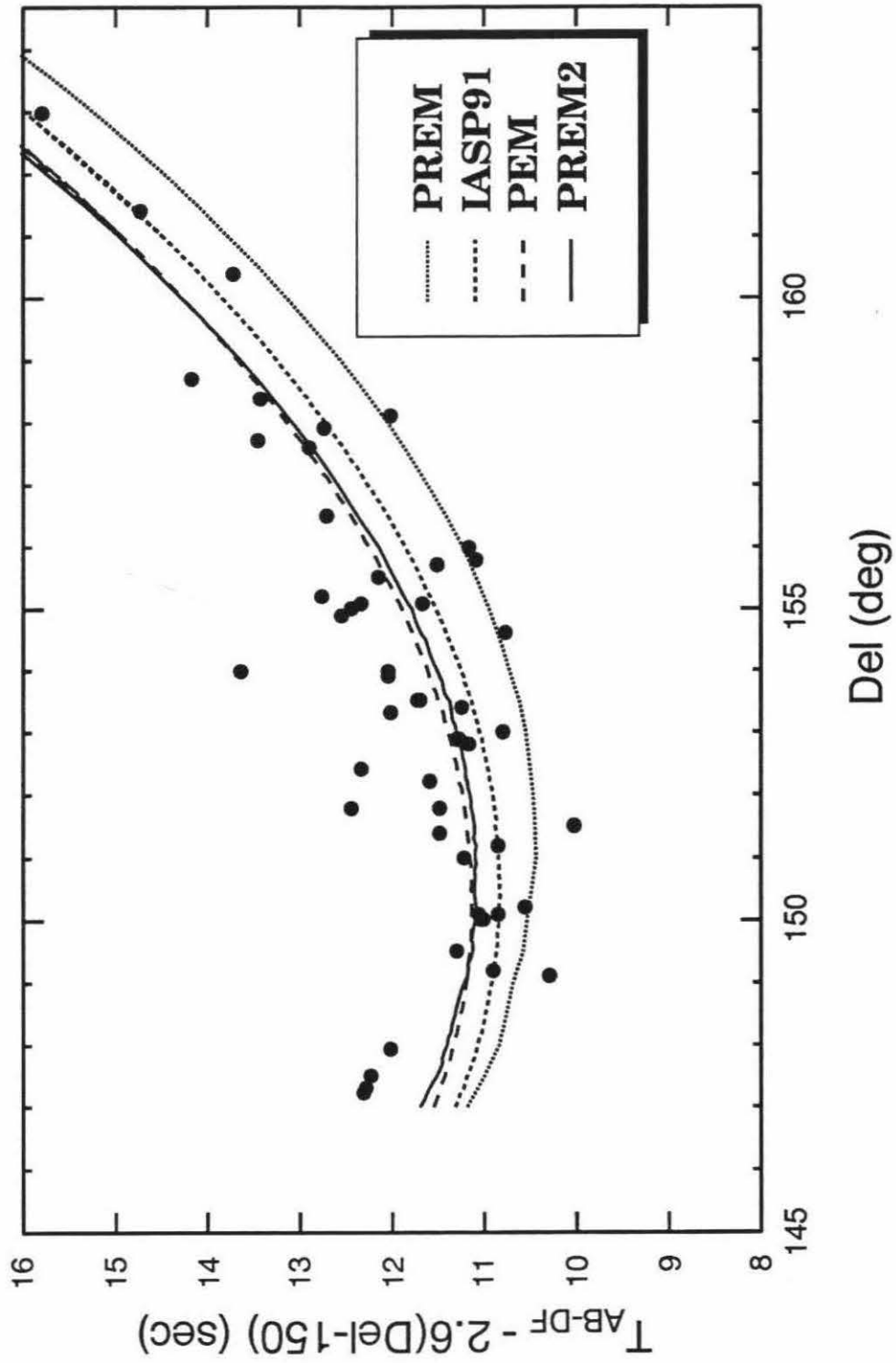
Figure 3.8: Comparisons of GDSN $AB - BC$ observations with predictions from various earth models.

$PKP_{AB} - PKP_{BC}$
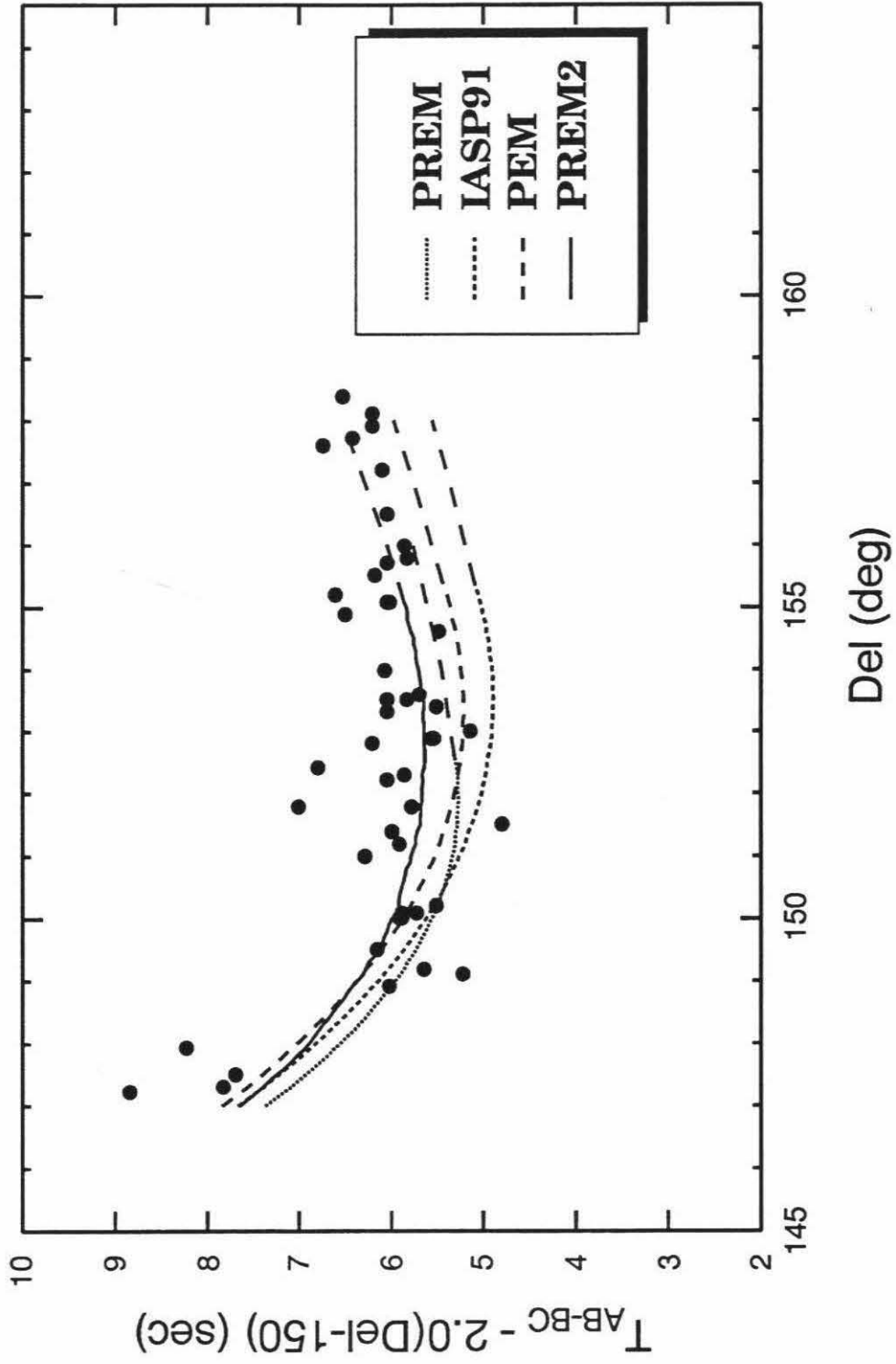
ures where a constant t* and a uniform Q are applied, using the velocity model from PREM2. The dotted lines show the synthetic amplitude ratios of BC/DF with a constant t*=0.35s. The dashed lines show the synthetic amplitude ratios of BC/DF with a constant Q=333, which was chosen to fit the observed ratios around 148°. Clearly, a uniform Q model is unlikely to to explain the amplitude ratios. The synthetic BC/DF ratio is more than 50% larger than the average observed ratio at 156°. Adjustment of the Q value to fit observations at large distances would significantly misfit observations at smaller distances. The fits from the constant t* model are good for the deep events (Figure 3.9b) and marginal for the shallow events (Figure 3.9a).

The constant t*=0.35s for the distance range 148° to 158° is used to invert for the inner core Q structures in the least-square sense (Figure 3.10). The inversion results with two different layer thickness at the top of the inner core are displayed. There is no sampling below 500km of the ICB. If we assume a constant Q below 500km of the ICB and the same constant t*=0.35s for the ray which goes straight through the center of the earth, the Q value would be about 940. At 136°, t*=0.35s for model A and 0.25s for model B. Considering LRSM short period records at distance from 130° to 136° which required t*=0.4s [*Song and Helmberger*, 1992], model A is better than B, i.e., a more strongly attenuating thin layer at the top of the inner core is favored.

The observed amplitude ratios of BC/AB and DF/AB are less useful for our purpose. They show much larger scatter than BC/DF ratios due to larger influence of heterogeneity of the lowermost mantle and/or radiation patterns on AB relative to DF or BC. The scatter of DF/AB amplitude ratios have been used to map the heterogeneity of the lowermost mantle by *Sacks et al.* [1979].

Figure 3.9: Comparisons of GDSN BC/DF observations with synthetic predictions from PREM2 model. a) The event depths are shallower than 400km. The synthetics are for source depth at 200km; b) The event depths are greater than 400km. The synthetics are for source depth at 600km. A constant differential $t^*=0.35$s and a constant Q in the inner core were applied to DF of the synthetics, respectively. Although there is room for improvement, the constant t^* model provides fair fits to the amplitude ratios. A uniform Q model is unlikely to explain these amplitude ratios.

a)

PKP_{BC}/PKP_{DF}

Amplitude ratio

Del (deg)

- obs 0-400km
······ const t*=0.35s
--- const Q=333

b)

PKP_{BC}/PKP_{DF}

obs 400-700km
const t*=0.35s
const Q=333

Del (deg)

Amplitude ratio
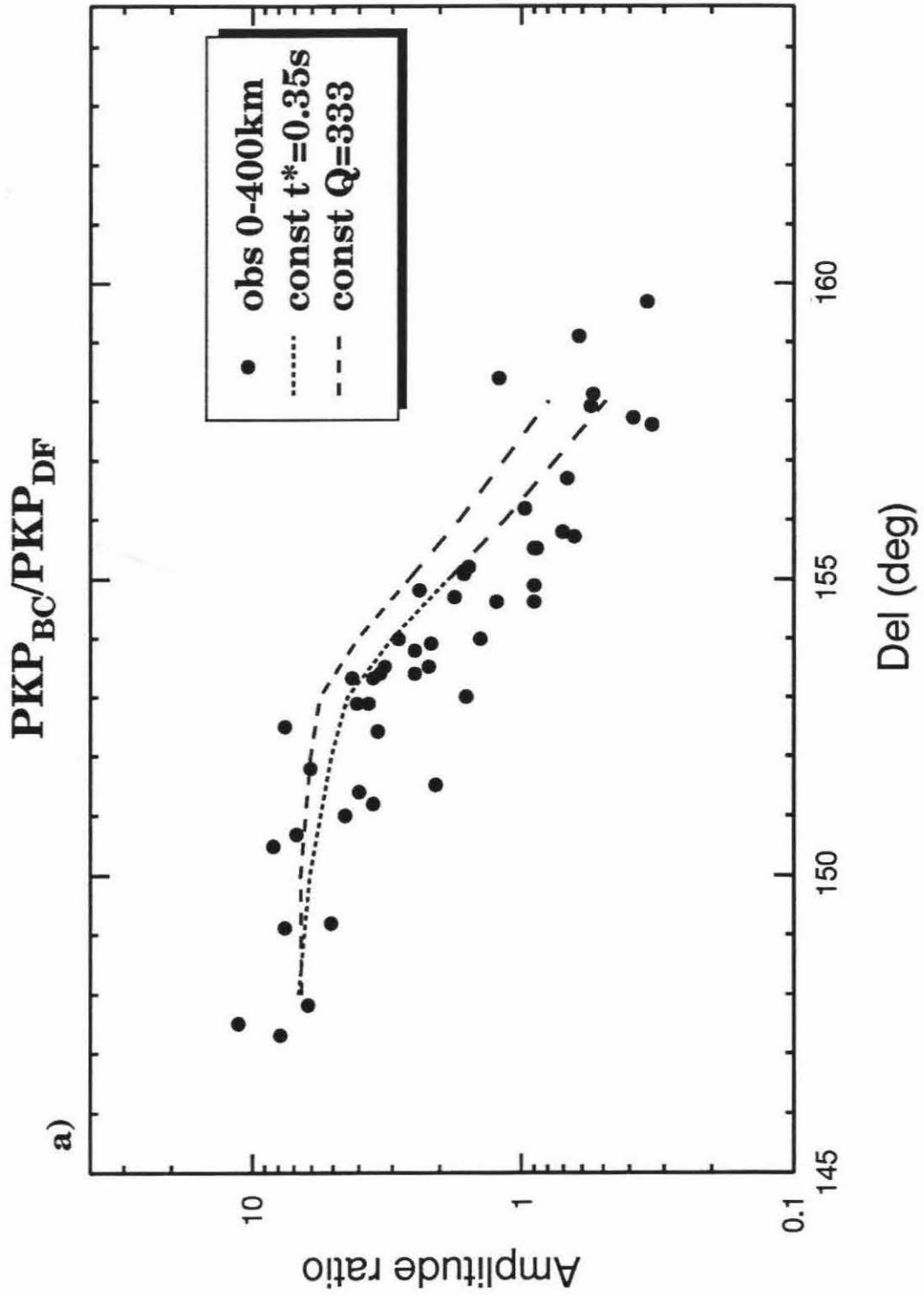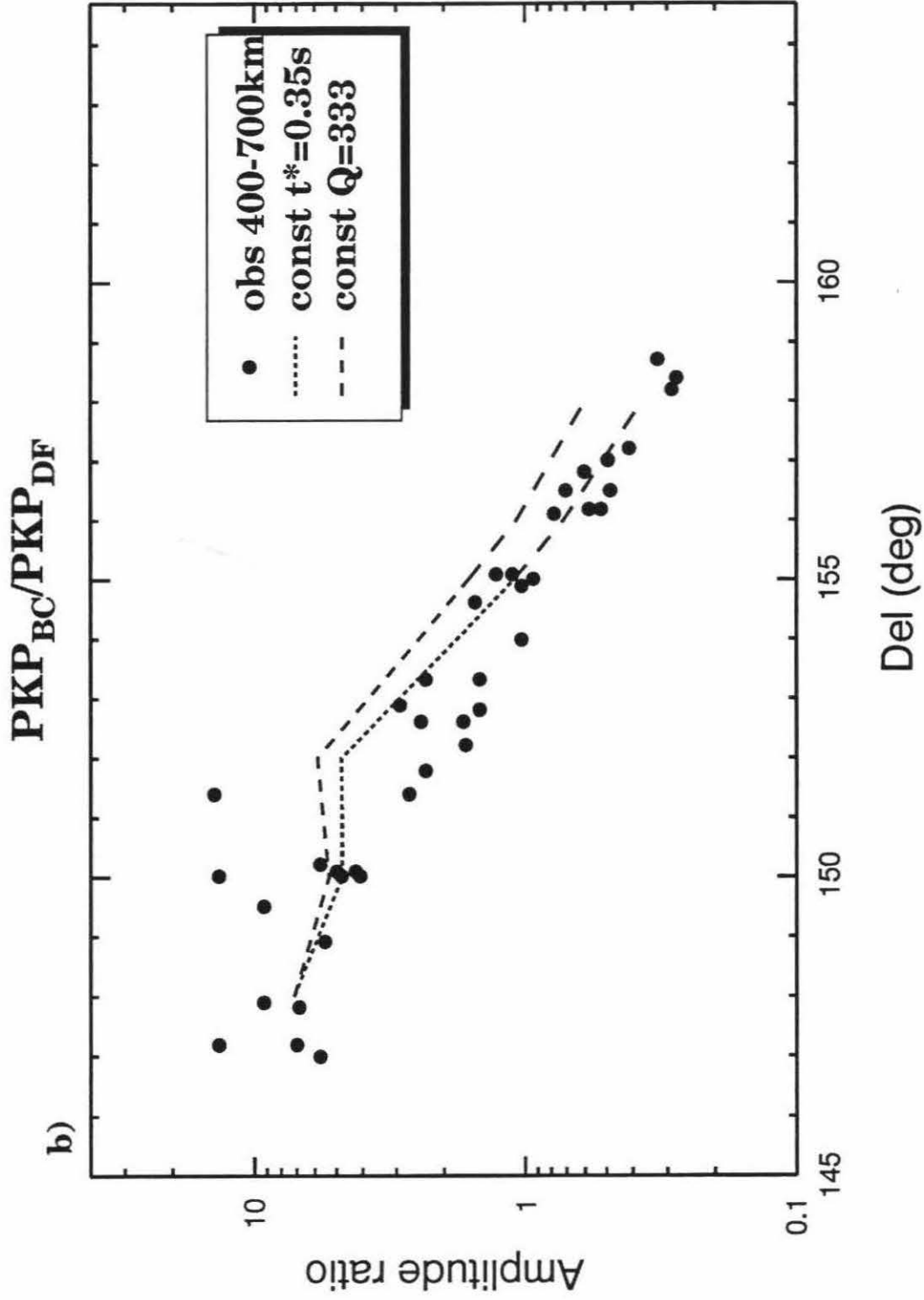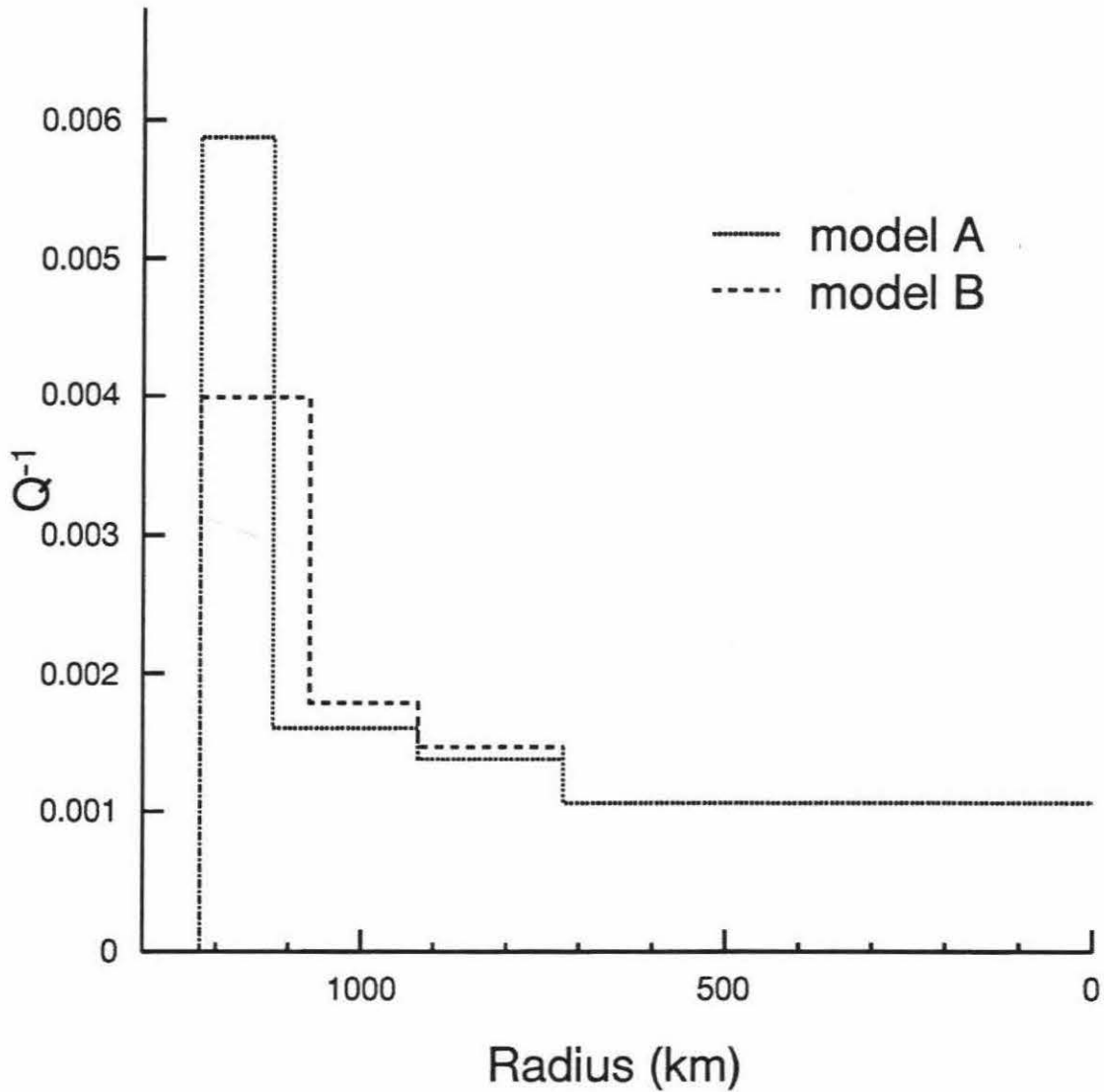
Figure 3.10: Q structure in the inner core. The constant t*=0.35s from distant 148°
to 158° is used to invert Q structures in the least-square sense. The inversion results
are displayed with two different layer thicknesses at the top of the inner core.

3.3.3 Waveform Studies

Ultimately, of course, we should be able to model the waveforms of these core phases. The advantage of using waveforms is that waveforms contain much more information than mere travel times and amplitudes as demonstrated in numerous modeling studies. Since variations of waveforms are commonly found for different sampling paths, it is not practical to model every detail of seismograms. Rather, we strike to examine the adequacy or inadequacy of using a spherically symmetric 1-D model to represent the Earth's core structure by comparing the waveforms of the data and the synthetics.

Fig. 3.11 shows comparison of GDSN short-period records from earthquakes at depths of around 150km with generalized ray synthetics from PREM2. The synthetics are computed at the depth of 150km for all the traces except the trace at 160°, which is computed at 250km. Amplitudes are normalized relative to BC at distances smaller than 154° and relative to DF at distances larger than 154°. A constant $t^*=0.35$s has been applied to the synthetics. The synthetics generally resemble the observations, especially the decaying amplitudes of PKP-C_{diff} at distances larger than 154°.

While the observations displayed in this figure proved useful in determining relative timing and in amplitude control, they are less useful in waveform modeling. This short-coming is caused by the lack of source control since every observation is from a different event with its unique source time function. Thus, the more dense network of analog stations, such as WWSSN and LRSM, has distinct advantages in waveform comparisons because the same source can be used and a record section constructed.

Figure 3.11: Left: A combined short-period GDSN record section from various events with focal depths around 150km. The event dates, depths and station names are printed near the records. Right: synthetics from model PREM2 at depth of 150km except the last trace at 160°, which is computed at 250km.

DATA

PREM2

146

821026 BDF 153km

148
850827 ANTO 36km

801130 GRFO 202km

150
830523 MAJO 110km

800120 ZOBO 110km

830820 BDF 156km
152

830821 GRFO 151km

154
830404 TOL 123km

800719 MAJO 110km

156
830815 TOL 182km

840717 MAJO 120km

158
830415 TOL 227km

850915 BCAO 282km
160
830415 BCAO 227

Δ (°)

D B

F C A

0   10   20   30   40   50   60
T (sec)

0   10   20   30   40   50   60
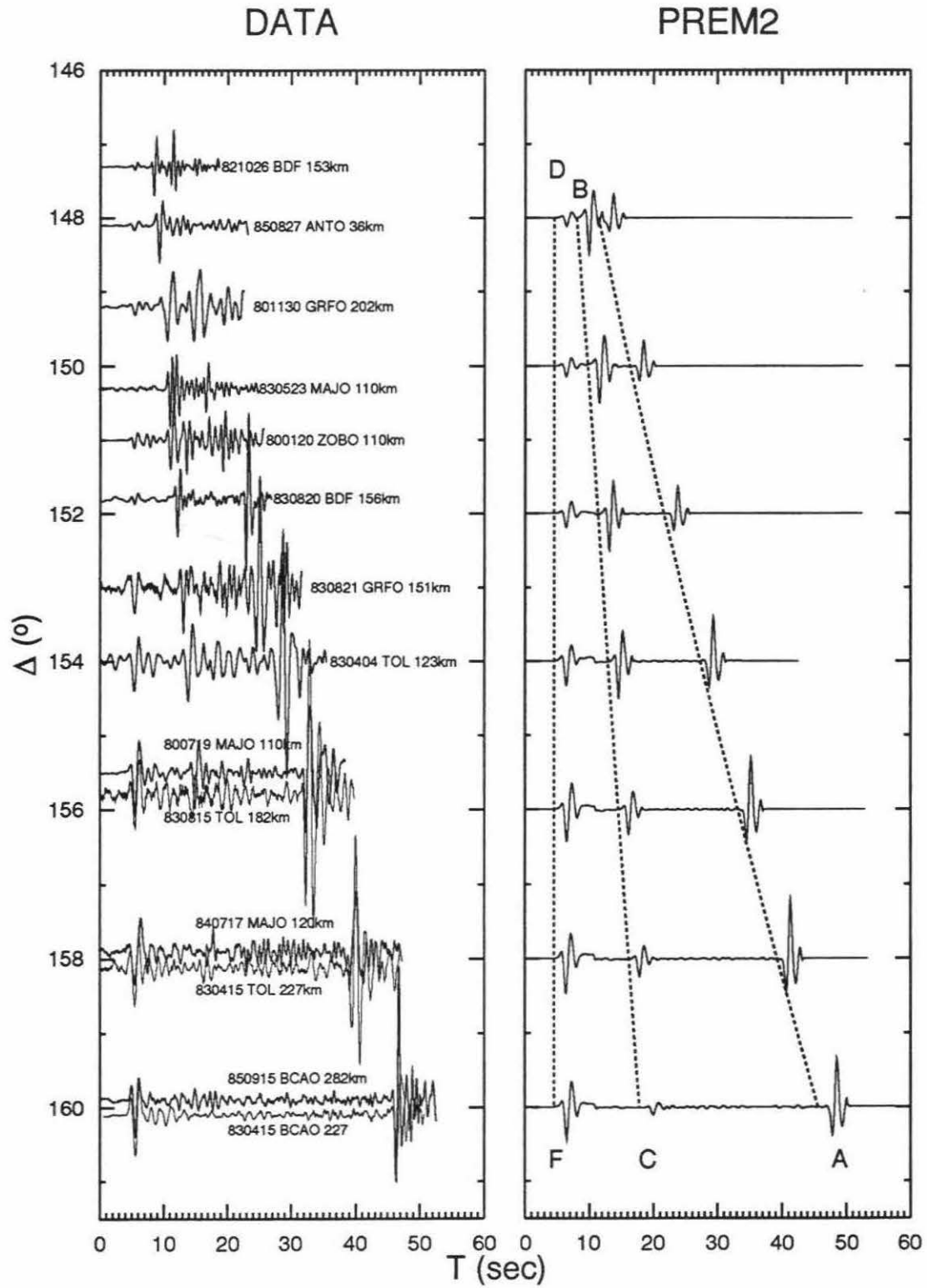
Figure 3.12 shows example fits of synthetics from PREM2 (dashed) to long-period WWSSN records (solid). The event is from West Tonga on March 17, 1966 with a focal depth of 627km. The observed waveforms were shifted to line up with the DF arrivals of the synthetics. Both data and synthetics are normalized to peak-to-peak amplitudes. We see excellent fits throughout the distance ranges except for the two stations PTO and TOL. The differential travel time of AB − DF for these two stations are anomalously smaller that other stations by about 2s. Events from similar paths confirm this observations [*Song and Helmberger*, 1993a]. It appears that the anomaly comes from lateral variations in the lowermost mantle underneath the Mid-Pacific, a well-know complex structure as reported by *Su et al.* [1992] and others. These shifts of AB and DF differential travel times are quite common for long-period records worldwide. However, much more data sampling and waveform modeling are required to map the details of these anomalous structures.

For this purpose, broadband modeling has particular advantages since shorter wavelengths are involved and better resolution can be obtained. The broadband data provided by the new digital systems are ideal but not very much data presently exist, especially on a global scale. Thus, working with the combined short and long-period WWSSN observations from the same event is motivated. An example of such data from an event occurring beneath Java (March 19, 1967; focal depth 89km) is displayed in Figures 3.13a,b. The data are shifted to line up with BC arrivals and normalized to peak-to-peak amplitudes. Note that records from station BEC (marked in thinner lines) have been shifted 2 degrees to a larger distance to distinguish traces from LPB at the neighboring distance. The fits for short-period records are excellent in PKIKP (DF), PKiKP (CD), and BC waveforms. The PKIKP

Figure 3.12: Comparisons of long-period WWSSN records (solid) from Mar 17, 1966

Western Tonga event (h=627km) and synthetics from PREM2 (dashed).

Model PREM2
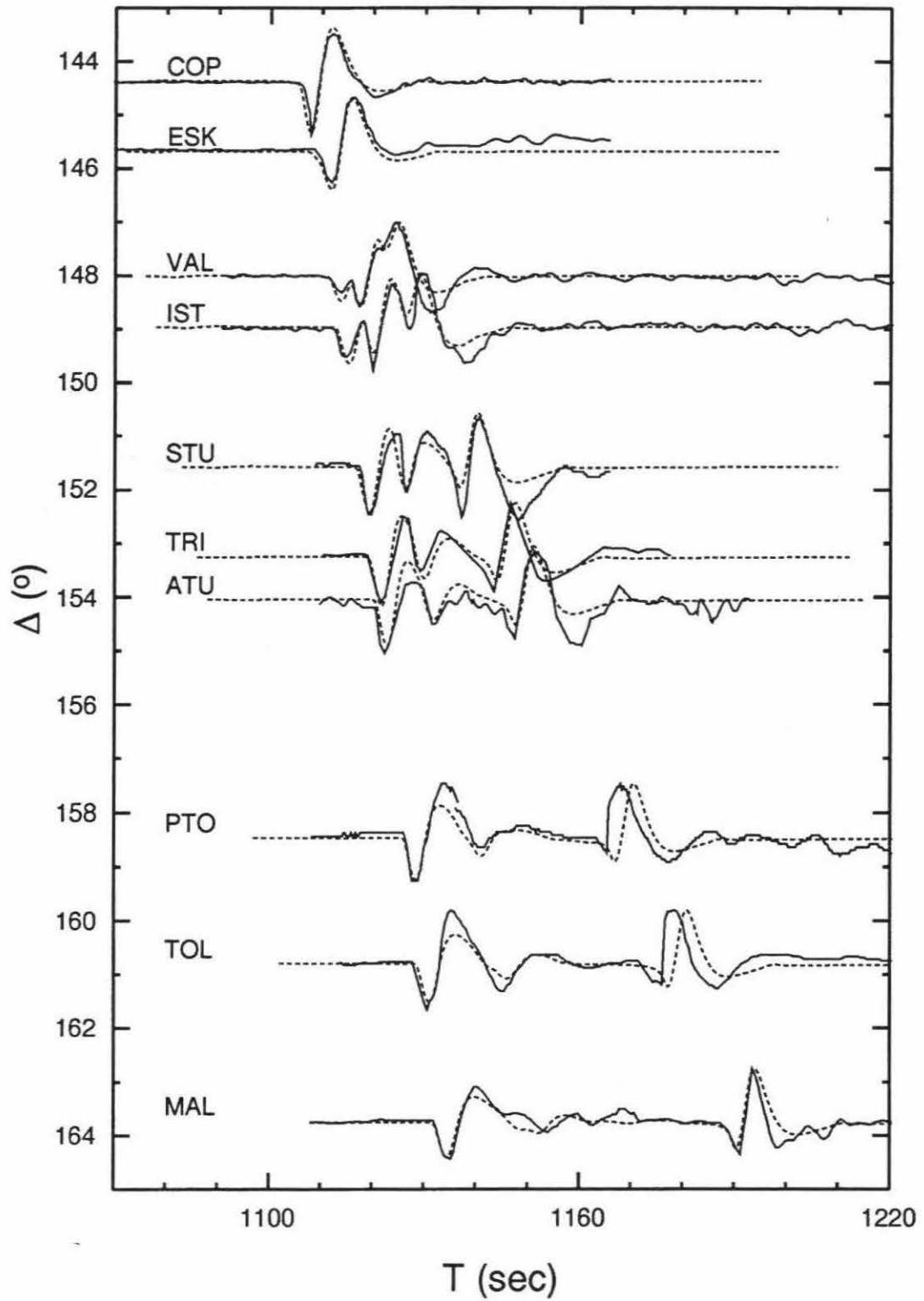
and PKiKP arrivals are distinctly observed in the short-period records between 130°
and 140° and are correctly modeled by PREM2. The agreement provides a good
test for the velocity and attenuation structure from bottom 400km of the outer core
to top 400km of the inner core where these rays sample. The fits for AB arrivals
vary, however. For example, AB arrivals slightly earlier at ARE and much later
at BOG (by 1.5s) than synthetics. The fits in the long-period record sections in
Figure 3.13b are less impressive. The data are not the best quality as the noise
level is high. However, AB arrivals are clearly late by about 1.0s at BOG. The
variations of AB phase in timing and in amplitudes displayed in these records have
been observed in bigger data sets of AB − DF and DF/AB and have been interpreted
as the influence of lateral heterogeneity in the lowermost mantle [*Sacks et al.*, 1979;
Song and Helmberger, 1993a], pointed out earlier in the text.

3.4 Concluding Remarks

Resolving the detailed seismic properties of the core remains integral in understand-
ing the dynamics of the Earth. This is especially true at the boundaries, CMB
and ICB, where the properties near boundary layers provide constraints on compo-
sitional and thermal effects. In this study, we have presented our best 1-D structure
to be used by other scientists in their quest for meaningful physical models and as a
reference in comparing other seismological data.

Since PREM has proven quite effective in other studies, we have attempted to
keep most of its structure intact. For example, a recent paper by *Garnero et al.*
[1993a] discovered that multiple SmKS waves for m=2,3,4 are commonly observed at
large ranges, where m − 1 denotes the number of times this phase reflects beneath the

Figure 3.13: Comparisons of short- and long-period WWSSN records (solid) from Mar 19, 1967 Java event (h=89km) and synthetics from PREM2 (dashed). The BEC records (thin lines) are shifted down 2 degrees for better reading.
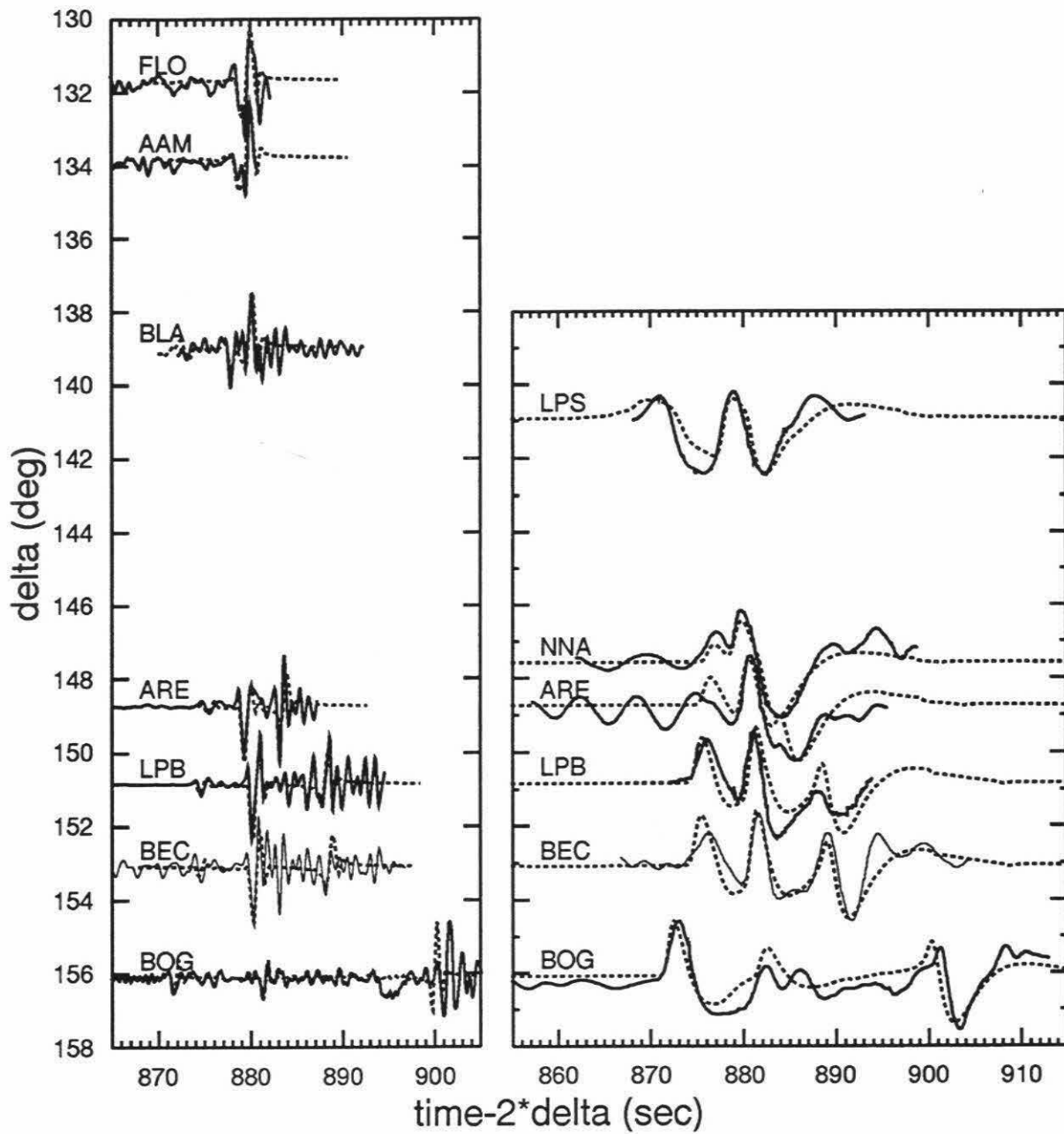
CMB. The timing between these multiples provides an excellent tool for determining the upper part of the outer core velocity structure. Predictions from PREM generally fit well both in timing and in waveform. However, PREM does appear too fast in the lowermost mantle, D'' as demonstrated recently by *Song and Helmberger* [1993a]. Thus, the separation between the PKP phases, $AB - DF$ are about 2s too small at ranges greater than $150°$. But D'' displays so much lateral variation, it can hardly be considered 1-D, see *Kendall and Shearer* [1994] and others.

The only other changes to PREM occur near the ICB, where changes were made to satisfy the waveform data and differential timing. The most noticeable change occurs at the bottom of the outer core where the velocity gradient is reduced to near zero. This low gradient persists over the lower most 150km and produces satisfactory fits to our $BC - DF$ differential travel times. This model fits the *Souriau and Poupinet* [1991]'s BC times as well as the Engdahl's BC and $BC - DF$ times (personal communications) from ISC. This small velocity gradient in the lowermost outer core has also appeared in the literature from regional studies of PKP phases, e.g., Müller, 1973; Qamar, 1973; Song and Helmberger, 1992. In our previous model PMNA of the ICB [*Song and Helmberger*, 1992], a small velocity gradient over the lower 400km of the outer core was used to model the waveforms of the long-period diffraction from PKP B-caustic. The structure, however, is much broader than here in PREM2. The discrepancy is possibly due to path variations, limited resolution of long-period data as well as the trade-off between the mid-outer core and the lower outer core not explored in this study.

One difficulty of having a very low velocity gradient in this region is that it predicts a relatively strong PKP-C_{diff} beyond the C-cusp [*Choy and Cormier*, 1983],

which is not always observed. Because of the high sensitivities of these diffracted waves to the gradient, it is possible to adjust the velocity gradient in the very bottom of the outer core and in the neighbouring region above to model these diffracted waves as we successfully demonstrated above. Further constraints on this velocity structure and possible lateral variations will come from modeling regional broadband seismic data.

It is important to realize that the determination of this velocity gradient has been crucial in the derivation of density stratification and the physics of the Earth's core. From *Bullen* [1963], the Bullen parameter of inhomogeneity is defined by

$$\eta = \frac{dK}{dP} + g^{-1}\frac{d\Phi}{dr} \tag{3.1}$$

where dK/dP is the pressure derivative of bulk modulus and $\Phi = V_p{}^2 - 4/3V_s{}^2$ is the seismic parameter. Both terms are physically measurable and can be determined independently. The value of η equal unity implies uniform chemical composition. With the second term in (1) vanishing, $\eta \approx dK/dP$. With dK/dP slowly varying around 3.5 at the outer core pressure from a recent work by *Anderson and Ahrens* [1994] on an equation of state for liquid iron based on experimental data, the inhomogeneity at the bottom of the outer core is "practically inescapable" as is the case for D'' pointed out by *Bullen* [1963] three decades ago.

Chapter 4

Anisotropy of the Earth's Inner Core

4.1 Abstract

In an effort to confirm inner core anisotropy, we conducted a systematic search for
PKP ray paths with various angles from the Earth's spin axis. In particular, we
studied paths nearly parallel to the spin axis (polar paths) and those nearly parallel
to the equatorial plane (equatorial paths). Data for earthquakes and explosions
were collected from Worldwide Standardized Seismograph Network (WWSSN), Long
Range Seismic Measurements (LRSM), and Global Digital Seismograph Network
(GDSN). Absolute times (DF, BC) and differential times (BC − DF, AB − DF) as
well as waveform data were examined. For all polar paths, differential times of
BC − DF consistently yield residuals of 1.5 to 3.5s larger than equatorial paths.
Absolute DF time residuals exhibit anomalies of the same magnitude (1 to 4s) with
DF being early along polar paths while BC residuals have no obvious correlation
with the differential time anomalies. DF phases appear multi-pathed for polar paths
and are relatively simple for equatorial paths. These results coupled with previous

studies suggest an axisymmetric anisotropy at the top of the inner core.

4.2 Introduction

Aspherical structure of the inner core has been hinted by two kinds of observations: anomalous splitting of the Earth's normal modes [e.g., *Woodhouse et al.*, 1986, *Li et al.*, 1991a] and zonal or directional variations of travel times of waves that go through the inner core, PKIKP (DF), in which polar ray paths travel significantly faster than equatorial paths [*Poupinet et al.*, 1983; Morelli *et al.*, 1986; Gudmundsson *et al.*, 1987; Shearer *et al.*, 1988; Shearer and Toy, 1991; Creager, 1992]. In particular, a recent study by *Creager* [1992] suggests a large amplitude axisymmetric anisotropy of about 3.5% in the inner core. In his study, large positive differential travel time anomalies of $BC - DF$ ranging from 2 to 4s are observed from near polar paths. Most of the paths, however, are from South Sandwich Islands to College, Alaska and all DF waveforms look complicated.

In this study, we conducted a systematic search for PKP paths with various angles from the spin axis. As in previous studies [*Shearer and Toy*, 1991; *Creager*, 1992], we examined $BC - DF$ differential travel times. In principle, $BC - DF$ is ideal in constraining the structure near the inner core boundary. Their ray paths are very close throughout the mantle, but DF turns at the top of the inner core while BC turns at the base of the outer core. We also determined DF absolute travel times for all $BC - DF$ differential times we examined. Although absolute times are subject to bias from source, receiver and mantle structure, they can be used in determining whether the $BC - DF$ anomalies are from the top of inner core or the base of the outer core. To examine structure at greater depths of the inner core, we also examined

AB — DF differential travel times at large distances, where AB is the PKP branch that turns near the mid-outer core.

The results of our search are consistent: all the polar paths show large BC — DF anomalies compared to "normal" (more equatorial) paths, up to 3.5s. A good example is from several nuclear explosions shown in Fig. 4.1. The short period data are from explosions at Nevada (NTS), Amchitka and Novaya Zemlya test sites recorded at WWSSN stations in South Africa (BUL, GRM, PRE, GRM), South America (SOM) and Antarctica (SNA). The DF ray paths for the source-station combinations sample a range of angles from the equatorial plane (Φ=30-80°). Φ is the angle between the DF ray direction at its turning point in the inner core and the equatorial plane. The records are aligned and normalized with respect to BC. Travel time predictions from the Preliminary Reference Earth Model (PREM) [*Dziewonski and Anderson*, 1981] for a surface focus (dashed lines) are shown for reference. It is clear that paths with large Φ from Novaya Zemlya show anomalous large BC — DF anomalies. The BC — DF residuals relative to PREM range from -0.5 to 0.5s for Φ=30-43° to 1.6s for Φ=65° and 3.5s for Φ=81°. These anomalies are more dramatic near the PKP caustic, where all branches of PKP come together and only one big arrival is normally observed, as in the BUL record from NTS (Handley) and the PRE record from Longshot. Early DF arrivals, however, are clearly observed in the SNA record from Novaya Zemlya November 2, 1974 bomb (SNA110274).

The above BC — DF anomalies are clearly seen in the long period records between a polar path and an equatorial path. Furthermore, the absolute DF times of the polar paths show fast anomalies of the same magnitude compared to the equatorial paths. It is thus confirmed that the top of the inner core is strongly anisotropic. The

Figure 4.1: PKP observations from nuclear explosions recorded in WWSSN short period instruments. Φ is the angle of PKP-DF ray direction at its turning point in the inner core with the equatorial plane (complementary to the angle of the ray direction with the Earth's spin axis). Dashed lines are PREM predictions for a surface focus.
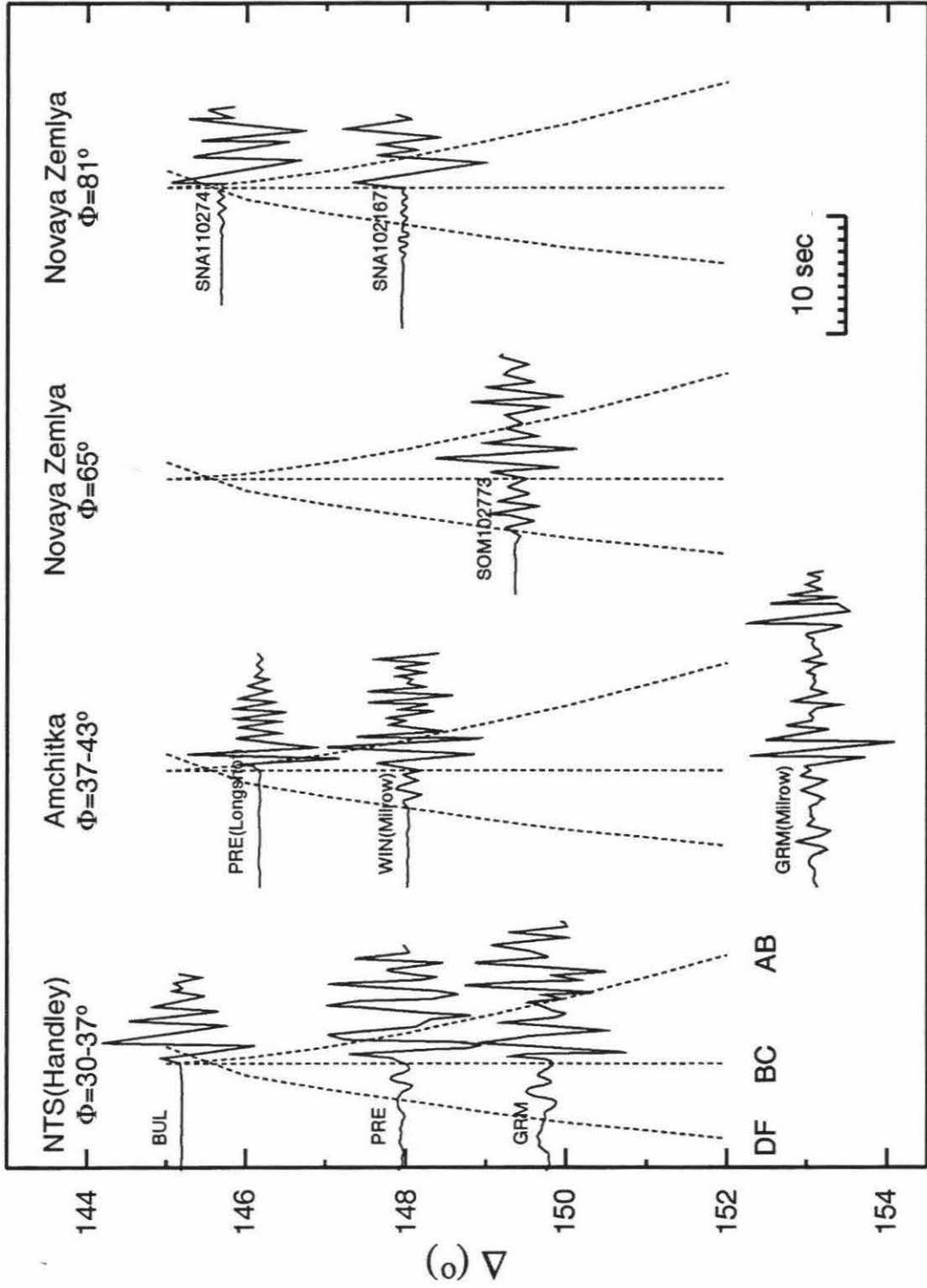
magnitude of the anisotropy seems to decrease at greater depths into the inner core since AB − DF anomalies at larger distances for polar paths are smaller than those of BC − DF even though DF spends more time in the inner core.

4.3 Data and Analyses

In this section, we introduce more comparisons of data from polar and equatorial paths. Fig. 4.2 summarizes the representative ray paths for the BC − DF observations in this study. "Equatorial" paths (small Φ) are dashed; "polar" paths (large Φ) are solid. Since BC can only be observed in a small distance range (from 146 to 158°), the selection of ray paths is limited. Even more limiting is the availability of polar ray paths, which must be from high latitudes in northern hemisphere to high latitudes in southern hemisphere or vice versa. The circles along the ray paths indicate the DF turning points in the inner core. The distance DF travels in the inner core ranges from 55 to 85° for the epicentral distance 147 to 155°. The ray bottoming depth ranges from 150 to 350km below the inner core boundary for this distance range.

The subsequent figures show more examples of PKP observations from different regions with various Φ. In all figures, they are aligned with BC and the amplitudes are normalized with either DF or BC whichever is larger. Travel time predictions from PREM are marked in dashed lines for reference.

Fig. 4.3 shows PKP triplications from quasi-equatorial paths ($\Phi < 45°$). They are all GDSN short period records. The PKP triplications are nicely shown in this figure. The difference of DF arrivals with PREM predictions is within one second. The difference of AB arrivals with PREM is somewhat larger. We should note,

Figure 4.2: Summary ray paths of this study in Hammer-Aitoff equal area projection. Paths nearly parallel to the Earth's spin axis (polar paths) are solid; paths nearly parallel to the equatorial plane (equatorial paths) are dashed. The circles along the ray paths indicate DF turning points in the inner core. The DF phases are observed to travel along the polar paths anomalously faster than along equatorial paths by 1.5 to 3.5s.
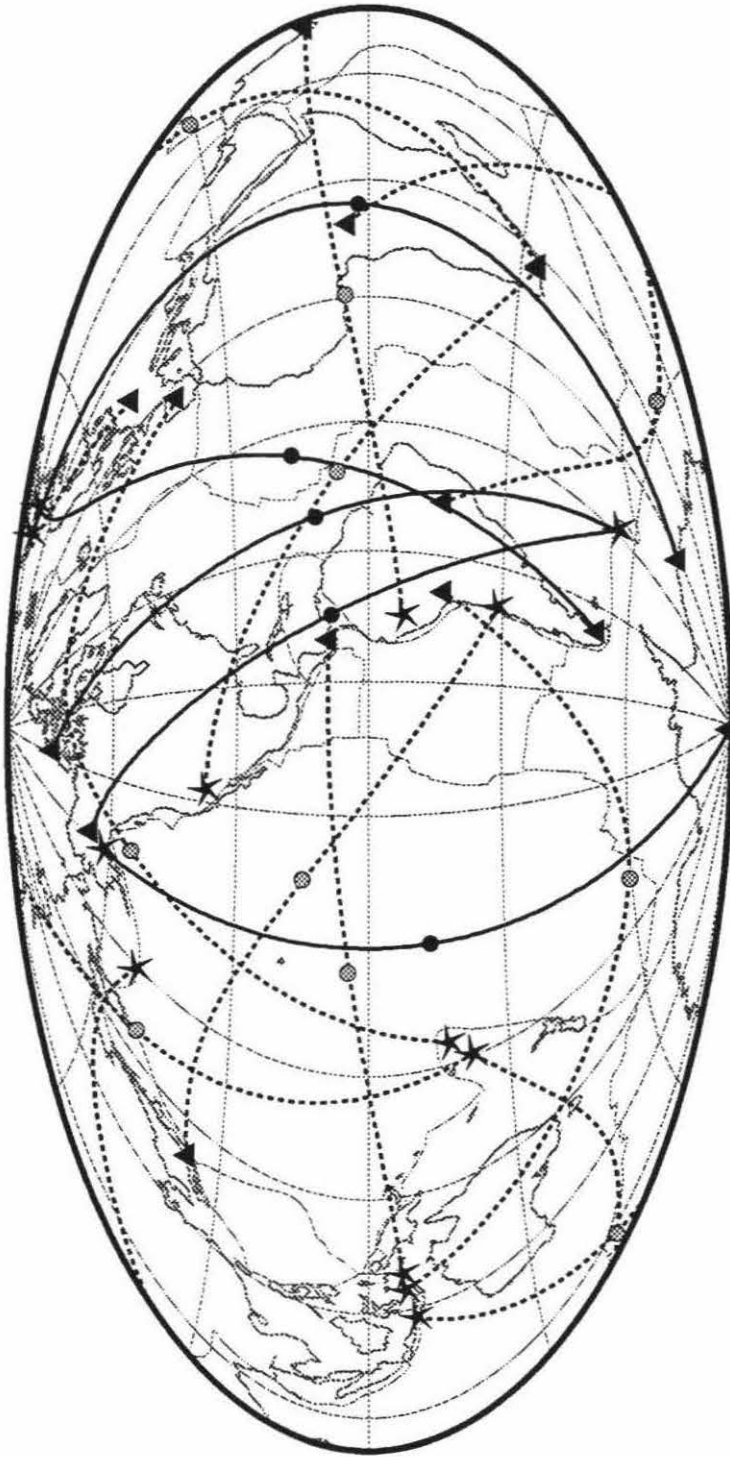
however, that the event depths vary from 33 to 227km and the synthetic predictions are for the depth of 100km only. An increase of focal depth of 100km increases $BC - DF$ and $AB - DF$ differential times by roughly 0.2s and 0.5s, respectively, for the distances concerned.

Fig. 4.4 shows observations for events from South Sandwich Islands to the GDSN station at College, Alaska. The Φ for these paths is around 64°. We can immediately see that DF arrives anomalous early relative to PREM. The $BC - DF$ residuals are about 2.5 to 4s. These anomalies have been used by *Creager* [1992] to infer large-amplitude axisymmetric anisotropy of the inner core. Note that the amplitudes of DF arrivals are anomalously small compared to those of quasi-equatorial paths, as in Fig. 4.3. The move-out of the fast DF with increasing distance, mimicking that of PREM, rules out phase mis-identification. Nevertheless, the large size of the anomalies provides the motivation to search for better polar path coverage and, perhaps, purer polar paths, as reported in this study.

Fig. 4.5 shows data from two extreme paths. Paths from Banda Sea to Balboa Heights, Panama (BHP) are almost along equatorial plane ($\Phi=8°$) while paths from Alaska to the South Pole (SPA) are almost parallel to the spin axis ($\Phi=75°$). The differences of $BC - DF$ residuals for these two paths are about 2 to 3s. Note again, the amplitudes of DF arrivals for the polar paths are small and the waveforms are complicated, appearing multi-pathed. This is true for all the polar paths we examined, including the high-quality data from explosions shown in Fig. 4.1.

Fig. 4.6 shows comparisons of two WWSSN long period records from different paths (solid) and a generalized ray synthetic from PREM (dashed). The top record is from South Sandwich Islands to College, Alaska (COL) ($\Phi=65°$); the bottom record
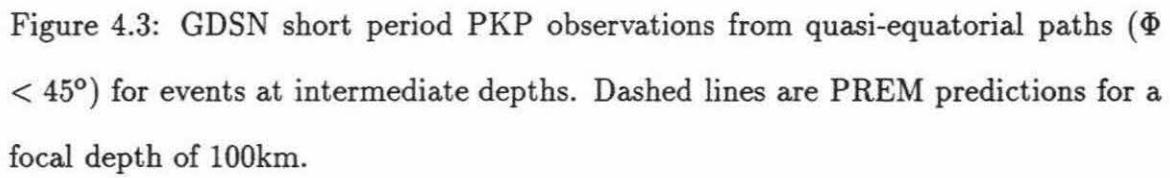
Figure 4.3: GDSN short period PKP observations from quasi-equatorial paths (Φ < 45°) for events at intermediate depths. Dashed lines are PREM predictions for a focal depth of 100km.

Quasi-Equatorial Paths
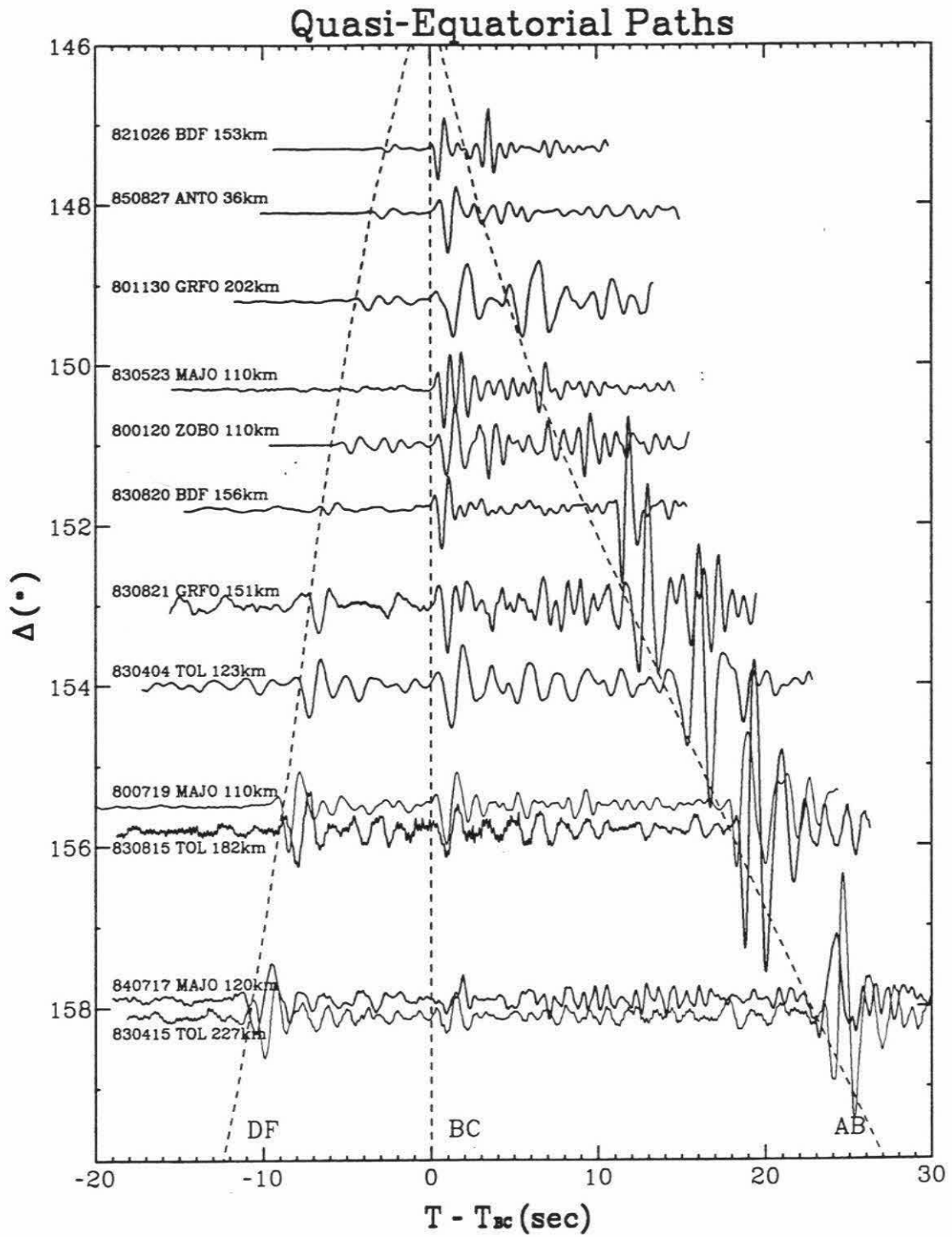
Figure 4.4: GDSN short period PKP observations from South Sandwich Islands to College, Alaska (Φ=64°). Dashed lines are PREM predictions for a focal depth of 100km.

South Sandwich to College, Alaska
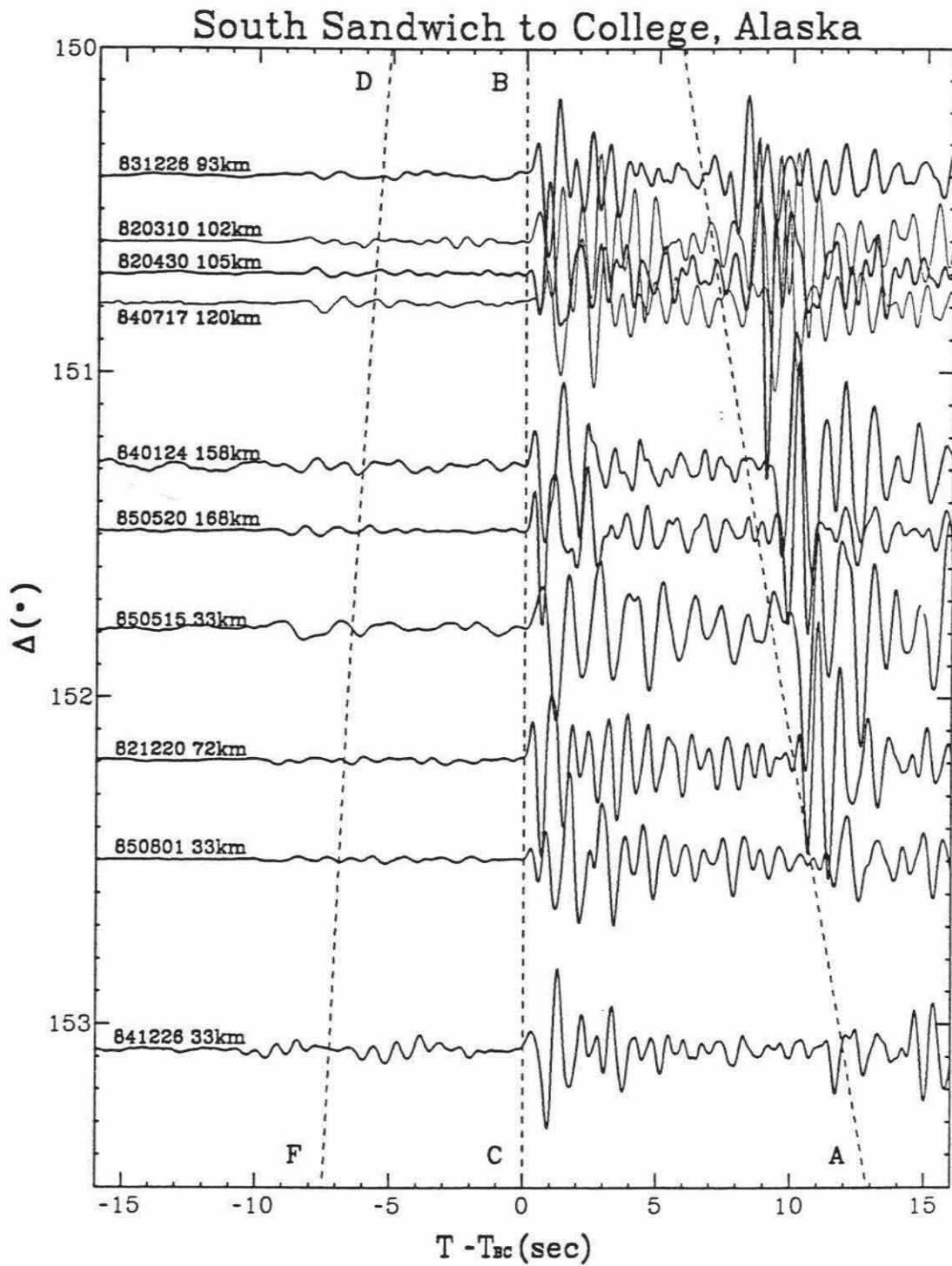
Figure 4.5: Comparisons of WWSSN short period PKP observations between equatorial and polar paths. Dashed lines are PREM predictions for a focal depth of 100km.
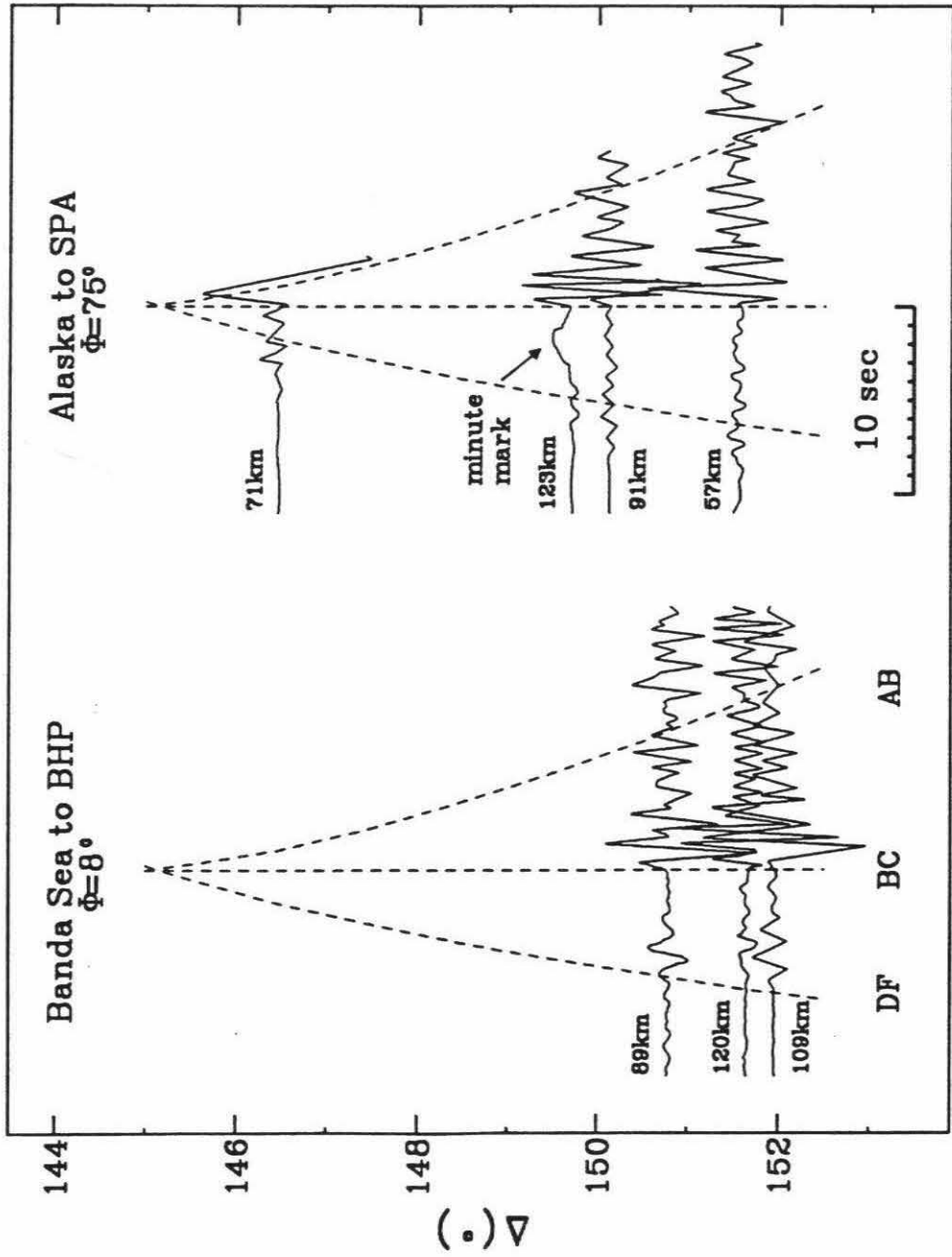
is from an event in northern Peru to Kodaikanal at the southern tip of India (KOD) ($\Phi=9°$). The distances are the same (152.2°). The event depths are 140km and 162km, respectively. The PREM synthetic in the middle is for a depth of 150km. The synthetic matches PKP waveforms of the KOD record and the BC and AB waveforms of the COL record well. The DF pulse of the COL record, however, arrives about 3s earlier than those of PREM and the KOD record. This suggests that the anomaly in the COL record is from DF or the inner core. The DF anomaly is also apparent in the reflected PKP waveforms between the COL and KOD records. Since long period arrivals are very stable in general, we think the observed DF anomalies are robust.

Fig. 4.7a summarizes BC − DF residuals relative to PREM. Fig. 4.7b and Fig. 4.7c show DF and BC absolute time residuals, respectively, for all the picks in Fig. 4.7a after ellipticity corrections [*Dziewonski and Gilbert*,1986]. No station corrections are applied to the absolute time residuals. The error bars show the mean and two standard deviations of the data binned in 10° intervals.

In Fig. 4.7a, the residuals relative to PREM remains from 0 to 1s for $\Phi < 50°$. For $\Phi > 60°$, however, the residuals increase drastically, ranging from 2 to 4s, with increased scatter. The standard deviations are twice those for $\Phi < 50°$. This might be associated with some complex mechanism for the polar paths considering the anomalously small amplitudes and complicated waveforms of DF arrivals. Note that almost all residuals are positive. The base line at small Φ can be adjusted by reducing the velocity gradient at the base of outer core. [*Souriau and Poupinet*, 1991; *Song and Helmberger*, 1994a].

In Fig. 4.7b, the average residuals of DF for large Φ are 1 to 4s smaller than those

Figure 4.6: Comparisons of WWSSN long period PKP observations between a polar path (top) and an equatorial path (bottom). Dashed line in the middle is PREM synthetic for a focal depth of 150km.
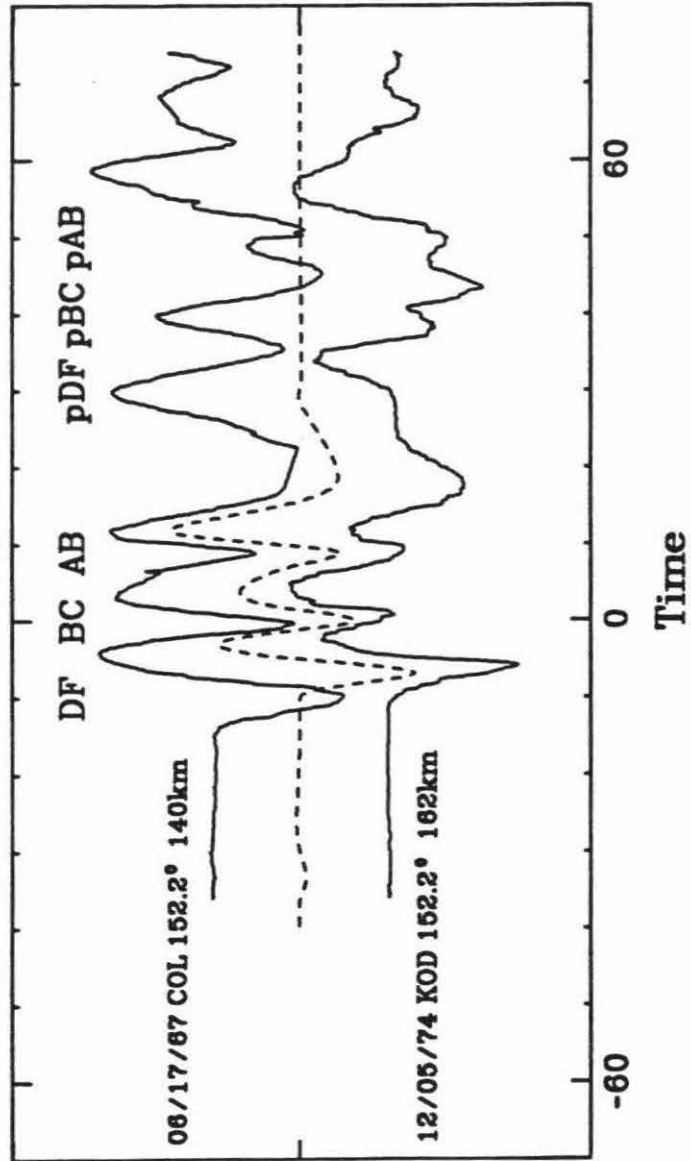
Figure 4.7: Travel time residuals relative to PREM vs. Φ for a) $BC - DF$; b) DF; c) BC. The error bars show the mean and two standard deviations of the data after binned in $10°$ intervals.

a) BC-DF

+ bomb(WWSSN)
△ quake(WWSSN/LRSM)
o quake(GDSN)

b) DF

c) BC

travel time residual (sec)

angle from equatorial plane (deg)
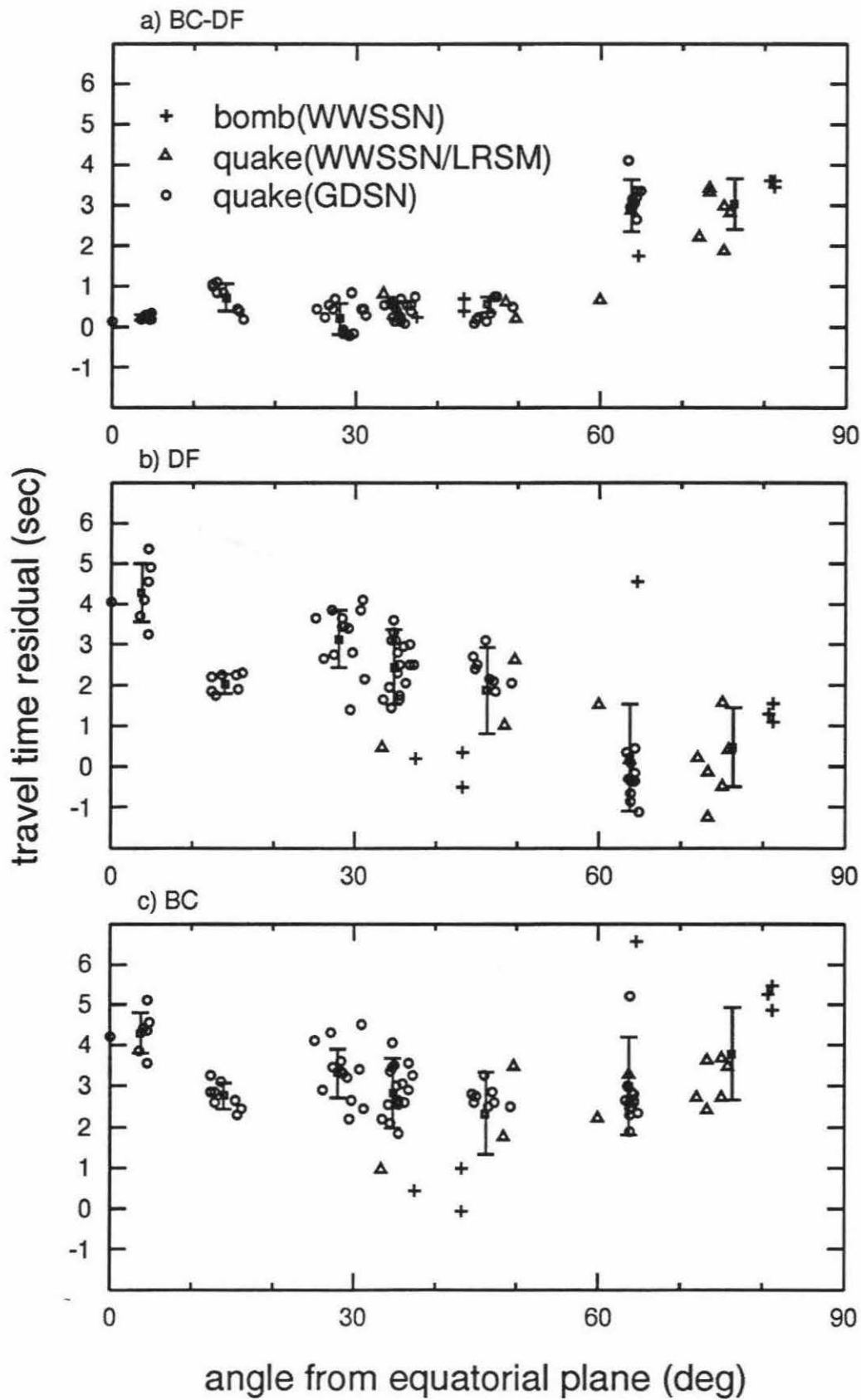
for smaller Φ. The difference is about the same magnitude as that of BC − DF, suggesting that the observed BC − DF anomalies from the polar paths are from DF or the inner core, at least to the first order. This is also clear if we examine BC residuals in Fig. 4.7c. Residuals from polar paths with $\Phi > 60°$ are quite similar to those from quatorial paths with $\Phi < 30°$. In fact, the BC residuals show, interestingly, symmetric Φ dependence around $45°$. The explosion data points near $40°$ are exceptions. They are from the Amchitka test site which has 1.5 to 2.0s travel time residuals caused by the fast slab as reported by *Davies and Julian* [1972] and others. Note there are large positive DF and BC residuals in Fig. 4.7b and Fig. 4.7c, most of which can be accounted for by baseline shifts inherent in PREM.

In Fig. 4.7a, BC − DF differential travel time residuals for all epicentral distances are plotted in the same figure. To examine directional velocity variations, the travel time residuals are re-plotted as percentages of the DF travel times through the inner core as in Fig. 4.8. If we assume uniform axi-symmetric anisotropy of the inner core about the Earth's spin axis, these relative residuals are equivalent to the velocity perturbations. For weak anisotropy, the compressional velocity perturbations can be approximated by $-\delta v/v = \delta t/t = a + b\cos(2\Phi) + c\cos(4\Phi)$ [*Morelli et al.*, 1986; *Shearer and Toy*, 1988; *Creager*, 1992]. The solid line shows the least-square fit of the expression to the data with a=0.0123, b=-0.0151, c=0.0068. The result indicates that velocity in polar direction is 3% faster than the equatorial direction.

4.4 Discussion and Conclusion

The main result of this study is that BC − DF for all the polar paths we examined show large anomalies of 1.5 to 3.5s relative to equatorial paths. Absolute DF residuals
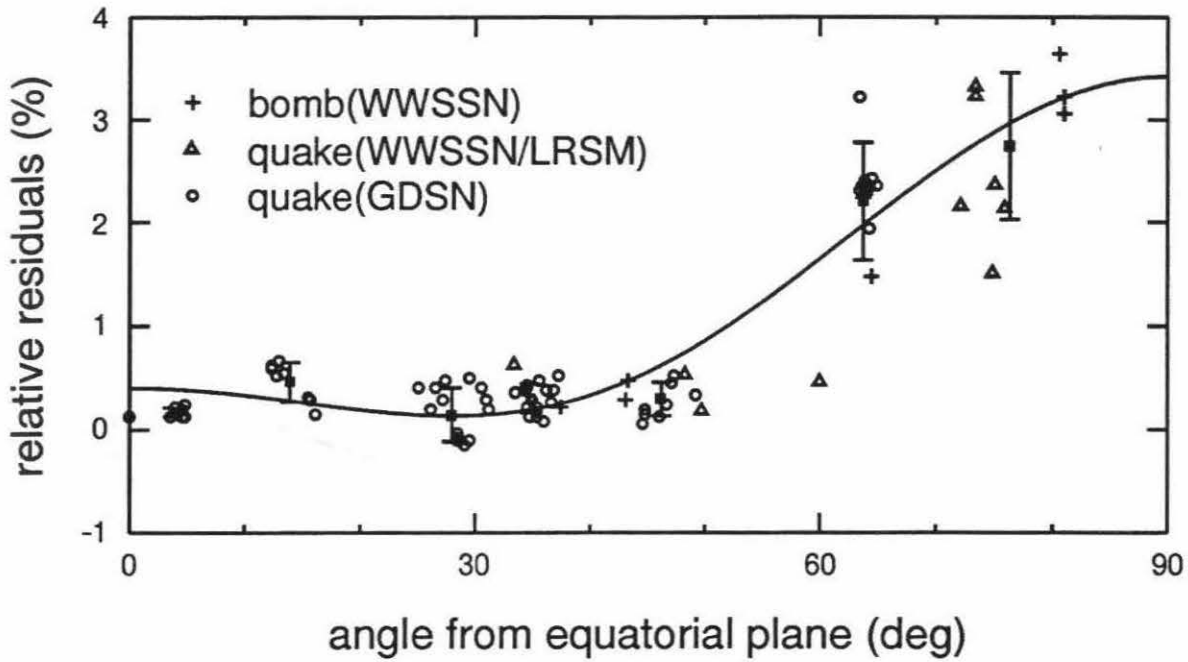
Figure 4.8: BC-DF differential travel time residuals divided by DF times through the inner core (in percent) vs Φ. The error bars show the mean and two standard deviations of the data after binned in 10° intervals. Solid line is the least-square fit of an axi-symmetric anisotropic model to the data.

correlate with these values but BC residuals do not, suggesting that the top of the inner core is very anomalous. Inner core anisotropy, with the fast direction parallel to the spin axis, is the most plausible conclusion at present. For a simple axi-symmetric anisotropic model, the polar direction is 3% faster than the equatorial direction.

A recent study by *Roudil and Souriau* [1993] suggests weak anomalies (less than 0.5s) in BC travel times from ISC. The residual variations with respect to angles from the spin axis are about 0.3s with polar paths slightly slower. This also indicates that the large BC − DF anomalies cannot be from the bottom of the outer core.

Poupinet et al. [1983] suggests there may be fast polar caps and a slow equatorial belt to explain the latitudinal dependence of PKIKP-P residuals with polar stations being fast. This model does not seem to be compatible with our observations. In Fig. 4.2, we have quasi-equatorial paths sampling the inner core at both low latitudes (e.g., South America to Japan and NTS to South Africa) and high latitudes (e.g., Fiji to Europe, Java to South America and South Africa). No obvious trend of latitudinal dependence (in terms of turning point latitude) is observed. Similarly, in Fig. 4.1, ray paths from NTS and Novaya Zemlya all sample low latitudes at turning points, ranging from 0 to 25°, but with totally different azimuths.

The above discussion also argues in favor of anisotropy of the inner core rather than lateral variations. A better indication comes from comparisons of polar and equatorial paths sampling the same region. One example is shown in Fig. 4.5 where paths from Alaska to the South Pole (SPA) and paths from Banda Sea to Balboa Heights, Panama (BHP) almost cross each other perpendicularly in the inner core underneath the central Pacific. Another example is shown in Fig. 4.1 where the path from Novaya Zemlya to Sombrero, Chile (SOM) samples the same region underneath

the east central Atlantic as the path from NTS to Grahamstown, South Africa (GRM) with a different azimuth.

These results are limited to a small shallow depth range of the inner core (120 to 300km from DF sampling at distances 145 to 153°). To constrain depth variations of the anisotropic structure, we need to look at DF at greater and smaller distances for polar paths. A good set of data comes from Novaya Zemlya explosions to Scott Base, Antarctica and the South Pole. The distances range from 160 to 164° which sample depths of 500-600km into the inner core. The AB − DF residuals show 1.5 to 2.5s positive anomalies compared to the average AB − DF residuals for more equatorial paths in our previous study [*Song and Helmberger*, 1993a]. Thus the anisotropic structure does not seem uniform. Since AB − DF is more subject to bias from the lower mantle variations [*Song and Helmberger*, 1993a], exhibiting larger scatter (up to 2s) in general, better path coverage is needed to confirm this result. For the topmost inner core, waveform modeling of PKIKP and the inner core reflected phase, PKiKP, in the distances 128 to 138° has been very successful [*Cummins and Johnson*, 1988; *Song and Helmberger*, 1992]. A 3% anomaly for polar paths will give about 1s shift, which can be readily resolved from short period waveforms, although we must be careful about PKP precursors at these distances.

In summary, the evidence for a directional dependence of travel times through the inner core is now well established. Considerable effort will be required to resolve the physical details of the model causing this apparent anisotropy, that is, preferentially oriented crystals or laminated solid that behaves as anisotropy [*Anderson*, 1989]. The model will be addressed in future efforts.

Chapter 5

Depth Dependence of the Inner Core Anisotropy

5.1 Abstract

Recent findings show general agreement on the anisotropy of the inner core from both body wave travel times [*Creager*, 1992; *Song and Helmberger*, 1993b; *McSweeney and Creager*, 1993; *Shearer*, 1994] and fits to the splitting of core modes[*Tromp*, 1993] that the top 300km of inner core is very anisotropic. The anisotropy displays axial symmetry around the Earth's spin axis with the polar direction 3% faster than the equatorial direction. One key problem now is the depth dependence of the inner core anisotropy.

Here we extend our polar path studies to include both long-period and short-period modeling at ranges 120° to 173°. At ranges 130° to 146°, arrivals from the top of the inner core (PKIKP) and reflections from the inner core boundary (ICB) can be observed distinctly in short-period records. On the long-period records, we

119

rely on waveform distortions of these arrivals and energy from the outer core. Record sections of polar paths from three events, two beneath the South Sandwich Islands and along the Macquarie Ridge, recorded at WWSSN, CAND and LRSM stations are analyzed. Our results suggest that the top 150km of the inner core is only weakly anisotropic (less than 1%) and the top 60km appears to be isotropic.

5.2 Introduction

Recent findings show general agreement on the anisotropy of the inner core. Both body wave travel times [*Creager*, 1992; *Song and Helmberger*, 1993b; *McSweeney and Creager*, 1993; *Shearer*, 1994] and fits to the splitting of core modes by *Tromp* [1993] display an axi-symmetric anisotropy of around 3% with fast direction parallel to the spin axis at the depth range of 150km and 300km into the inner core. Tromp's model displays a monotonic decrease of the anisotropy in P-wave velocity from the top of the inner core to the center of the Earth. A complete spherically symmetric model of the similar kind has yet to be constructed from the body waves.

While the travel times along polar paths appear to be quite anomalous compared to equatorial paths. The sampling from the polar samples is rather sparse as reported by *Shearer* [1994]. Most ISC polar samples are associated with paths originating at South Sandwich Islands. These events occur below 33km and are probably the best documented in terms of travel time anomalies by *Creager* [1992], *Song and Helmberger* [1993b] and most recently by *Vinnik et al.*[1994]. The recent studies by *Song and Helmberger* [1993b] and *Vinnik et al.*[1994] suggest that these anomalies persist at periods longer than one second and can be seen in broadband waveforms. These results are very significant in that such waveform data can be used to more

fully understand the nature of the anisotropy as well as model shallow events where short-period picks of travel times alone become difficult to interpret. For example, as pointed out by *Shearer* [1994], the ISC times from events occurring along the Macquarie ridge do not appear as anomalous as the South Sandwich events. That is, the ISC times from events occurring along the Macquarie ridge do not support the anisotropy model. But since most of these events are strike-slip (occurring at transform faults) and most are rather small, we expect direct P to be weak compared to sP; thus it becomes difficult to pick out the PKP triplication phases. This feature is further complicated by the precursors that occur in the range 130° to 144°.

In this report, we examine a few long-period and short-period record sections from events occurring beneath South Sandwich Islands and Macquarie ridge to help establish the nature of the anisotropy both in depth distribution and spatial character. We concentrate on the topmost 150km of the inner core. This depth range is not well sampled by the above reported body wave travel times. It might not be well resolved in Tromp's fits either because the long-period nature of the normal modes and spline functions used, which tend to smooth out the structure involved. It appears that the detailed resolution of the anisotropy at the topmost of the inner core comes from the waveform modeling of PKP body-waves before the caustic (from 130° to 146°). At this distance range, arrivals from the top of the inner core and reflections from the inner core boundary (ICB) can be observed distinctly in short-period records and have been used successfully to investigate velocity structure near the ICB in previous studies [*Cummins and Johnson*, 1988; *Song and Helmberger*, 1992]. On the long-period records, we rely on waveform distortions of these arrivals and energy from the outer core.

Figure 5.1 show the ray paths of PKIKP (DF) and PKiKP mentioned above and other branches of PKP phases. Table 5.1 summarizes some useful parameters of DF ray paths in the inner core. It is calculated for a surface focus using the Preliminary Reference Earth Model (PREM) [*Dziewonski and Anderson*, 1981]. Ranging from 120° to 180°, the rays sample the top of the inner core to the center of the Earth. The sampling depths vary only slightly (within 20 km) for two extremal focal depths at 0km and 700km. The time residual of DF for 3% axi-symmetric anisotropy exceeds half a second at distance of 136° for a ray angle from the equatorial plane $\Phi=63°$, which can be readily resolved in short-period DF and PKiKP waveforms. If 3% anisotropy occurs throughout the inner core, the time residuals of DF range from a few tenth of a second to 6.5 seconds for the whole distance range for paths running North-South. Included on the right of the table are differential times of PKP branches predicted from PREM along with those from a modified model, PREM2 [*Song and Helmberger*, 1994a]. We will discuss these comparisons in more detail later.

5.3 Waveform Modeling Results

We examined three events in this study, two occurring beneath the South Sandwich Islands and one along the Macquarie Ridge listed in Table 5.2. Event 3 was one of the events used by *Häge* [1983] to study the inner core from PKP amplitudes. Stations include Worldwide Standardized Seismographs Network (WWSSN), Canadian Network (CAND) and Long Range Seismic Measurements (LRSM). The analog seismograms were scanned and digitized. The digitization is accurate to a fraction of a second.
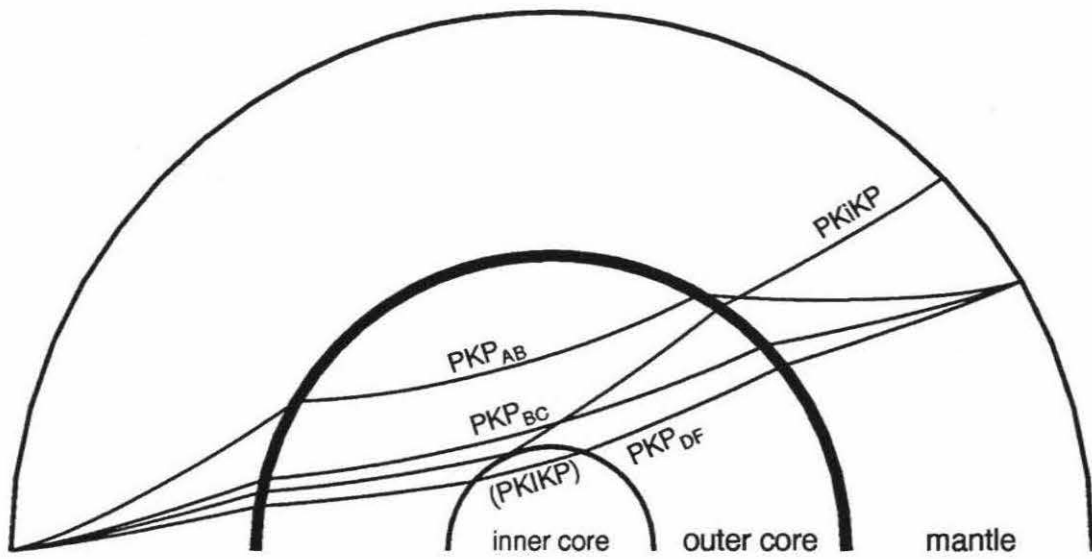
Figure 5.1: Ray paths of PKP phases used in this study.

Δ (deg)	Δ_{ic} (deg)	T_{ic} (sec)	Z_{bot} (km)	Differential Times (sec)			
				PREM		PREM2	
				CD-DF		CD-DF	
120	4.0	7.8	0.8	0.05		0.10	
122	6.3	12.2	1.9	0.12		0.20	
124	8.7	16.8	3.7	0.21		0.32	
126	11.3	21.8	6.2	0.34		0.47	
128	14.0	27.1	9.5	0.49		0.66	
130	17.0	32.8	14.0	0.68		0.88	
132	20.3	39.0	19.9	0.90		1.13	
134	23.8	45.7	27.3	1.15		1.42	
136	27.7	53.0	37.0	1.45		1.76	
138	32.0	61.0	49.2	1.80		2.15	
140	36.8	69.8	64.8	2.20		2.59	
142	42.0	79.3	84.4				
144	47.8	89.6	108.7	BC-DF	AB-DF	BC-DF	AB-DF
146	54.1	100.5	138.4	0.99	1.44	1.03	1.72
148	60.8	111.8	173.9	3.27	5.81	3.31	6.22
150	68.0	123.3	215.3	5.07	10.61	5.13	11.11
152	75.4	134.8	262.7	6.50	15.75	6.72	16.36
154	83.1	146.0	315.5		21.19	8.23	21.91
156	90.8	156.6	372.7		26.92		27.75
158	98.6	166.5	434.1		32.93		33.87
160	106.3	175.6	498.5		39.21		40.26
162	114.0	183.9	565.6		45.74		46.91
164	121.6	191.3	634.6		52.54		53.83
166	129.1	197.7	705.2		59.59		61.00
168	136.5	203.3	777.2		66.90		68.43
170	143.9	208.0	850.0		74.45		76.11
172	151.2	211.8	923.6		82.24		84.03
174	158.4	214.7	997.6		90.28		92.20
176	165.7	216.8	1072.0		98.55		100.60
178	172.8	218.0	1146.7		107.06		109.25
180	180.0	218.4	1221.5		115.80		118.12

Table 5.1: Some useful parameters related to PKP-DF for a surface focus. Δ is the epicentral distance; Δ_{ic} is the distance DF travels in the inner core; T_{ic} is the time DF spends in the inner core and Z_{bot} in the bottoming depth of DF ray paths in the inner core. These parameters are calculated for a surface focus using PREM model. The right side of the table compares the differential travel times of PKP phases from PREM2 model and those from PREM.

Event	Region	Date	Origin Time	Epicenter	Depth	m_b
1	South Sandwich	17 Jun 1967	05:00:12.0	58.36°S/26.83°W	136	5.9
2	South Sandwich	13 Dec 1965	15:08:27.2	56.14°S/27.76°W	153	5.2
3	Macquarie Ridg	21 Jul 1977	11:53:22.3	53.8°S/158.80°E	33	6.2

Table 5.2: Two events used in this study.

5.3.1   South Sandwich Islands Events

We selected two of the simplest events available from this region. The smaller of the two is particularly well recorded by the LRSM network. The paths associated for Event 1 are displayed in Figure 5.2. There are two distinct ray path groups from this event. One group contains polar paths to Canada and Alaska (Φ ranging from 61° to 72°); the other one contains non-polar paths to Japan and South Korea (Φ around 48°). The paths associated for Event 2 are similar to the group to North America.

Figure 5.3 shows comparisons of two stations at close distances from a polar path and a non-polar path from Event 1. It is yet another nice example of inner core anisotropy. DF for polar path to COL (Φ= 65°) at a smaller distance arrives clearly earlier than the non-polar path to SHK (Φ= 47°). This is true on both long-period and short-period records. In the long-period channel, the DF pulse of COL appears to be broadened. The anomalously early DF arrivals such as this have been interpreted by axi-symmetric inner core anisotropy of 3.5% based on samples from South Sandwich Islands to College, Alaska [*Creager*, 1992] or an average of 3% based on other more polar paths as well [*Song and Helmberger*, 1993b]. These results appear to be compatible with the results from the recent revisit of ISC data [*Shearer*, 1994]. The question now is whether the anisotropy of this magnitude exists at the top few tens of kilometers of the inner core. To answer the question, we need to test the sensitivity of synthetic waveforms to various velocity distributions and examine how these synthetics compare with observations.

Figure 5.4 shows comparisons of observations (solid) for non-polar paths (Φ around 48°) and synthetics (dashed) from a recent average Earth's core model PREM2 [*Song and Helmberger*, 1994a]. The model is modified from PREM to fit

Figure 5.2: Ray paths of Event 1 from the South Sandwich Islands. Paths of Event 2 to North America stations are similar to those of Event 1.
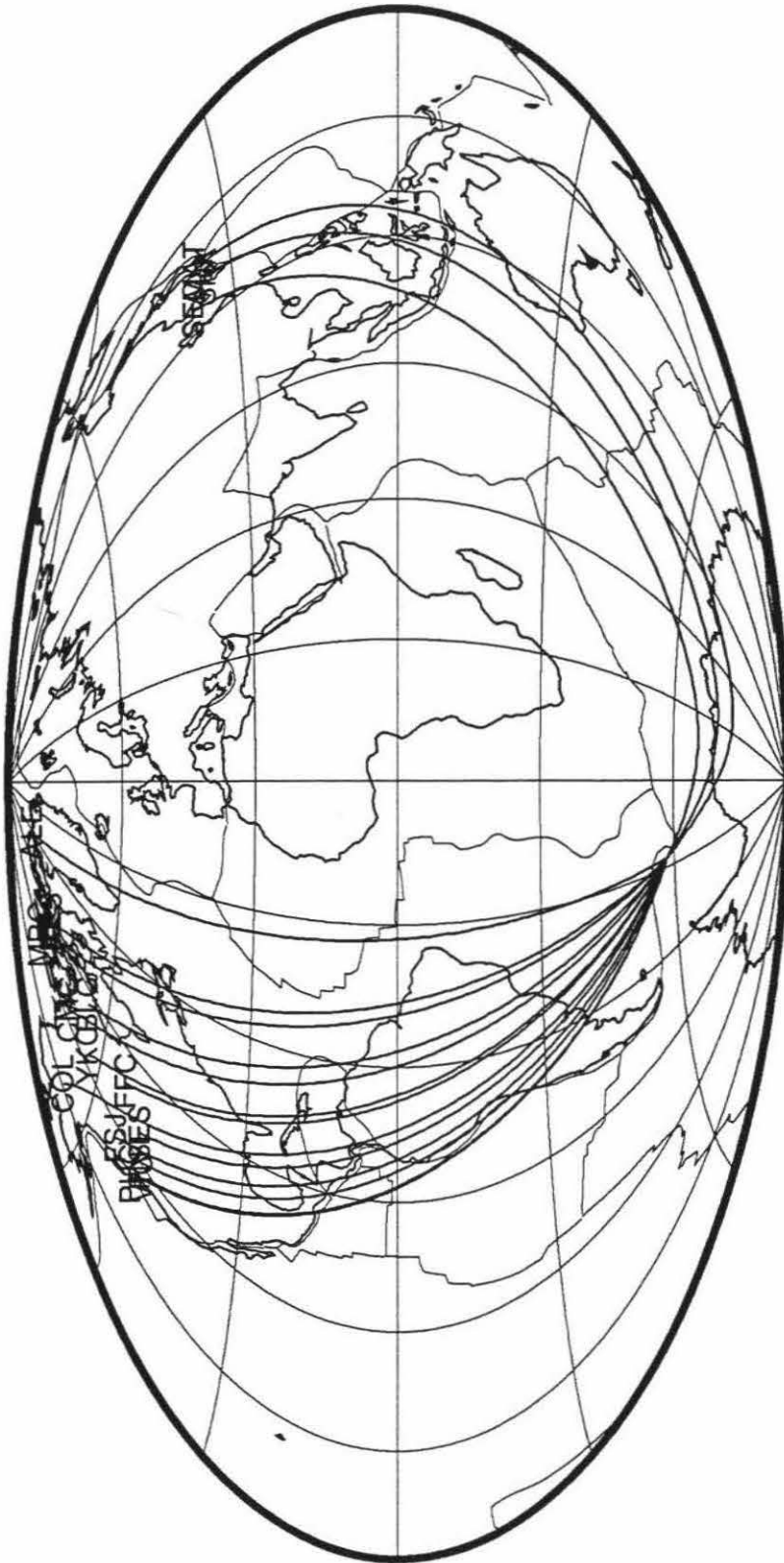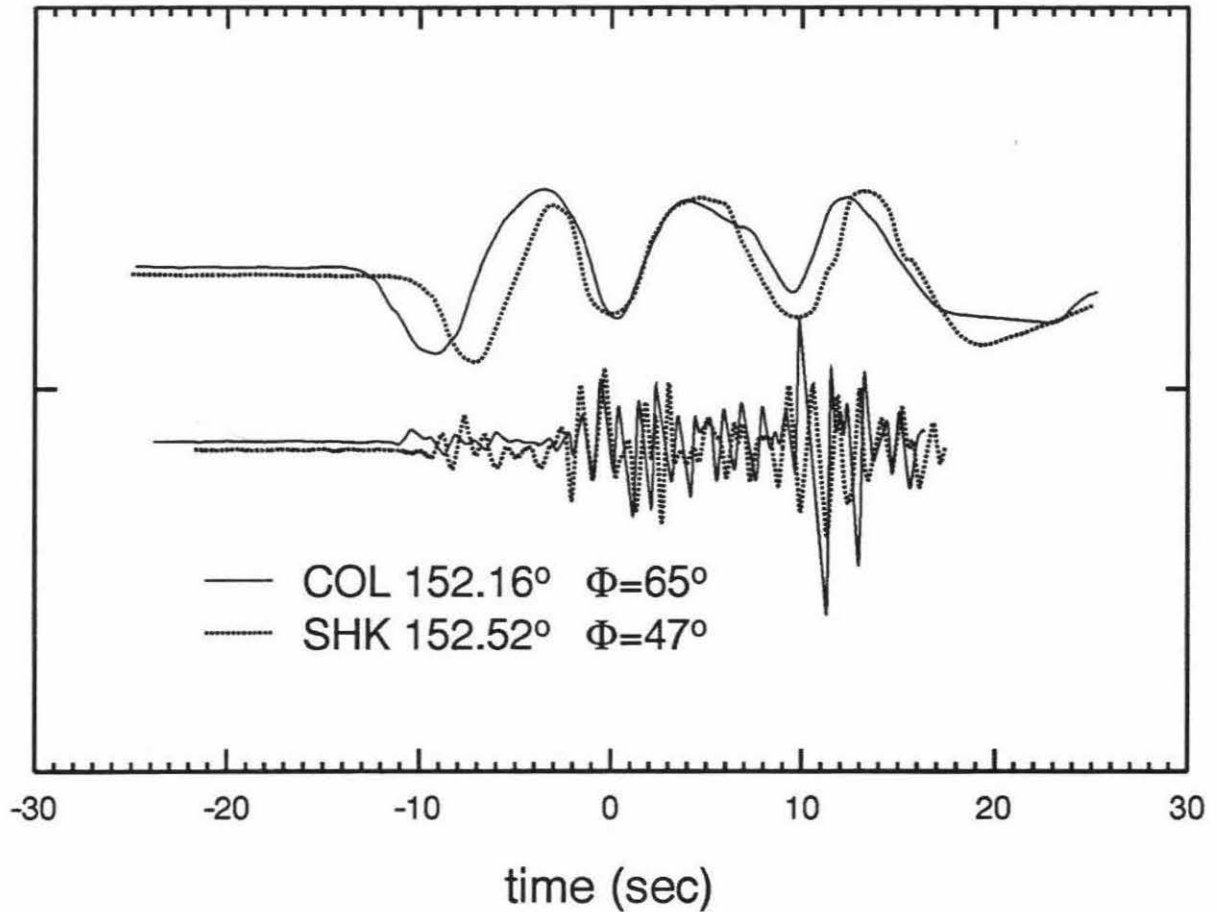
Figure 5.3: Comparisons of a polar path and a non-polar path at close distances from Event 1. Φ is the angle of the DF ray direction in the inner core from the equatorial plane, which is complimentary to the angle from the rotation axis.

differential travel time, amplitude ratios and waveforms of PKP phases on a global scale but from nonpolar paths, see Table 5.1 for comparisons of differential travel time predictions. The synthetics fit these observations reasonably well.

The depth dependence of the inner core anisotropy is explored by modeling PKP waveforms across the PKP triplications shown in Figure 5.5. Solid lines are the observations for polar paths (Φ ranging from 61° to 72°). Dotted lines are predictions from three test models. Data are shifted to line up with the synthetics. The left column shows that our average core model PREM2, which fits the non-polar paths, does not fit the data at the COL record and records at distances approaching the PKP caustic (RES, CMC, ALE). The DF arrivals from the inner core appear too late. The middle column shows synthetics from PREM2 model with a 3% uniform increase of inner core P velocity throughout the inner core. The mis-fits before the caustic (RES, CMC, ALE) and at the caustic (MBC) are obvious. The model speeds up the DF arrival so much that it becomes a very distinct arrival at CMC. Our current best fits are shown in the column on the right from a test model, PREM2_NS. This model a 1% velocity increase at the top 200km of the inner core and a 3% increase down below. The fits between 140° and 146° are significantly improved. The fits in distances smaller than 140° are less discernible between models at these periods. More definite results rely on modeling of short-period records at these ranges as discussed later. Although the details of the model may vary, this seismic section does indicate the anisotropy at the very top of the inner core, perhaps top 150km, is weaker than that at greater depths, which we have seen in the BC − DF differential times.

The short-period modeling results for event 2 are displayed in Figure 5.6. The
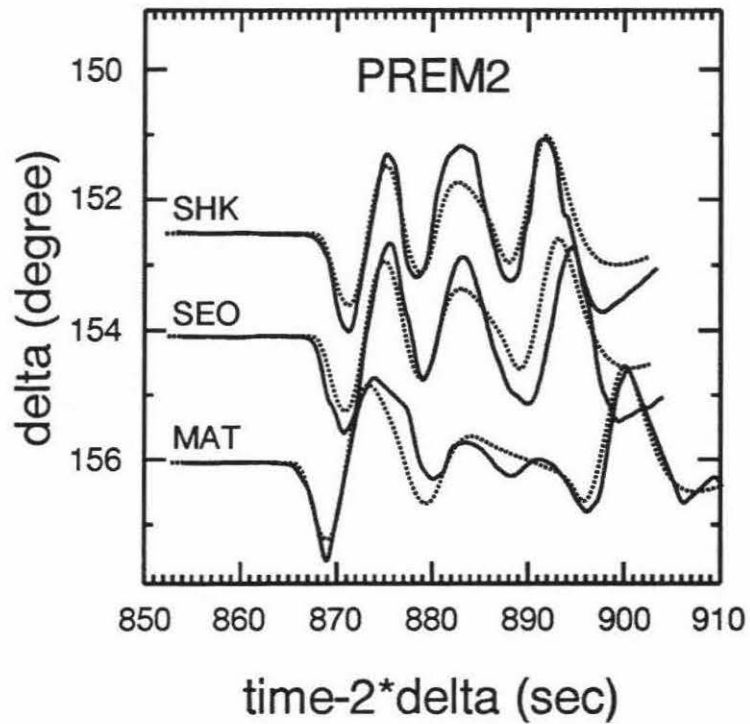
Figure 5.4: Synthetics (dotted) from PREM2 [*Song and Helmberger*, 1994a] fit non-polar paths (Φ around 48°) from Event 1 rather well.

132

Figure 5.5: Comparisons of the observations (solid) for polar paths (Φ ranging from 61° to 72°) from Event 1 and synthetics (dotted) from three testing models.
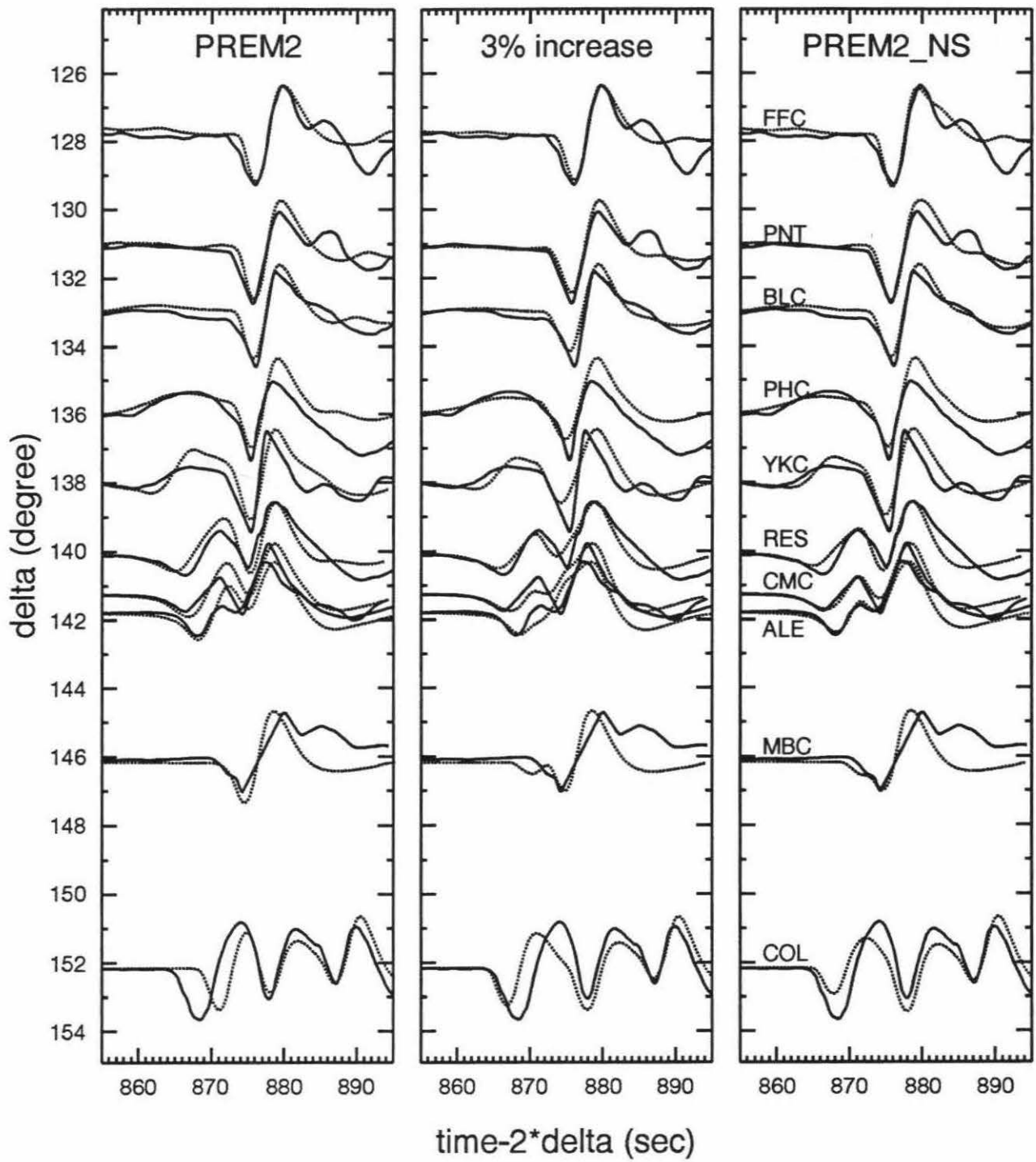
data include short-period vertical components from both WWSSN and LRSM stations in North America. The station names (three letters for WWSSN, four letters for LRSM) and the Φ angles are marked by the traces. The synthetics are calculated using PREM. Dashed lines are the geometric travel time predictions of of PKP phases from PREM. The empirical source functions for the synthetics are shown in Figure 5.7. The effective source function for LRSM records was obtained from the stack of the PKiKP arrivals from 3 stations: WNSD, KNUT and RGSD. The source function for WWSSN stations are taken directly from the direct P arrival at LPS at 86.8°, which has a similar azimuth to those of the stations used. We favor this description of the source excitation as compared with attempting to model the earthquake explicitly [*Song and Helmberger*, 1992]. A differential t^*=0.2s was applied to the PKIKP (DF) to account for inner core attenuation. This value is significantly smaller than our earlier result of 0.4s [*Song and Helmberger*, 1992] or 0.35s [*Song and Helmberger*, 1994a], which is not well understood at the present.

In the lower panel of Figure 5.6, the observations from College, Alaska (COL) is aligned and normalized with respect to BC arrivals in the synthetics. The DF arrival from COL is 2.9s earlier than PREM predictions due to inner core anisotropy at greater depths, which corresponds to an anisotropy larger than the average 3% for this particular example. On the other hand, the AB arrival from COL is 1s later than PREM predictions. This discrepancy can be explained by slowing down the P-wave velocity in the lowermost mantle. This is demonstrated by the long-period fit of the COL record in Figure 5.5 from PREM2, which slows down PREM in the lowermost mantle.

In the upper panel, however, the PREM synthetics fit the observations rather
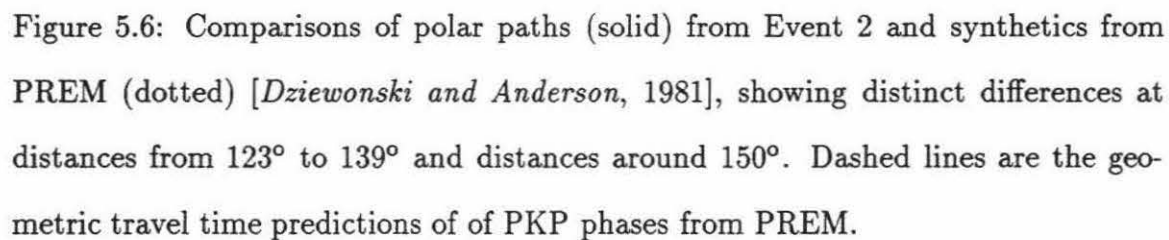
Figure 5.6: Comparisons of polar paths (solid) from Event 2 and synthetics from PREM (dotted) [*Dziewonski and Anderson*, 1981], showing distinct differences at distances from 123° to 139° and distances around 150°. Dashed lines are the geometric travel time predictions of of PKP phases from PREM.

Dec 13,1965 South Sandwich (h=153km)

delta (deg)

travel time - 2*delta (sec)
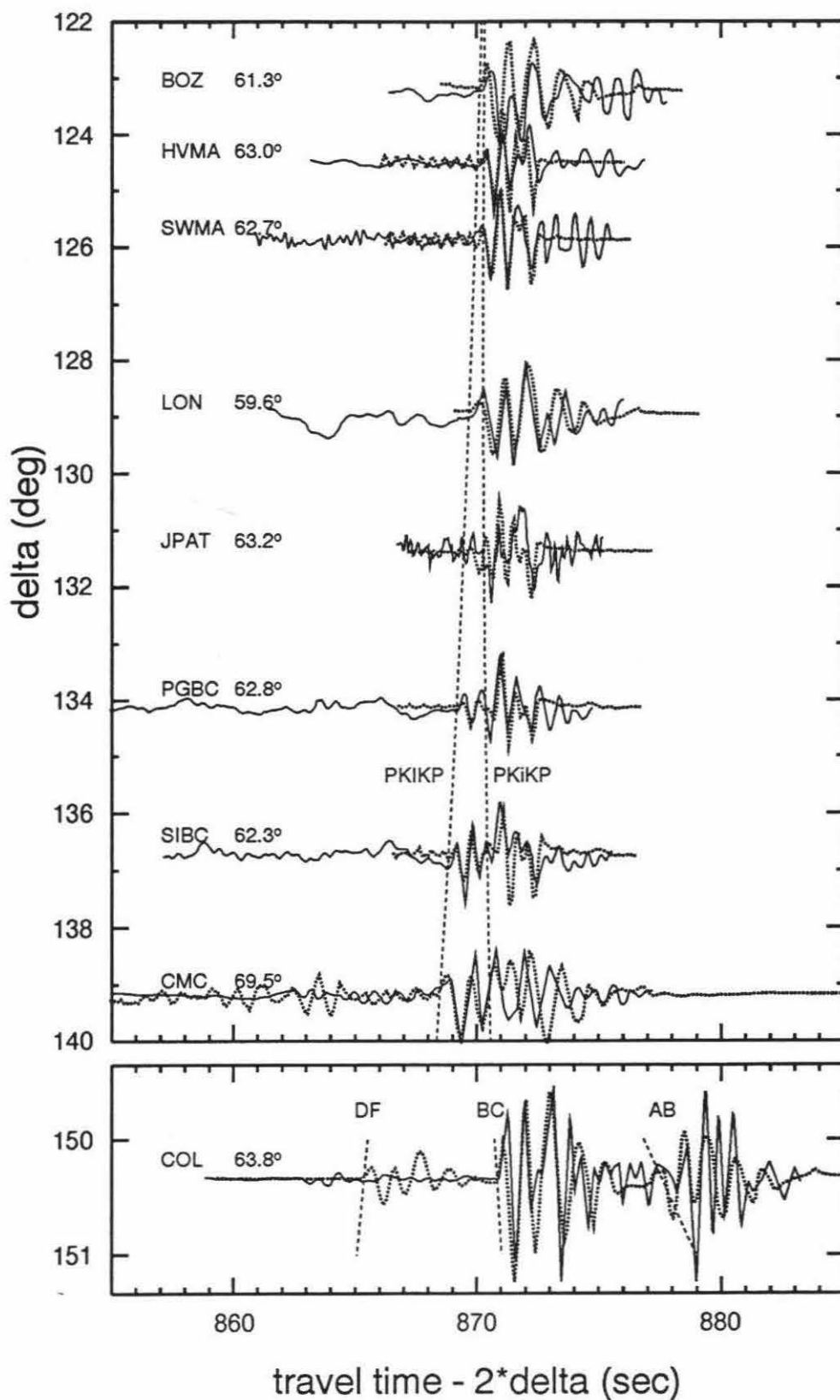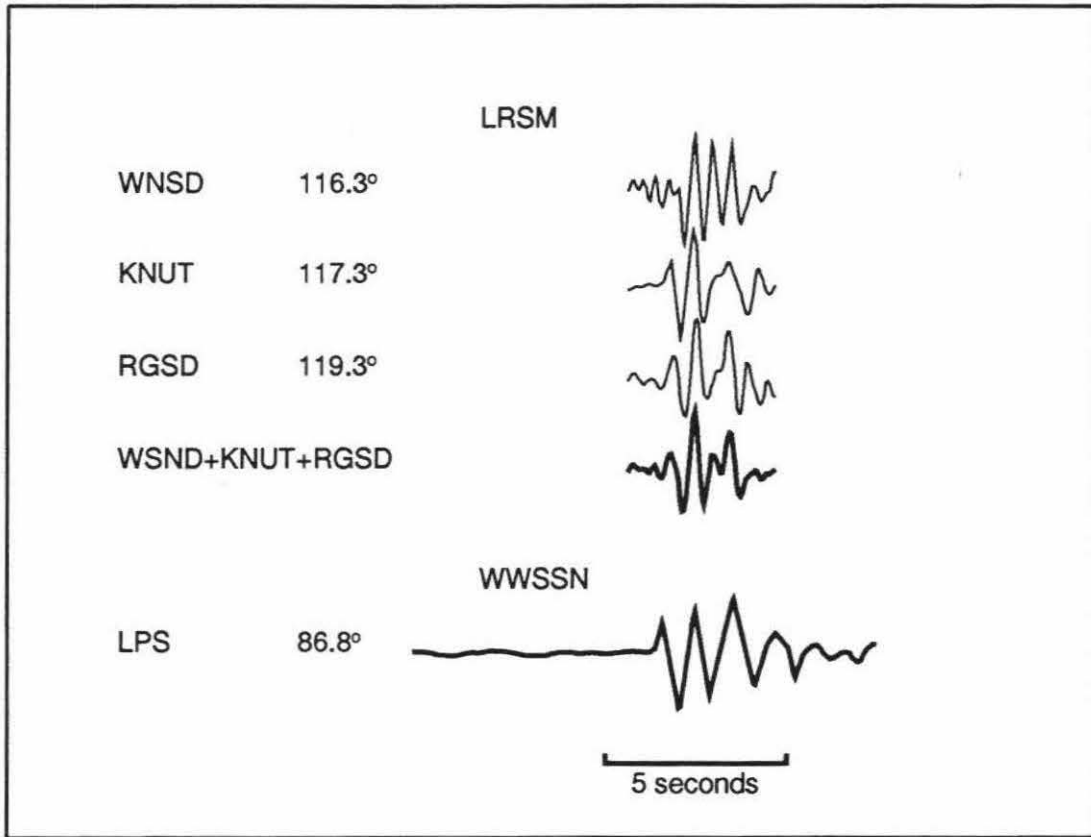
Figure 5.7: The effective source functions used for synthetics of Event 2.

well, indicating the top 60km of the inner core sampled by these polar paths is not anomalous at all. The fits on the PKIKP and PKiKP waveforms from PREM for these records are actually better than PREM2, which would predict 0.1-0.3s larger separations between these two arrivals [see Table 5.1]. Note no clear precursors to PKIKP are observed in these records. At CMC, however, we start to see diffraction from the B caustic in both the data and the synthetic. To summarize, the distinct differences at these two distance ranges from very similar paths argue strongly lack of or very weak anisotropy at the top 60km of the inner core.

5.3.2 Macquarie Ridge Event

Unfortunately, the South Sandwich Islands is the only place in the southern hemisphere where polar paths from deep events can be obtained. Most of the other paths involve shallow ridge events which generally produce weak P-waves. Thus, the scatter in the ISC PKP data [*Shearer*, 1994] is particularly difficult to interpret. In this section, we consider one such event located on the the Macquarie Ridge (Event 3). Figure 5.8 shows ray paths of the event to WWSSN and CAND stations. Both long-period and short-period records are collected with distance range of 121° to 173° and Φ angle up to 72°. In the following, the observations are divided up into a few distance ranges to examine the depth variation of the inner core anisotropy.

Figure 5.9 show short-period records from Event 3 before the PKP caustic. In contrast to Event 2 in Figure 5.6, clear precursors are observed here from 134° to 140°. Because of the strong PKP arrivals and very weak emergent direct PKP arrivals (see the dark arrow), it is very difficult to model these records. Nonetheless, we performed a sensitivity test using stations EDM and INK, which have the weakest precursors.

Figure 5.8: Ray paths from the Macquarie Ridge event (No.3).
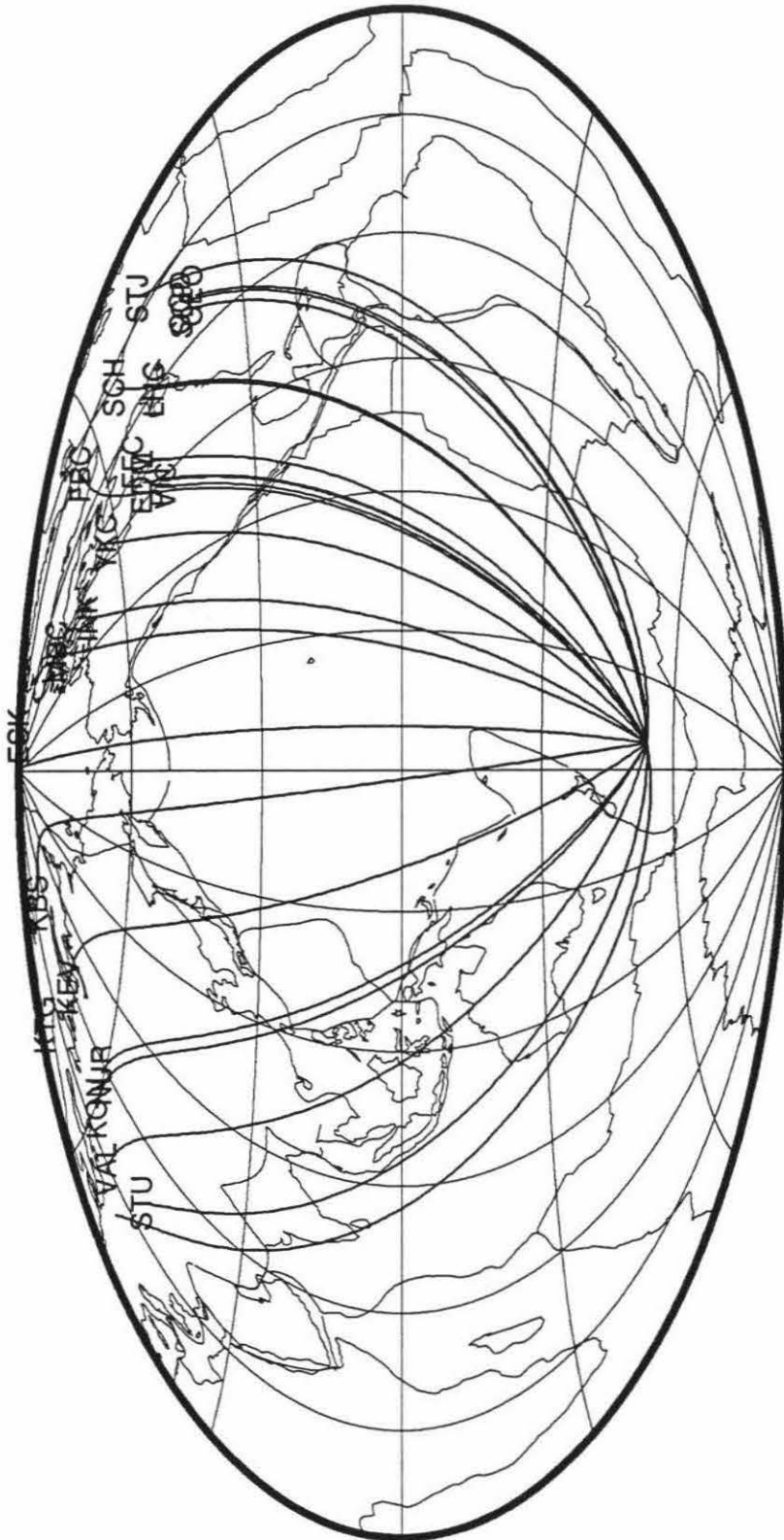
Figure 5.10 shows comparisons of the EDM and INK records (solid) and synthetics (dotted) from PREM2 and 3% uniform increase of P-wave velocity of PREM2 in the inner core. An average differential t* of 0.35s in PREM2 [*Song and Helmberger*, 1994a] was applied to DF arrivals for all the synthetics for Event 3. The empirical source function is obtained from the stack of VIC and PNT records. The synthetics from the model with 3% velocity increase show clear extra early arrivals compared to the synthetics from PREM2. However, there is no indication of these early arrivals in either record.

Figure 5.11 shows short-period records from Event 3 a few degrees after PKP caustic, where the three branches of PKP (DF, BC and AB) are observed. The data (solid) are aligned with BC arrivals in the synthetics (dotted). The AB arrivals in the data generally agree with PREM2 predictions. But the discrepancies between the DF arrivals from these polar paths and the synthetic predictions (PREM2) are clear. The differences of BC − DF times are about 1.0s to 1.5s except SCH, which is most non-polar in this range. The anomalies, however, are only a half of what was previous observed for a similar orientation from South Sandwich to College, Alaska or about 70% of the average [*Song and Helmberger*, 1993b] at the same orientation. Note this path was examined in a recent study from ISC DF travel times by *Shearer* [1994]. The data showed large scatter and no systematic anomalies were found for this path. Since this path provides a significant variation compared with numerous previous observations, it is important to analyze more reliable samples from this path for a more realistic model of inner core anisotropy. At this stage, it is difficult to know whether the variation comes from lateral variation or deviation of symmetry axis [*Su and Dziewonski*, 1994] or more complex models of anisotropy than the axi-symmetric

Jul 21, 1977 Macquarie Ridge
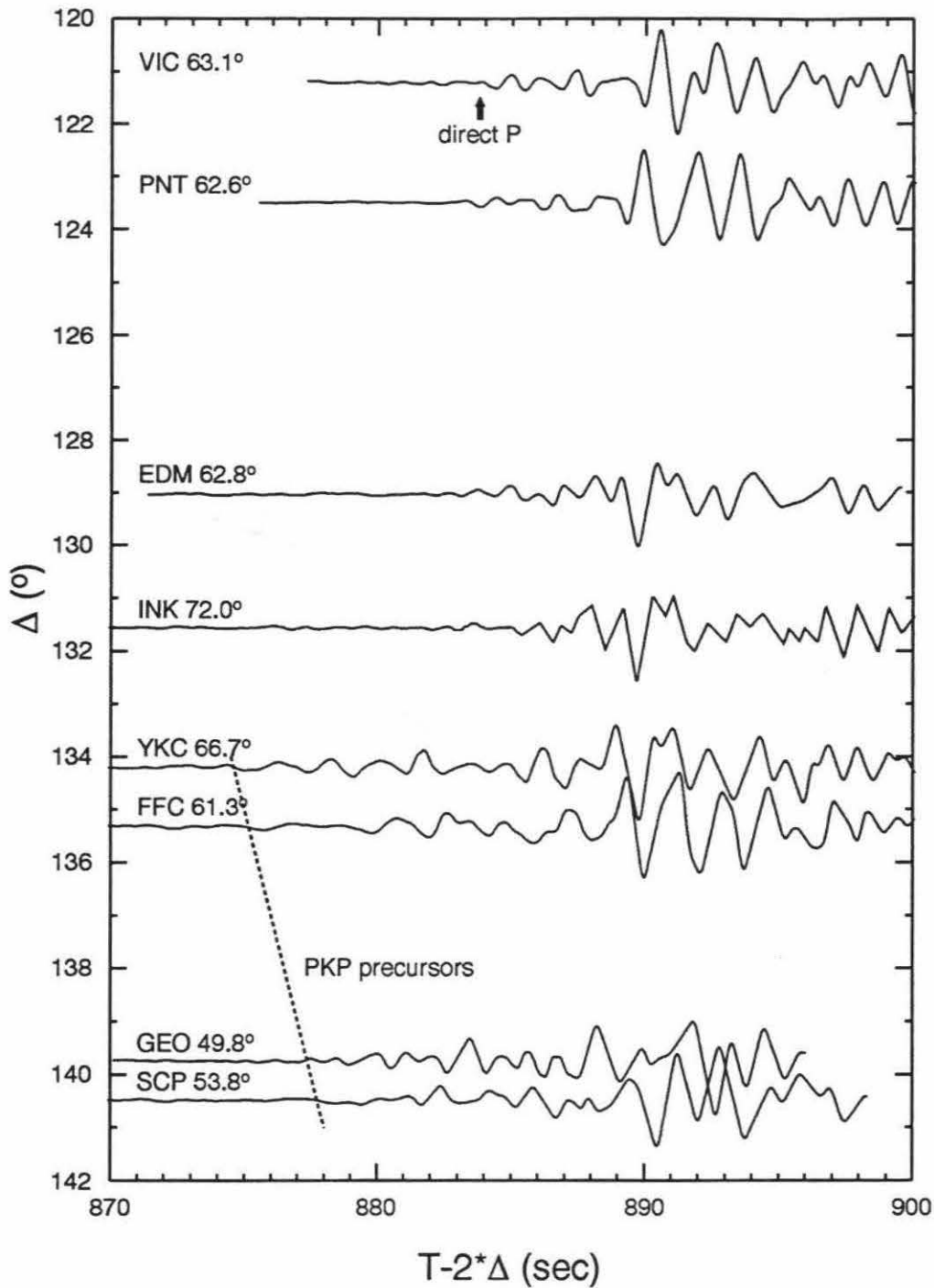
Figure 5.9: Short-period records from Event 3 before PKP caustic. Strong precursors and weak emergent direct PKP arrivals make waveform modeling very difficult.

Jul 21, 1977 Macquarie Ridge
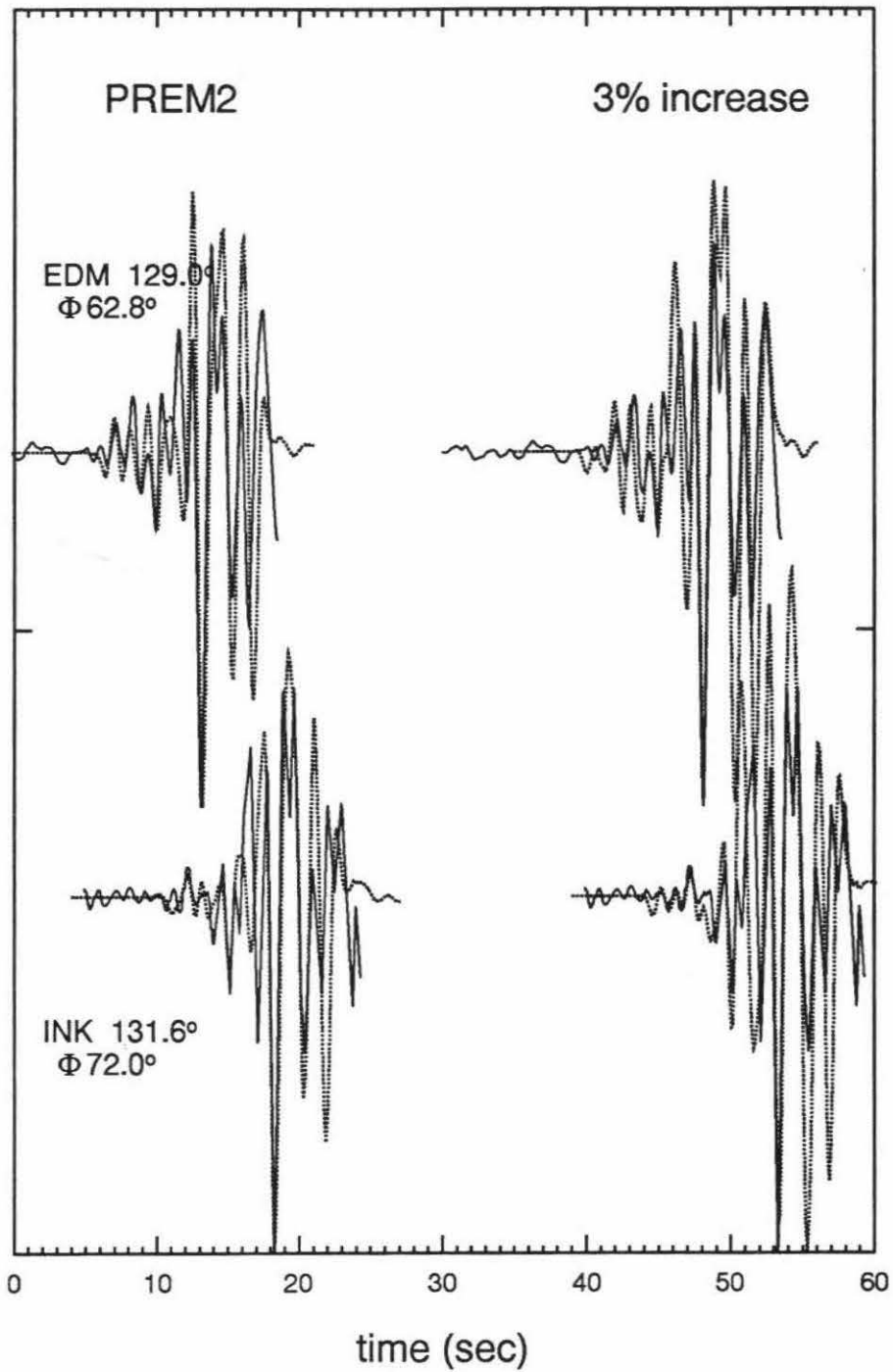
Figure 5.10: Comparisons of EDM and INK records from Event 3 with synthetics from PREM2 and 3% uniform increase of P-wave velocity of PREM2 in the inner core.

anisotropy.

Figure 5.12 shows comparisons of data from Event 3 and PREM2 synthetics at even larger distances. The attenuation model and source function used are the same as above. Note although VAL is not very polar, it shows a 1.5s time anomaly, suggesting that the inner core anisotropy might persist into the center of the Earth. If all of the anomaly is attributed to the anisotropy in the inner core, the anisotropy is roughly 3% throughout the sampling depth (close to 1000km) assuming the axisymmetric anisotropy around the spin axis. There is large uncertainty in this estimate, however, because of large variation (around 2s) in AB travel times [*Song and Helmberger*, 1993a]. Indeed, a recent study by *Vinnik et al.*[1994] suggests anisotropy as large as 3.5% persists into the center of the Earth from a more polar sample.

Results of waveform modeling of long-period records of Event 3 before the PKP caustic is shown in Figure 5.13. The fits of the synthetics from PREM2 to the observations are fairly good. The best polar path sample is from the station MBC near 140° and it fits PREM2 well indicating little need for anisotropy at this range. Note, however, the comparisons at smaller distance ranges can not resolve this feature as pointed out in the discussion of Figure 5.6.

Figure 5.14 shows comparisons of synthetic from PREM2 and the data after the PKP caustic. The fits are general consistent with the short-period results. The STJ record, however, shows anomalously small AB − DF time. Such anomalies are often observed [e.g., *Song and Helmberger*, 1994a] and are possibly due to lateral variation in the lowermost mantle. This is coupled with the observation that STJ takes quite a different ray path than a normal station such as STU at a corresponding distance (Figure 5.8). The time anomaly at station ESK is consistent with the anomaly
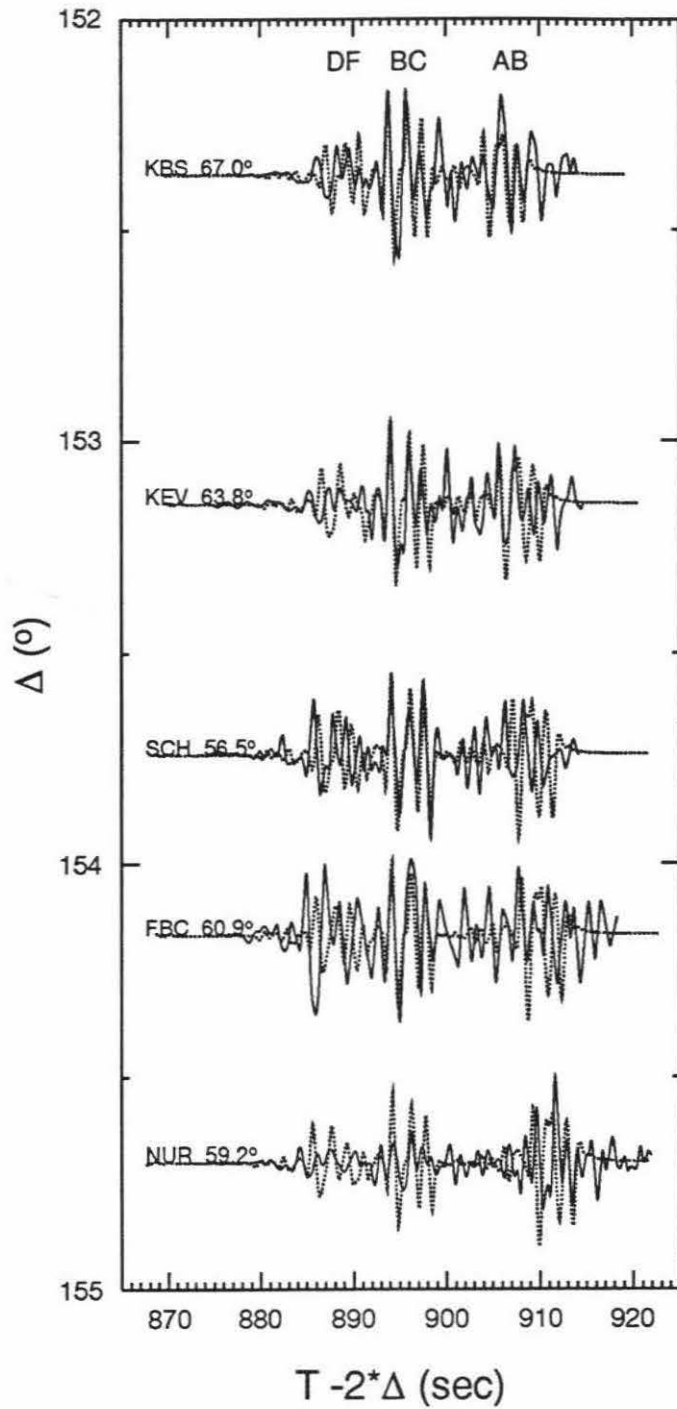
Figure 5.11: Comparisons of observations (solid) from Event 3 and synthetics from PREM2 (dotted) after the PKP caustic.

Jul 21, 1977 Macquarie Ridge
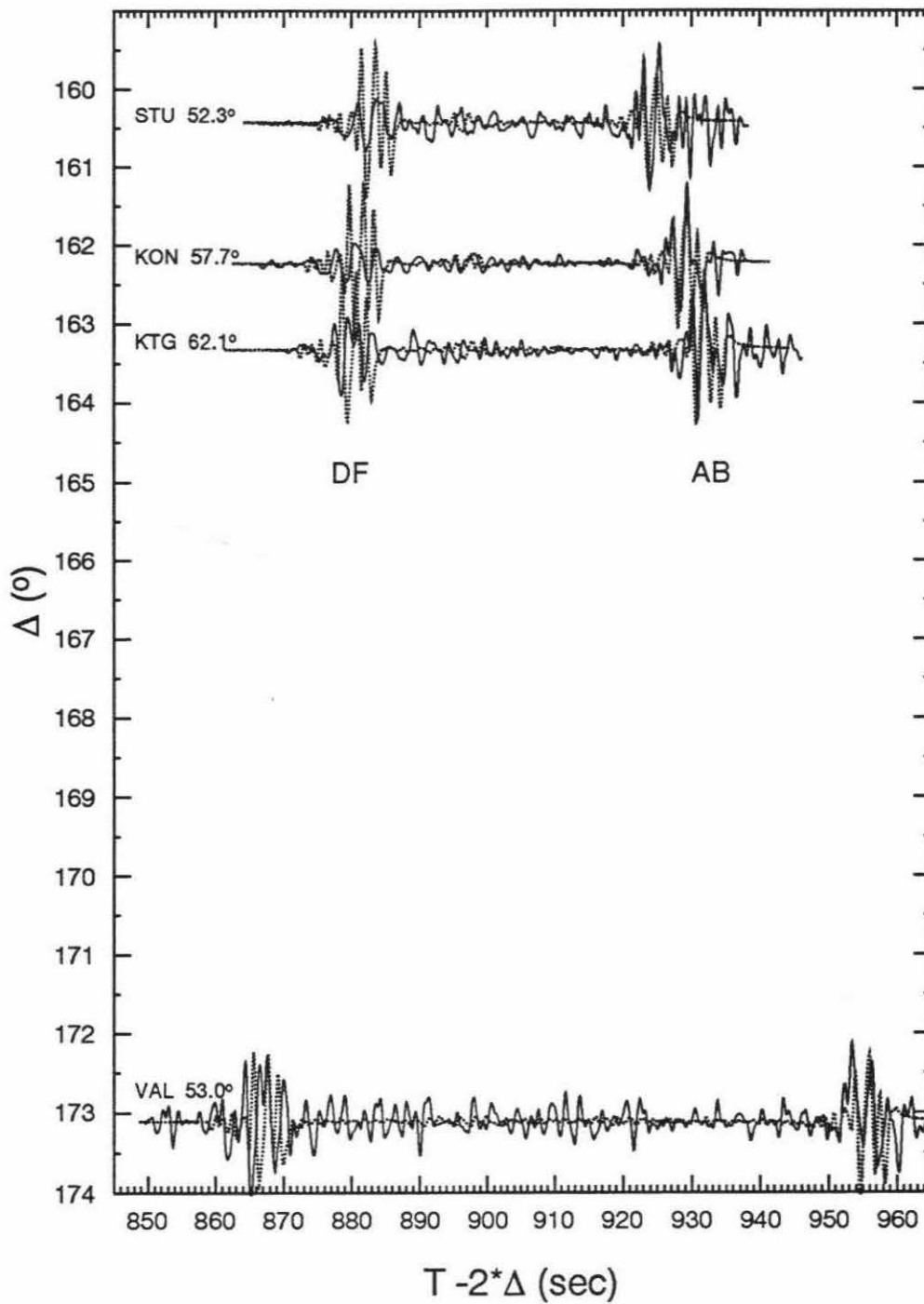
Figure 5.12: Comparisons of observations (solid) from Event 3 and synthetics from PREM2 (dotted) at greater distances.

Jul 21, 1977 Macquarie Ridge
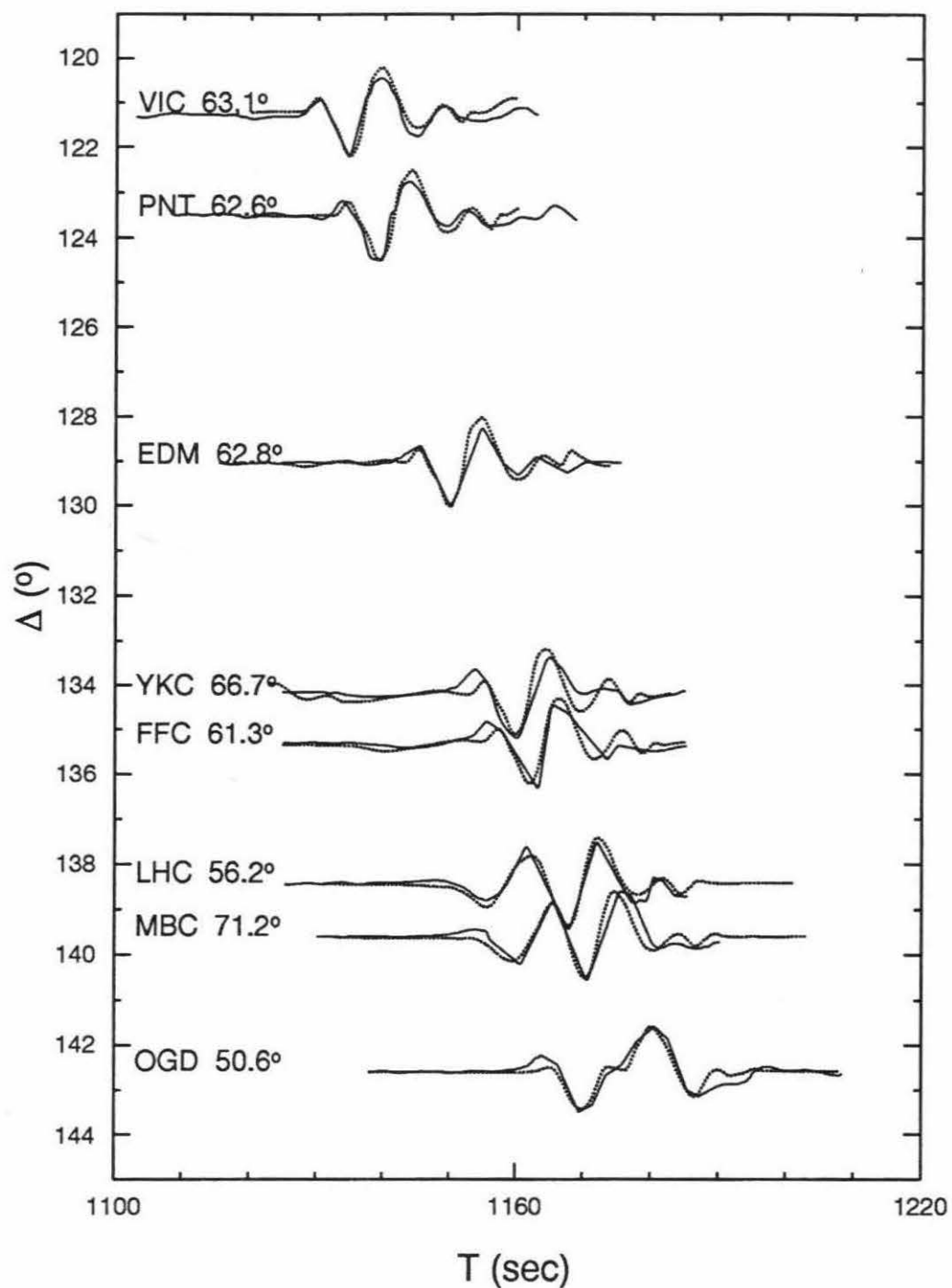
Figure 5.13: Comparisons of long-period records from Event 3 and PREM2 synthetics before PKP caustic. The fits are fairly well.

observed in the short-period record VAL (Figure 5.12), indicating the inner core anisotropy might persist to the center of the Earth.

5.4 Discussion and Conclusion

The main result of this study is that the anisotropy at the top 150km of the inner core is weaker than at greater depths. The anisotropy seems to disappear at the top 60km as indicated in Figure 5.6. The improved synthetic fits in Figure 5.5 from a distributed model of anisotropy at the top of the inner core (PREM2_NS) in the range of 140° to 146° seems to suggest a transition from isotopy at the top 60km to large anisotropy below 150km of the inner core. It then raise the question of what physical process could cause it. If the lattice preferred orientation of the hexagonally close-packed phase (ϵ-phase) of iron is responsible for the inner core anisotropy [e.g. *Brown and McQueen*, 1986; *Anderson*, 1986; *Jeanloz and Wenk*, 1988; *Sayers*, 1989; *Karato*, 1993], this could imply that a certain physical process prevents the formation of the lattice preferred orientation of ϵ-iron near the inner core boundary.

Earlier studies suggest a small anisotropy of 1% at the top 60km of the inner core from ISC DF travel times at distances from 132° to 140° [*Shearer*, 1988; 1994]. However, the result should be viewed with caution because of PKP precursors and weak emergent onsets of PKIKP due to inner core attenuation. For the same reason, other studies have windowed out data from ISC in this distance range [*Morelli et al.*, 1986; *Gudmundsson*, 1989; *Su and Dziewonski*, 1993; *Su and Dziewonski*, 1994].

The strength of anisotropy at the very top of the inner core has profound implication to our understanding of the splitting of normal modes. Some modes, such as $_{11}S_5$ and $_{16}S_6$, have very little energy in the inner core, and what little they have is
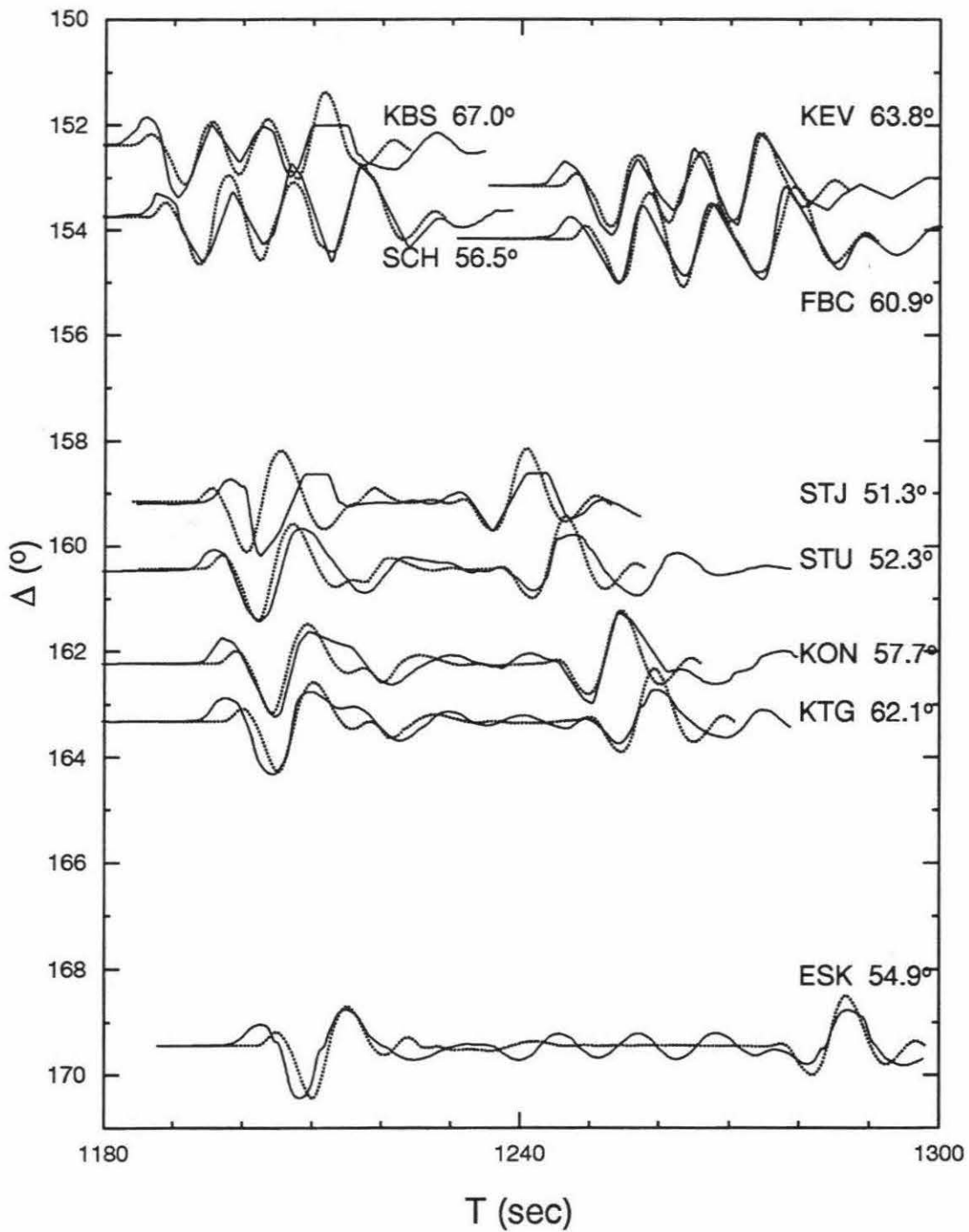
Figure 5.14: Comparisons of long-period records from Event 3 and PREM2 synthetics after the PKP caustic.

only sensitive to the very top [Tromp, personal communications]. Other mechanisms might be required to explain these modes that have puzzled normal mode community for many years [*Li et al.*, 1991a; *Widmer et al.*, 1992; *Masters*, 1993].

Chapter 6

Effect of Velocity Structure in D'' on the PKP Phases

6.1 Abstract

Differential travel times between various branches of PKP are used to study the P velocity structure in D''. Simple geometrical ray tests show that the ray path of the AB branch, which almost grazes the core-mantle boundary (CMB), is much more sensitive to the velocity structure in D'' than the DF and BC branches, which have small incident angles at the CMB. Thus, the differential travel times of AB and DF and AB and BC provide an effective means of studying lateral variations in D''. In a systematic search of six years of the GDSN short period data on CD-ROM, large anomalies in differential travel times of $AB - DF$ and $AB - BC$ were observed for different regions of D''. The scatter of $BC - DF$ data is half the scatter of $AB - DF$ and $AB - BC$ data, suggesting that the lowermost mantle has more influence on $AB - DF$ and $AB - BC$ data than the bottom of the outer core or

the top of the inner core. The mean of the AB − DF data set shows a 1 s offset relative to Preliminary Reference Earth Model (PREM) [*Dziewonski and Anderson,* 1981], in that $(AB - DF)_{prem}$ is smaller than $(AB - DF)_{obs}$. Variations of the lower mantle PREM model that contain a discontinuity or a more distributed 1.5% velocity reduction in the lower 500 km can explain the discrepancy. The largest variations in the AB − DF data are associated with paths sampling beneath the mid-Pacific. The AB − DF data along the mid-Pacific paths are about 1.0 s smaller than the average of the AB − DF from other paths and the differences are as large as 2.0 s at some distances.

6.2 Introduction

PKP phases are the first arrivals after the diffracted P arrival in the shadow zone. There are several branches associated with these phases on account of the discontinuities at the core-mantle boundary (CMB) and the inner core boundary (ICB). They are PKP-AB, PKP-BC and PKP-DF, which travel through the top of the outer core, the bottom of the outer core and the inner core, respectively (Figure 6.1). This study is based on the premise that P velocity structure in D'' has a stronger effect on AB than on BC or DF owing to the fact that PKP-AB almost grazes (incident angle over 70°) the CMB, while PKP-BC and PKP-DF have much smaller incident angles at the CMB (less than 30° for BC and less than 20° for DF) at distances larger than 150°. Thus, lateral variations in D'' can be assessed by mapping differential travel times between the AB and DF branches and the AB and BC branches. Since the ray paths of DF, BC and AB are similar in the upper mantle, differential travel times have some intrinsic advantages over techniques based on absolute travel

times [see *Creager and Jordan*, 1986]. Use of differential times eliminates the effects of uncertainties in event origin time, source duration and minimizes the effects of uncertainties in source location and the velocity variations of the crust and upper mantle under the source and receiver.

6.3 Method and Data

In a systematic survey of GDSN data, we observed considerable travel time anomalies between PKP-AB and PKP-DF. Figure 6.2 shows one example. The dotted line is a short period vertical response from a South America event recorded at station MAJO in Japan. The solid line is from Fiji-Tonga event recorded at station TOL in Spain. The focal depths and epicentral distances are 110 km and 182 km, respectively, and 155.46° and 155.76°, respectively. The DF and AB phases from these two seismograms line up perfectly. However, the differences in distances and focal depths result in about a 1.3 s correction in differential travel time of AB − DF from any reasonable global travel time model such as PREM. The differential travel time anomalies of BC − DF and AB − BC are about 0.5 s and 0.8 s, respectively.

Measurements of differential travel times from this type of digital data are easily obtained from the cross-correlation method (for example, Shearer and Toy, 1991). The DF and BC pulses were used directly in the cross-correlation analyses while the AB pulse was Hilbert transformed before applying this operation. The transformed nature of AB is quite apparent in the observed waveforms in Figure 6.2.

The survey included GDSN data documented on the CD-ROM from 1980 to 1986 for distances of 147° to 165°. We obtained 1898 event-station pairs. Of these, 47 high quality pairs for AB − DF with cross-correlation coefficients greater than 0.5 were
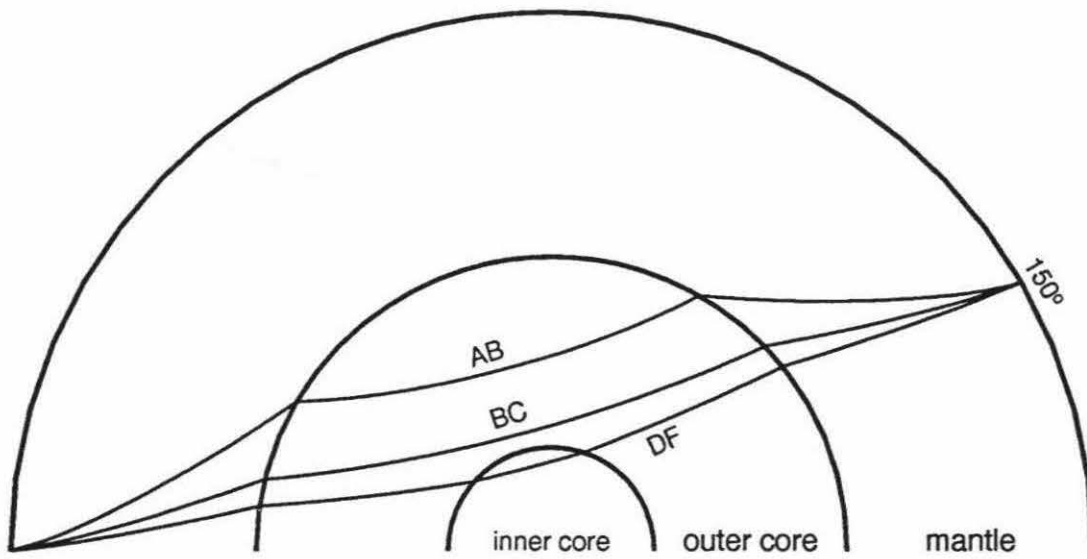
Figure 6.1: Ray paths of PKP-AB, PKP-BC, PKP-DF at 150°.

Figure 6.2: Data comparisons from two different paths showing large travel time anomalies. Dotted line is a short period GDSN vertical component seismogram from a South America event to MAJO, Japan. Solid line is a same type of seismogram from a Fiji-Tonga event to TOL, Spain.
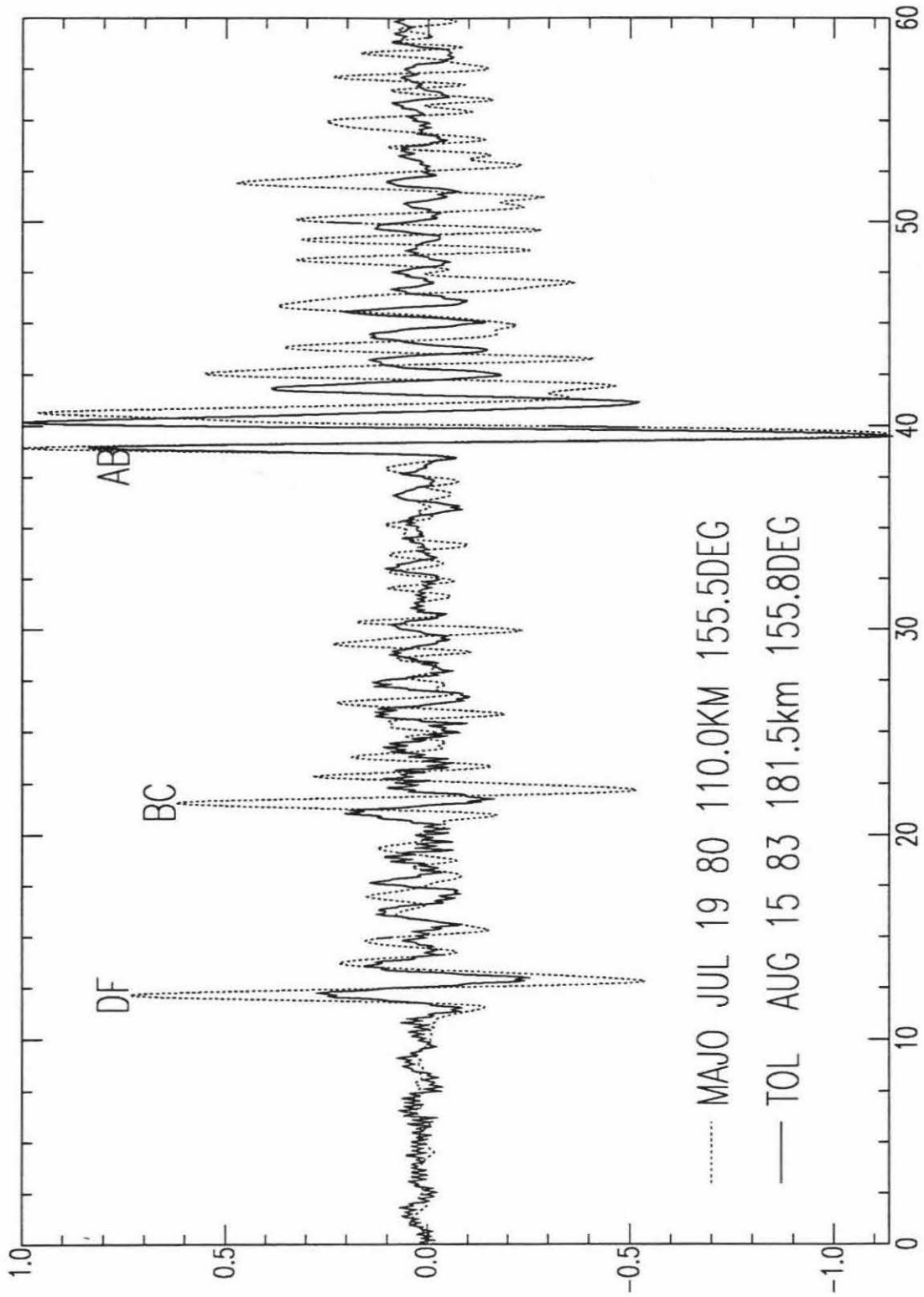
selected for further analyses. Figure 6.3 displays the event and station locations, six representative ray paths of station-event pairs and the intersection points of the ray paths for PKP-AB at CMB. The ray paths and the corresponding intersection points at CMB are designated by A, and B1 to B5 as shown in the figure. As we will see below, path A has smaller AB − DF times than paths B1 through B5.

Only a small fraction (less than 3%) of the data proved suitable for our study. There are several reasons for this. First, many station-event pairs were eliminated because they provided only a few samples, which did not appear useful considering the scatter in the data. The remaining 1191 pairs sample the six paths displayed in Figure 6.3. Second, data from shallow events are usually more complicated because of the surface reflected phases, thus their chances of being selected were greatly reduced. For example, the surface reflected phase pPKP-DF for events shallower than 100 km arrives close to PKP-AB after 155°, making identification difficult. This depth consideration reduced the 1911 pairs to only 328 pairs, which were further reduced to 47 pairs based on quality of fit. Reasons for bad correlations among the rest of the data are not very well understood. High background noise is one reason. Differential attenuation and scattering due to some unknown mechanism could be another reason. By experimenting with differential t*, one may improve the correlation. This approach has been used to study the inner core attenuation [see *Bhattacharyya*, 1993]. It is, however, not used in this study since it has little effect on the measurements of differential travel times. At any rate, since this high quality data set shows interesting results, we are confident that these rather selective measurements are meaningful.

The differential travel time measurements of AB − DF are summarized in Ta-

Figure 6.3: Summary ray paths of this study. The intersection points of PKP-AB with CMB are marked along the ray paths.
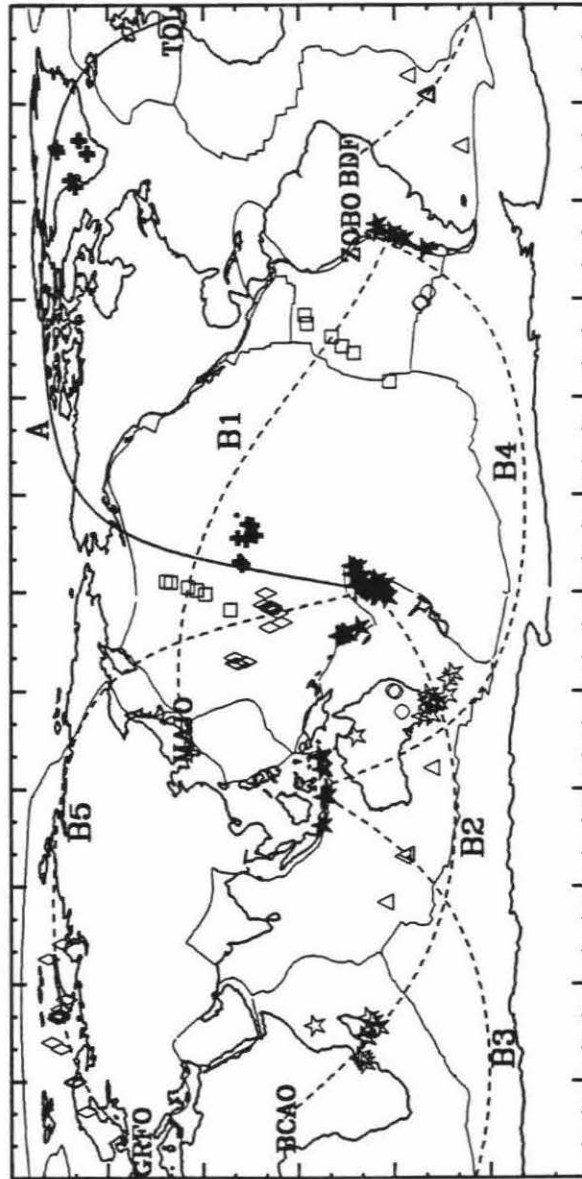
ble 6.1. Also listed are the cross correlation coefficient (CC) of DF and Hilbert-transformed AB (after flip of sign), the depth correction term (DEPC) and the ellipticity correction term (ELLC). The time window used in these cross-correlations is about 4 s, which contains only the main pulses. The depth correction was obtained by subtracting the differential travel time difference between a source at the correct event depth and a surface source predicted by PREM. In the following analyses, all differential times are corrected to a surface focus for direct comparisons. For these differential travel times, the depth correction is model insensitive. However, this correction is non-trivial as we see in the table and should be done carefully. The ellipticity correction was simple interpolations in distance and depth of the tables given by *Dziewonski and Gilbert* [1976].

Measurements of differential travel times $AB - BC$ and $BC - DF$ for the six groups of paths in this study are also obtained using the cross-correlation method. The depth correction and the ellipticity correction mentioned above are applied to each measurement. Whenever possible, all the differential travel times $AB - DF$, $AB - BC$ and $BC - DF$ are measured for cross-checking. The numbers of measurements with cross-correlation coefficients larger than 0.5 are 47 and 52 for $AB - BC$ and $BC - DF$, respectively. Thus, the lack of waveform coherency does not appear to be uniquely related to AB. The scatter of $BC - DF$ is about half the scatter of $AB - DF$ and $AB - BC$ from this data set. This suggests that the lowermost mantle has more influence on $AB - DF$ and $AB - BC$ data than the bottom of the outer core or the inner core. In the following, we discuss the effect of a few hypothetical models of D'' on the differential travel time $AB - DF$ and its possible implications.

Table 6.1. Differential travel times of AB and DF used in this study

PATH	STATION	DATE	ELAT	ELON	DEPTH	DELTA	AB-DF	CC	DEPC	ELLC
A	TOL	820602a	-18.1	-172.5	33.0	156.0	26.75	0.81	0.14	-0.15
A	TOL	820705c	-20.8	-178.8	615.3	160.4	45.05	0.85	4.46	-0.18
A	TOL	830415a	-19.2	-175.5	226.7	158.1	34.25	0.92	1.32	-0.16
A	TOL	830601b	-17.0	-174.6	179.6	155.7	27.15	0.75	0.97	-0.16
A	TOL	830610b	-24.2	-176.3	46.7	163.0	49.70	0.84	0.24	-0.15
A	TOL	830815a	-17.1	-174.5	181.5	155.8	27.00	0.93	0.99	-0.16
A	TOL	830830a	-16.7	-172.1	38.7	154.6	22.75	0.78	0.16	-0.15
A	TOL	860526a	-21.7	-179.3	603.8	161.4	48.60	0.77	4.41	-0.18
B1	MAJO	800611c	-32.7	-71.6	35.0	155.2	26.55	0.51	0.15	0.11
B1	MAJO	800719a	-29.0	-69.7	110.0	155.5	27.10	0.94	0.56	0.08
B1	MAJO	810919a	-39.1	-74.8	30.0	153.9	22.45	0.74	0.12	0.13
B1	MAJO	840611a	-30.7	-71.2	45.1	154.9	25.60	0.87	0.20	0.10
B1	MAJO	840812a	-24.4	-69.2	100.8	153.5	21.35	0.62	0.50	0.03
B1	MAJO	841020b	-24.3	-67.1	212.5	155.1	26.15	0.81	1.17	0.04
B2	BCAO	800115a	-22.2	-179.5	605.0	155.1	29.50	0.72	4.06	-0.17
B2	BCAO	800227a	-27.4	178.3	621.0	150.0	14.60	0.70	3.75	-0.16
B2	BCAO	800614a	-18.3	-178.0	553.0	158.7	40.45	0.80	3.81	-0.16
B2	BCAO	801226a	-22.2	-179.6	592.0	155.0	29.20	0.87	3.93	-0.17
B2	BCAO	810206a	-21.1	-178.9	618.0	156.2	32.95	0.50	4.24	-0.17
B2	BCAO	820419a	-26.0	-178.6	351.0	152.9	20.60	0.67	1.97	-0.19
B2	BCAO	820705c	-20.8	-178.8	615.3	156.5	33.65	0.73	4.24	-0.21
B2	BCAO	830207a	-26.7	-177.6	151.6	152.9	19.40	0.50	0.76	-0.20
B2	BCAO	830415a	-19.2	-175.5	226.7	159.9	41.25	0.77	1.34	-0.20
B2	BCAO	831106a	-20.1	-177.7	387.3	157.7	35.70	0.84	2.41	-0.18
B2	BCAO	831129c	-19.5	-177.8	527.0	158.1	37.90	0.59	3.56	-0.16
B2	BCAO	831228a	-13.1	166.8	141.3	147.5	6.35	0.50	0.64	-0.03
B3	BDF	821026b	-7.1	108.7	153.0	147.3	5.80	0.78	0.65	-0.13
B3	BDF	830820a	-8.5	117.6	156.2	151.8	17.65	0.84	0.77	-0.24
B3	BDF	840217a	-6.6	130.1	165.0	157.6	33.20	0.78	0.92	-0.39
B3	BDF	840117a	-7.7	117.4	303.9	152.4	20.00	0.73	1.66	-0.24
B4	ZOBO	800120b	-7.1	129.4	110.0	151.0	14.15	0.60	0.52	-0.19
B4	ZOBO	801023a	-6.6	129.6	160.0	151.2	14.55	0.66	0.78	-0.20
B4	ZOBO	821007a	-7.2	125.9	515.2	152.8	21.35	0.68	3.15	-0.26
B5	TOL	830404f	-15.0	167.3	123.0	154.0	22.90	0.95	0.62	-0.17
B5	TOL	850306a	-12.5	166.6	33.0	151.4	15.10	0.62	0.12	-0.16
B5	TOL	851006a	-18.9	169.4	255.9	158.4	36.60	0.55	1.52	-0.18
B5	TOL	860213b	-14.3	167.3	206.3	153.4	21.00	0.88	1.09	-0.17
B5	GRFO	800617a	-20.2	-178.4	580.0	149.5	13.30	0.53	3.38	-0.08
B5	GRFO	801130a	-19.4	-175.8	202.0	149.2	9.70	0.76	0.95	-0.08
B5	GRFO	811007a	-20.8	-178.6	619.0	150.0	14.70	0.77	3.74	-0.08
B5	GRFO	811125c	-20.9	-178.9	614.0	150.2	14.70	0.76	3.71	-0.08
B5	GRFO	820131a	-22.7	-179.2	500.0	151.8	19.05	0.52	2.96	-0.07
B5	GRFO	820512a	-24.6	179.2	532.0	153.3	23.85	0.83	3.32	-0.06
B5	GRFO	820705c	-20.8	-178.8	615.0	150.1	14.75	0.63	3.71	-0.08
B5	GRFO	830620a	-23.6	179.1	544.4	152.2	20.60	0.57	3.34	-0.06
B5	GRFO	830701a	-20.8	-178.3	529.4	150.1	14.30	0.59	3.06	-0.08
B5	GRFO	830821c	-23.5	-177.1	150.5	153.0	19.30	0.75	0.76	-0.07

6.4 Results and Discussion

The differential travel times $AB - DF$ displayed in Table 6.1 are plotted in Figure 6.4. Different symbols are used to distinguish data from various paths as shown in Figure 6.3. We see that differential travel times for sample A are consistently smaller than differential travel times for other paths. The differences are about 1.0 s on average and the maximum differences near 156° are as large as 2.0 s. In spite of the quality control on the data selection, we still see this large variation along different paths.

A variety of P velocity structures near the CMB displayed in Figure 6.5 were tested to interpret the data. All the testing models are modifications of PREM (solid line). Model DDL is a Lay-type discontinuity model [*Lay and Helmberger*, 1983b] with a near constant velocity starting at 590 km above the CMB, a velocity increase of 2.7% at 253 km above the CMB and a pronounced negative gradient down to the CMB. It has a structure similar to the shear wave model SYL1 [*Young and Lay*, 1987]. Models DNG, DPG and DFL represent a family of models with smoothly changing velocities but different gradients at the base of the mantle, similar to those proposed in previous studies (for example, Mula and Müller, 1980). Model DNG deviates from PREM at 150 km above CMB and has a significant negative gradient down to CMB with a 1% decrease in V_p at the CMB. Model DPG deviates from PREM at 500 km above CMB and has a positive gradient down to CMB with a 1.5% decease at the CMB. Model DFL has a flat velocity structure in the bottom 500 km of the lower mantle ending in a 3% reduction at the CMB.

The predicted differential travel times $AB - DF$ of these models are plotted in Figure 6.4 along with the observations. By comparing the observations with pre-

Figure 6.4: Differential travel times AB − DF of the observations and the predictions from various lower mantle models. The differential travel times have been corrected to surface focuses.

PKP-AB - PKP-DF

165
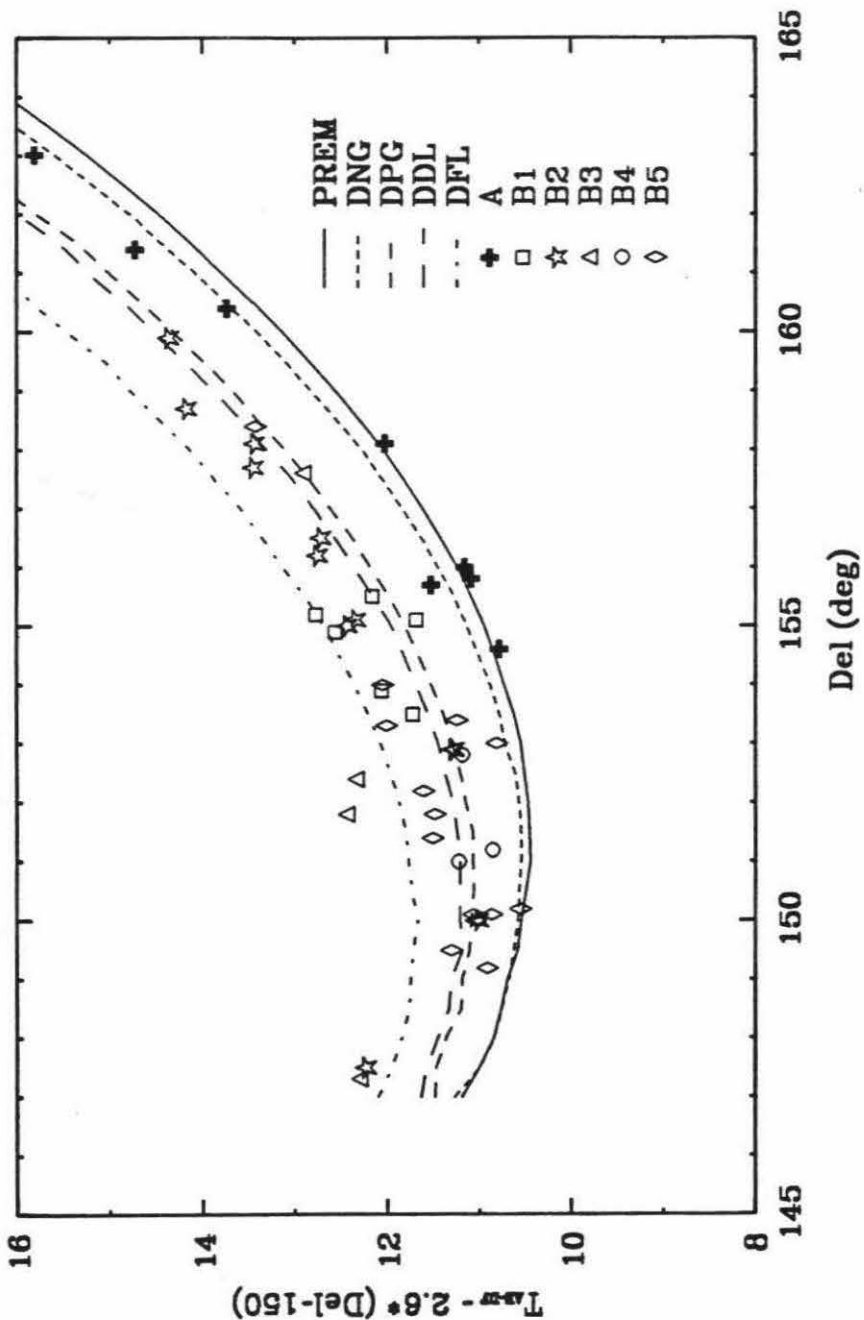
Figure 6.5: Test models for P-wave velocity in the lowermost mantle.
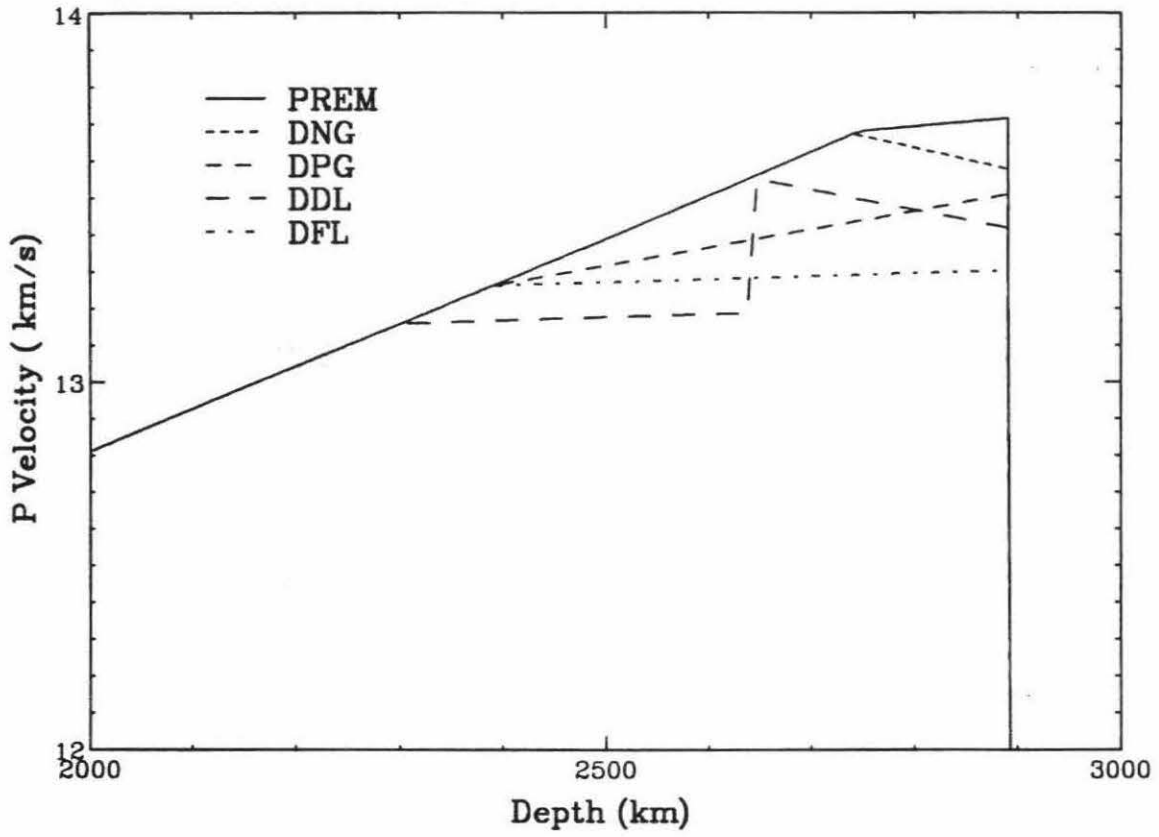
dictions from the models, we conclude the following. (1) PREM falls on the lower bound of the data. It failed to predict the average of the AB − DF data by about 1.0 s. (2) Model DFL can serve as an upper bound of the data. The velocity decrease in the model effectively slows down AB much more than DF and, thus, increases the differential travel time AB − DF. (3) Model DNG fits the data from path A slightly better than PREM at larger distances. The negative velocity gradient in the model DNG effectively slows down AB more at larger distances and, thus, noticeably increases $dT/d\Delta$. Note that $dT/d\Delta$ predicted by PREM is too small at distances larger than 158°. (4) Model DPG and model DDL fit the data from paths B1 to B5 equally well on the average. This suggests, on the one hand, that velocity in D'' must be slowed down considerably from PREM to fit the the average of the observations and, on the other hand, that we cannot identify the existence of a discontinuity from these differential data alone. (5) Relatively speaking, path A samples faster regions than path B1 to B5 in the lowermost mantle. The variations are about 1% in the lowermost 500 km of the mantle.

The above analysis assumes that the travel time anomalies are due to the velocity variations in the lowermost mantle. Other factors which also affect the differential travel time include topographical variations in D'', velocity variations in the outermost core as well as aspherical structure in the inner core.

The reported peak-to-peak long wavelength (up to degree 6) topography of CMB ranges from the order of 1 km to the order of 10 km [*Gwinn et al.*, 1986; *Hager et al.*, 1985; *Morelli and Dziewonski*, 1987]. The observed AB − DF travel time anomalies requires a peak-to-peak value of about 30 km assuming such a long wavelength topography. This high value should be detectable by travel time tomography even

taking into account 5 km to 10 km uncertainties from the International Seismological Center (ISC) data [*Gudmundsson and Clayton*, 1991]. Hence, the long wavelength CMB topography cannot explain the observed AB − DF anomalies although it might be contributing.

The lateral variations of the outer core are considered to be small because of the extremely low viscosity [*Stevenson*, 1987]. So if we only consider variations near its boundary, the topmost core region, the effect on AB − DF is also small since the ray path of AB is steepened again when entering the outer core (the incident angle is less than 35°). Some evidence suggest the existence of aspherical structure in the inner core as well as in the lowermost outer core [*Creager*, 1992]. We consider these variations, however, to be smaller than the variations in the lowermost mantle because the variation in both AB − DF and AB − BC observations is two times larger than the variation in BC − DF observations.

Still another important factor is that DF and AB sample different velocity structures in the lower mantle since their paths are separated by about 1300 km to 2000 km near the CMB at the ranges 150° to 160°. This situation is similar to SKS and S data [*Garnero et al.*, 1988] where one favored explanation for large S-SKS anomalies is that S and SKS sample different velocity structures when crossing a laterally varying *D″*. *Garnero and Helmberger* [1993b] persued the study furthur by comparing the direct S-SKS observations with predictions from tomographic models of the mantle. They concluded that predictions from tomographic models show general agreement with the azimuthal variations of S-SKS from Fiji-Tonga to North America and 3-D models may ultimately account for all of the S-SKS anomalies. In the Appendix to this chapter, we describe the comparisons of predictions from

taking into account 5 km to 10 km uncertainties from the International Seismological Center (ISC) data [*Gudmundsson and Clayton*, 1991]. Hence, the long wavelength CMB topography cannot explain the observed AB − DF anomalies although it might be contributing.

The lateral variations of the outer core are considered to be small because of the extremely low viscosity [*Stevenson*, 1987]. So if we only consider variations near its boundary, the topmost core region, the effect on AB − DF is also small since the ray path of AB is steepened again when entering the outer core (the incident angle is less than 35°). Some evidence suggest the existence of aspherical structure in the inner core as well as in the lowermost outer core [*Creager*, 1992]. We consider these variations, however, to be smaller than the variations in the lowermost mantle because the variation in both AB − DF and AB − BC observations is two times larger than the variation in BC − DF observations.

Still another important factor is that DF and AB sample different velocity structures in the lower mantle since their paths are separated by about 1300 km to 2000 km near the CMB at the ranges 150° to 160°. This situation is similar to SKS and S data [*Garnero et al.*, 1988] where one favored explanation for large S-SKS anomalies is that S and SKS sample different velocity structures when crossing a laterally varying D''. *Garnero and Helmberger* [1993b] persued the study furthur by comparing the direct S-SKS observations with predictions from tomographic models of the mantle. They concluded that predictions from tomographic models show general agreement with the azimuthal variations of S-SKS from Fiji-Tonga to North America and 3-D models may ultimately account for all of the S-SKS anomalies. In the Appendix to this chapter, we describe the comparisons of predictions from

tomographic models of the mantle and the AB − DF observations. The results show that the model predictions are in poor agreement with the observations. However, the effect of 3-D velocity structure in the lowermost mantle on the PKP differential times is very important even on the wavelength of current tomographic models.

The P velocity variations in the lowermost mantle observed from the AB − DF differential travel times agree well with the variations derived from direct ISC PKP-DF and PKP-AB arrivals by *Creager and Jordan* [1986] and less well with the lower mantle model by *Dziewonski* [1984] based on ISC direct P arrivals. Figure 6.6 shows the AB − DF travel time residuals relative to model DPG. The residuals are marked on both the entering and exit points of the AB ray paths at CMB. There is a general good agreement between fast and slow regions in this study and the (AB+DF) anomaly map in *Creager and Jordan* [1986]. For example, they find the Southeastern Pacific and the region below Australia to be slow, in agreement with our results. The velocity variations in this study, however, are larger than in their study by a factor of two. This is a reasonable result considering that the ISC data have been binned and averaged. One significant difference between their results and ours occurs in the mid-Pacific which they consider fast, while we see more structure with only the region beneath Hawaii as fast. One should bear in mind, however, that the travel time anomaly from a particular path is the accumulations of anomalies along the whole path, especially along both ends of the lowermost mantle. There is no way to assess the contributions from either end with this analysis. Nevertheless, our data appear to be sampling the same lower mantle anomaly as seen in the study of SKS-S by *Garnero et al.* [1988]. This latter study suggests that the region beneath Hawaii is faster than the neighbouring regions in S wave.

Figure 6.6: AB − DF travel time residuals relative to model DPG in Figure 6.5 marked on both the entering and exit points of the AB ray paths at the CMB. A positive residual indicates that the AB phase is slowed down relative to DF, suggesting a slow velocity anomaly for 1-D velocity models.

AB-DF residuals
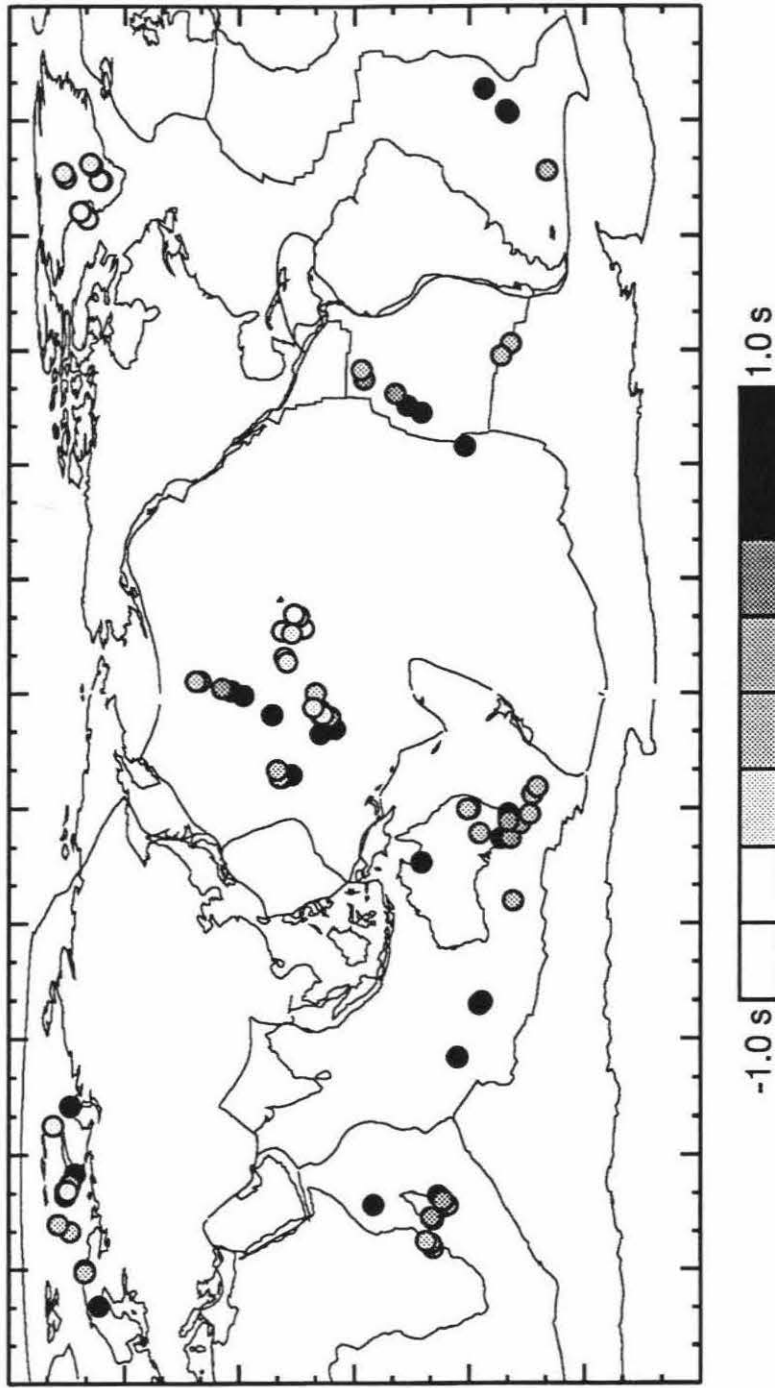
6.5 Conclusions

Velocity structure in D'' has stronger influence on AB than DF and thus can be constrained by PKP differential travel times. Large variations in differential travel times $AB - DF$ were observed from short period GDSN data sampling different regions of the lowermost mantle. $AB - DF$ time predictions of PREM are on average 1.0 s smaller than our observations, suggesting the D'' V_p structure in PREM is too fast. The largest variations in the data are associated with paths sampling beneath the mid-Pacific. The variations in $AB - DF$ for the mid-Pacific paths are about 1.0 s smaller than the average of the rest of the data and are as much as 2.0 s smaller at some distances. These regional variations in the lowermost mantle are consistent with anomalies seen in the ISC direct PKP picks but our anomalies are about twice as large in magnitude.

6.6 Appendix: Predictions from Tomographic Models of the Mantle

In this Appendix, we examine a few tomographic models of the mantle for the same ray geometry of the data presented in the text. The purpose is to have a quantitative understanding of the effect of 3-D velocity structure on $AB - DF$ differential travel times and to provide a direct comparison of model predictions and the observations. This direct comparison is somewhat encouraged by a recent study of *Garnero and Helmberger* [1993b], which demonstrates that tomographic models are in general agreement with the azimuthal variations observed in S-SKS differential times beneath the Central Pacific from Fiji-Tonga to North America.

The models tested include S-wave models and P-wave models as summarized in Table 6.2. In calculating travel time residuals from the S-wave models, the scaling factor of 0.5 is used, i.e., $d\ln Vp=0.5d\ln Vs$. The choice of this value is somewhat arbitrary but has been suggested in the literature [*Jordan and Lynn*, 1974; *Lay* 1983a; *Dziewonski and Woodhouse*, 1987; *Anderson*, 1987; *Li et al.*, 1991b].

The travel time perturbation of each individual ray path from a tomographic model is calculated by summing up velocity perturbations along the ray path, as illustrated in Figure 6.7. In this example, model SH12_WM13 is used for path A, which is from Fiji-Tonga region to Toledo, Spain. The upper panel shows velocity variations of SH12_WM13 at the CMB. The solid and dashed curves are the minor and major arcs of the great circle of the path, respectively. The lower panel shows the cross section of the great circle and ray paths of DF and AB phases. The ray paths are obtained for the homogeneous PREM model. Fermat's principle implies that the time residual due to velocity perturbations, to first order, is the integral of

Model	Reference	Parameterization (lateral/radial)	Data
MDLSH	*Tanimoto* [1990]	L=6/11 layers	waveforms of long period (40-100s) SH body waves and long-period (100-500s) Love waves
SH12_WM13	*Su et al.* [1992]	L=12/Chebyshev polynomials deg. 13	travel times of S, SS; differential times of ScS-S, SS-S and waveforms of mantle waves
SH.10C.17	*Masters et al.* [1992]	L=10/11 layers	travel times of S, SS SSS; differential times of SS-S, ScS-S, sScS-s and free-oscillation structure coefficients
L02.56	*Dziewonski* [1984]	L=6/Legendre polynomials deg. 5 (lowermantle only)	500 thousand ISC P times at 30° to 90° from 1964 to 1979
CMB1	*Creager and Jordan* [1986]	L=5 (CMB only)	ISC travel times : 925,983 PKP-DF and 6,968 PKP-AB
IFTO90SH	*Inoue et al.* [1990]	L=25/16 layers	2 million ISC P times from 1964 to 1985

Table 6.2: Tomographic models of the mantle used to compute AB − DF times in this study.

the velocity perturbations along the ray path [e.g., *Nolet*, 1987]:

$$\delta T \approx \int_{\text{path}} \frac{-\delta v}{v^2} ds = \int_{\text{path}} \frac{-\delta v}{v} dt$$

As mentioned in the discussion section, the 3-D velocity structure such as displayed in Figure 6.7 has important implications on $AB - DF$ times. Firstly, these rays are likely to sample very different velocity anomalies at the entrance points and exit points at the CMB. This is certainly true in 6.7. Secondly, the separation of the DF ray path and AB ray path at the CMB (1300km to 2000km) is close to one wavelength of tomographic models, $2\pi r_{\text{cmb}}/L$, or 1800km for SH12_WM13. Thus DF and AB may sample different anomalies in the lowermost mantle, which is also true in this example. Figure 6.8 provides one quantification of these 3-D effects. It shows how the $AB - DF$ differential times or residuals are accumulated through the depth of the mantle. The upper panel shows the depth accumulation of $AB - DF$ calculated for spherically symmetric model (1-D) at distance 155°. We see that 50% of the different time comes from bottom 500km of the mantle and more than 70% from bottom 1/3 of the mantle. The lower panel shows the depth accumulation of $AB - DF$ residuals from model SH12_WM13. We see the curves have much more structure in the lower most mantle than what we would expect from a 1-D model. This suggests that DF and AB rays are sensing different velocity anomalies and the 3-D velocity structure are constantly modifying $AB - DF$ times that we observe in the surface. However, even for this more realistic model, it is still true that 70% of the $AB - DF$ residuals are from model perturbations in the bottom 1/3 of the mantle. The model perturbations in the top 2/3 of the mantle are are heavily dumped.

Figures 6.9 and 6.10 show comparisons of predictions from the P- and S-wave tomographic models and the observed $AB - DF$ residuals. The observed residuals

Figure 6.7: Travel time perturbations along individual ray paths. The upper panel shows velocity variations of SH12_WM13 at the CMB along with lateral projection of path A. The solid and dashed curves are the minor and major arcs of the great circle of the path, respectively. The lower panel shows the cross section of the model along the great circle and the DF and AB ray paths. The time perturbation for a particular path is, to first order, the integral of the velocity perturbations along the ray path.

SH12_WM13 CMB
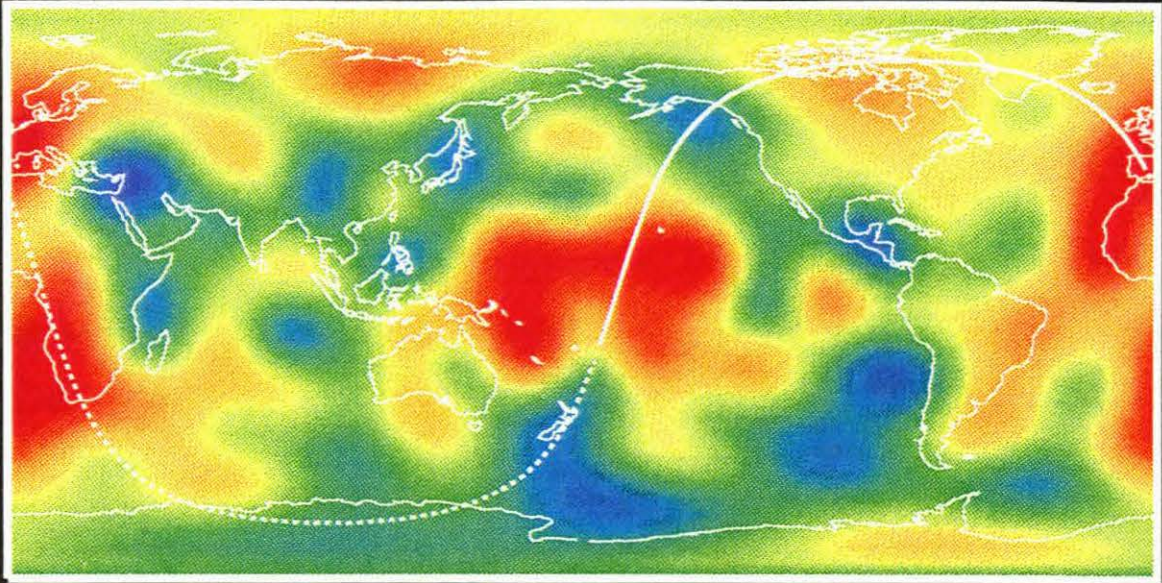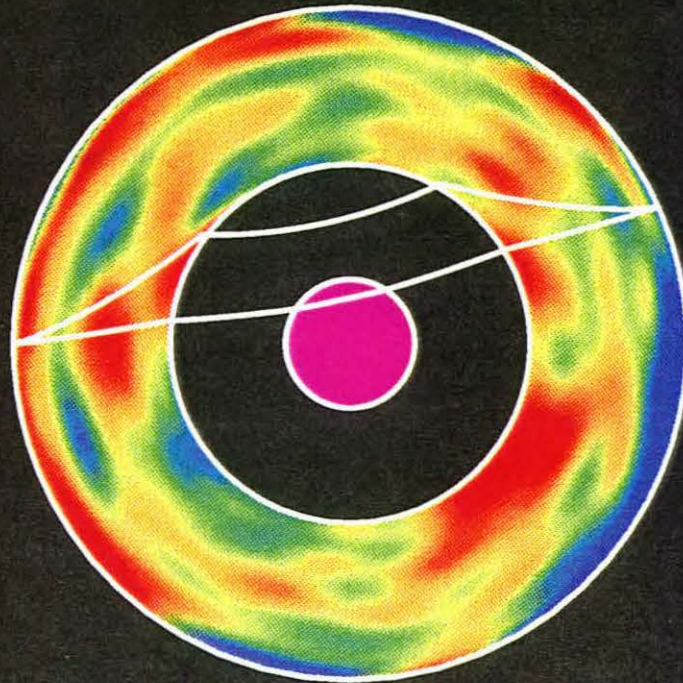
Figure 6.8: An illustration of effects of 3-D structure on AB − DF residuals. The upper panel shows the accumulation of AB − DF differential travel times as a function of depth in the mantle. It is calculated for a spherically symmetric model (1-D), such as PREM, at distance 155°. The lower panel shows the accumulation of AB − DF residuals calculated from a tomographic model (SH12_WM13). The curves in the lower panel have much more complex structure than 1-D predictions in the lowermost mantle, suggesting the DF and AB are sensing different velocity anomalies.

How does AB-DF stack up in the mantle?
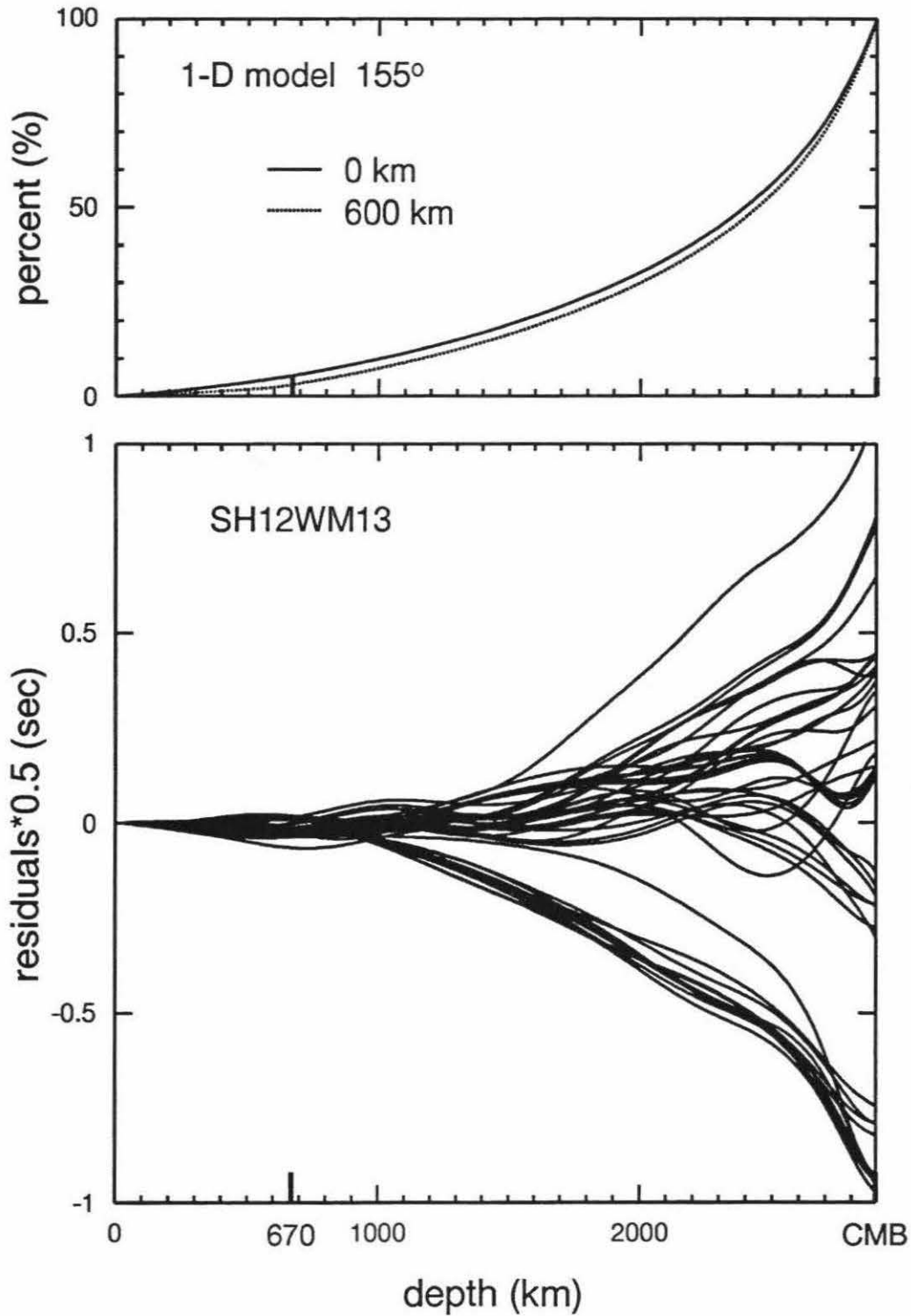
(top panels) are relative to PREM. The predictions from PREM2 fall roughly on the average of the data as discussed in Chapter 3. Apparently, none of the models produce the pattern of the observed anomalies. CMB1 seems to be the only model to predict systematic differences between path A and path B2 as observed in the data. The predictions from SH12_WM13 and SH.10C.17 for these two paths seem to be anti-correlated with the observations. Early studies also suggested poor and sometimes anti-correlation between P-wave anomalies and S-wave anomalies [*Bolton and Masters*, 1992; *Wysession*, 1993]. This might also explain the discrepancy between the lack of correlation on the AB − DF data in this study and some correlation on the SKS-S data by *Garnero and Helmberger* [1993b]. However, we cannot rule out the possibility that the tomographic models have too broad wavelengths to explain these high frequency observations. The lack of correlations on other paths as well suggests that this might well be the case.

In summary, the velocity structure in the lowermost mantle has strong impact on AB − DF differential times and thus can be constrained by these differential travel time measurements. However, 3-D velocity structure should be taken into account in mapping these differential travel time anomalies to velocity perturbations in the lowermost mantle. The tomographic models are not successful in explaining the observed AB − DF anomalies. Thus, it is questionable to attribute body wave travel time anomalies to the Earth's core after mantle corrections before higer resolution tomographic models are obtained.

Figure 6.9: Predictions of AB − DF residuals from S-wave tomographic models along with the observed AB − DF residuals (relative to PREM). Note the S-wave model predictions have been scaled by a factor of 1/2.

182
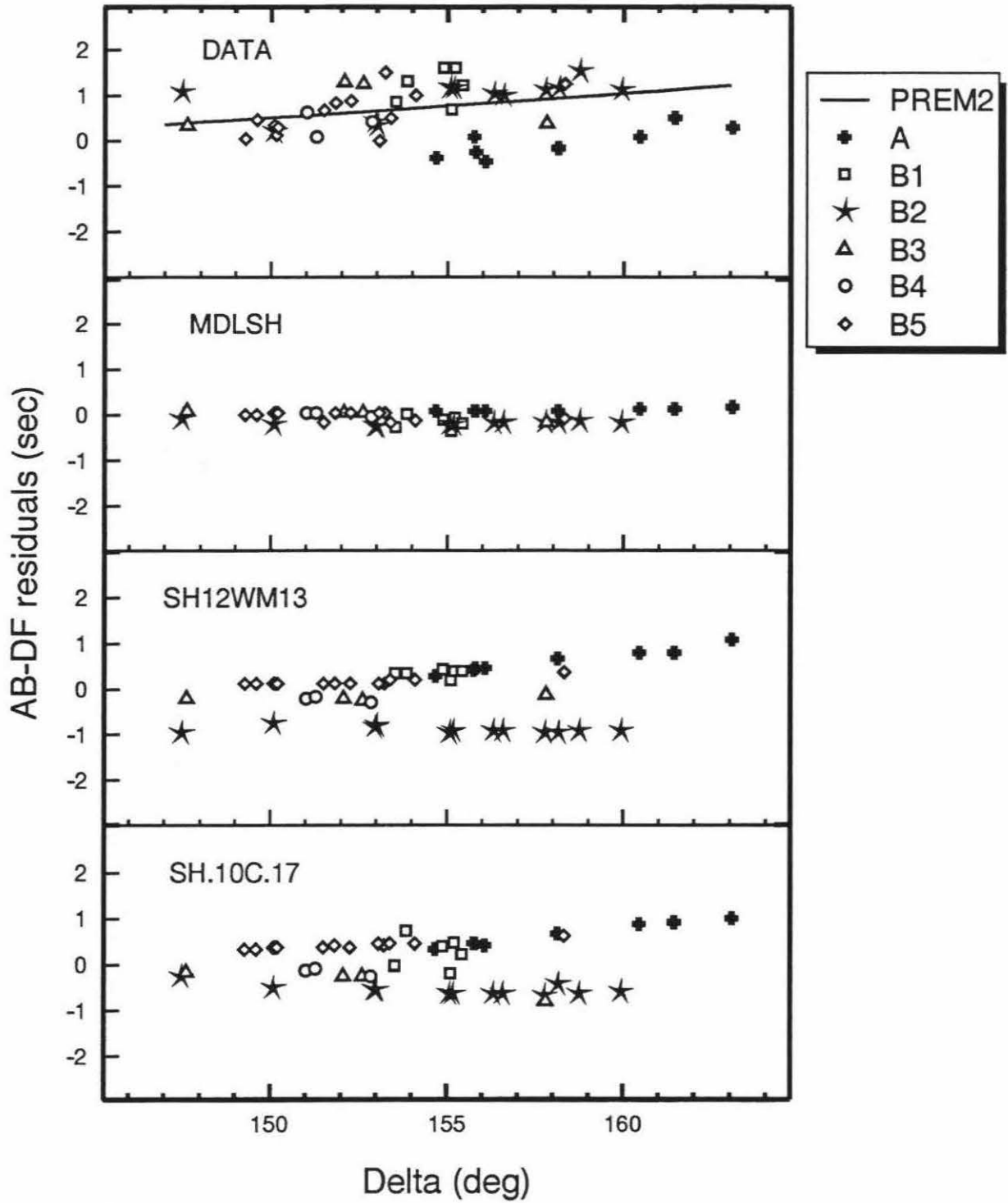
Figure 6.10: Predictions of AB − DF residuals from P-wave tomographic models along with the observed AB − DF residuals (relative to PREM).
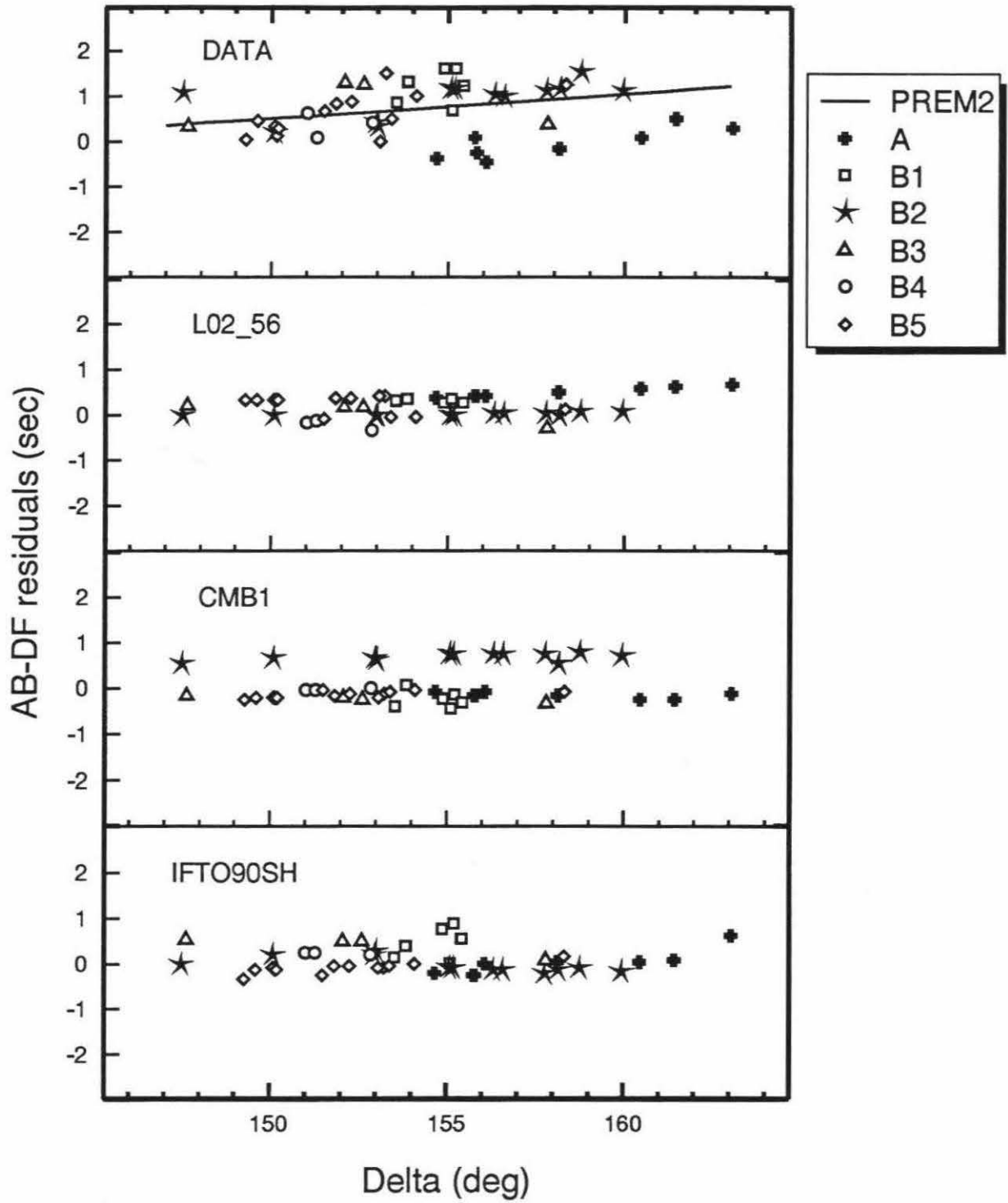
Bibliography

Aki, K., and P.G. Richards. *Quantitative Seismology: Theory and Methods*, W.H.Freeman, San Francisco, Calif., 1980.

Anderson, D.L., and R.S. Hart. An Earth model based on free oscillations and body waves, *J. Geophys. Res.*, *81*, 1461-1475, 1976.

Anderson, D.L. A Seismic Equation of State II. Shear properties and thermodynamics of the lower mantle, *Phys. Earth Planet. Inter.*, *45*, 307-323, 1987.

Anderson, D.L. *Theory of the Earth*, Blackwell Scientific Publications, Osney Mead, Oxford, UK, 1989.

Anderson, O.L. Properties of iron at the earth's core conditions, *Geophys. J. R. Astron. Soc.*, *84*, 561-579, 1986.

Anderson, W.W., and T.J. Ahrens. An equation of state for liquid iron and implications for the Earth's core, *J. Geophys. Res.*, *99*, 4273-4284, 1994.

Bhattacharyya, J., P.M. Shearer, and G. Masters. Inner-core attenuation from short-period PKP(BC) versus PKP(DF) wave-forms, *Geophys. J. Int.*, *114*, 1-11,1993.

Birch, F. Elasticity and constitution of the Earth's interior, *J. Geophys. Res.*, *57*, 1952.

Bolt, B. Gutenberg's early PKP observations, *Nature*, *196*, 122-124, 1962.

Bolt, B. The velocity of seismic waves near the Earth's center, *Bull. Seismol. Soc. Am.*, *54*, 191-208, 1964.

Bolt, B. The constitution of the core: seismological evidence, *Phil. Trans. R. Soc. Lond.*, *306*, 11-20, 1982.

Bolton, H., and G. Masters. S/P ratios in the lower mantle (abstract), *EOS, Trans. AGU.*, *73*,40 3, 1992.

Brown, J.M, and R.G. McQueen. Phase-transitions, gruneisen-parameter, and elasticity for shocked iron between 77-GPA and 400-GPA, *Geophys. J. R. Astron. Soc.*, *91*, 7485 -7494, 1986.

Brush, S.G. Discovery of the Earth's core, *Am. J. Phys.*, *48*, 705-724, 1980.

Bullen, K.E. An index of degree of chemical inhomogeneity in the Earth, *Geophys. J.*, *7*, 584-592, 1963.

Bullen, K.E., and B. Bolt. *An introduction to the theory of seismology*, Cambridge Univ. Press, 4th Ed., 1985.

Choy, G.L., and V.F. Cormier. The structure of the inner core inferred from short-period and broadband GDSN data, *Geophys. J. R. Astron. Soc.*, *72*, 1-21, 1983.

Cormier, V.F., and P.G. Richards. Full wave theory applied to a discontinuous velocity increase: the inner core boundary, *J. Geophys.*, *43*, 3-31, 1977.

Cormier, V.F., and G.L. Choy. A search for lateral heterogeneity in the inner core from differential travel times near PKP-D and PKP-C, *Geophys. Res. Lett.*, *13*, 1553-1556, 1986.

Creager, K. C., and T. H. Jordan. Aspherical structure of the core-mantle boundary from PKP travel times, *Geophys. Res. Lett.*, *13*, 1497-1500, 1986.

Creager, K. C. Anisotropy of the inner core from differential travel times of the phases PKP and PKIKP, *Nature*, *356*, 309-314, 1992.

Cummins, P., and L. Johnson. Short-period body wave constraints on properties of the Earth's inner core boundary, *J. Geophys. Res.*, *93*, 9058-9074, 1988.

Davies, D., and B.R. Julian. A study of short period P-wave signals from LONG-SHOT, *Geophys. J. R. Astron. Soc.*, *29*, 185-202, 1972.

Doornbos, D.J. Observable effects of the seismic absorption band in the Earth, *Geophys. J. R. Astron. Soc.*, *75*, 693-711, 1983.

Doornbos, D.J. Multiple scattering by topographic relief with application to the core-mantle boundary, *Geophys. J.*, *92*, 465-478, 1988.

Dziewonski, A.M., A.L. Hales, and E.R. Lapwood. Parametrically simple earth models consistent with geophysical data, *Phys. Earth Planet. Inter.*, *10*, 12-48, 1975.

Dziewonski, A.M., and F. Gilbert. The effect of small, aspherical perturbations on travel times and a re-examination of the corrections for ellipticity, *Geophys. J. R. Astron. Soc.*, *44*, 7-17, 1976.

Dziewonski, A.M., and D.L. Anderson. Preliminary reference Earth model, *Phys. Earth Planet. Inter.*, *25*, 297-356, 1981.

Dziewonski, A.M. Mapping the lower mantle: Determination of Lateral Heterogeneity in P velocity up to Degree and Order 6, *J. Geophys. Res.*, *89*, 5929-5952, 1984.

Dziewonski, A.M., and J.H. Woodhouse. Global images of the Earth's interior, *Science*, *236*, 37-48, 1987.

Garnero, E., D. V. Helmberger, and G. Engen. Lateral variations near the core-mantle boundary, *Geophys. Res. Lett.*,*15*, 609-612, 1988.

Garnero, E., D. V. Helmberger, and S.P. Grand. Constraining outermost core velocity with SmKS waves, *Geophys. Res. Lett.*, *20*, 2463-2466, 1993a.

Garnero, E., D. V. Helmberger, and S.P. Grand. Travel Times of S and SKS: Implications for three-dimensional lower mantle structure beneath the central pacific, *J. Geophys. Res.*, *98*, 8225-8241, 1993b.

Grand, S.P., and D.V. Helmberger. Upper mantle shear structure of North America, *Geophys. J. R. Astron. Soc.*, *76*, 399-438, 1984.

Gudmundsson, O., R.W. Clayton, and D.L. Anderson. Is there anisotropy in the outer core? (abstract), *EOS, Trans. AGU.*, *68*, 1378, 1987.

Gudmundsson, O. Some problems in global tomography: modeling the core-mantle boundary and statistical analysis of travel-time data, *Ph.D. Thesis*, California Institute of Technology, Pasadena, California, 1989.

Gudmundsson, O., and R. W. Clayton. A 2-D synthetic study of global traveltime tomography, *Geophys. J. Int.*, *106*, 53-65, 1991.

Gutenberg, B., and C.F. Richter. P' and the Earth's core, *Mon. Not. R. Astr. Soc., Geophys. Sup.*, *4*, 363-372, 1939.

Gwinn, C. R., T. A. Herring, and I. I. Shapiro. Geodesy by radio interferometry: studies of the forced nutations of the earth 2. interpretation, *J. Geophys. Res.*, *91*, 4755-4765, 1986.

Haddon, R.A.W. Corrugations on the mantle core boundary or transition layers between inner and outer cores? (abstract), *Eos, Trans. AGU*, *53*, 600, 1972.

Häge, H. Velocity constraints for the inner core inferred from long-period PKP amplitudes, *Phys. Earth Planet. Inter.*, *31*, 171-185, 1983.

Hager, B. H., R. W. Clayton, M. A. Richards, R. P. Comer, and A. M. Dziewonski. Lower mantle heterogeneity, dynamic topography and the geoid, *Nature*, *313*, 541-545, 1985.

Hales, A.L., and J.L. Roberts. The velocities in the outer core, *Bull. Seismol. Soc. Am.*, *61*, 1051-1059, 1971.

Helmberger, D., and R.A. Wiggins. Upper mantle structure of midwestern United States, *J. Geophys. Res.*, *76*, 3229-3245, 1971.

Helmberger, D.V. Theory and application of synthetic seismograms, *Earthquakes: Observation*, Theory and Interpretation, *LXXXV Corso*, 1983.

Inoue, H., Y. Fukao, K. Tanabe, and Y. Ogata. Whole mantle P-wave travel time tomography, *Phys. Earth Planet. Inter.*, *59*, 294-328, 1990.

Jeanloz, R., and H.R. Wenk. Convection and anisotropy of the inner core, *Geophys. Res. Lett.*, *15*, 72-75, 1988.

Jeanloz, R. The nature of the Earth's core, *Annu. Rev. Earth Planet. Sci.*, *18*, 357, 1990.

Jeffreys, H. The times of the core waves, M.N.R.A.S., *Geophys. Suppl.*, 4, 548-561, 1939a.

Jeffreys, H. The times of the core waves (second paper), M.N.R.A.S., *Geophys. Suppl.*, 4, 594-615, 1939b.

Jeffreys, H., and Bullen. *Seismological Tables*, British Association for the Advancement of Science, London, 1940.

Jephcoat, A., and P. Olson. Is the inner core of the Earth pure iron, *Nature*, *325*, 332-335, 1987.

Johnson, L.R., and R.C. Lee. Extremal bounds on the P velocity in the Earth's core, *Bull. Seismol. Soc. Am.*, *75*, 115-130, 1985.

Jordan, T.H., and W.S. Lynn. A velocity anomaly in the lower mantle, *J. Geophys. Res*, *79*, 2679-2685, 1974.

Karato, S. Inner core anisotropy due to the magnetic field-induced preferred orientation of iron, *Science*, *262*, 1708-1711, 1993.

Kendall, J.M., and P.M. Shearer. Lateral variations in D'' thickness from long-period shear-wave data, submitted to *J. Geophys. Res.*, 1994.

Kennett, B.L.N., and E.R. Engdahl. Traveltimes for global earthquake location and phase identification, *Geophys. J. Int.*, *105*, 429-465, 1991.

Lamb, H. On the propagation of tremors over the surface of an elastic solid, *Philos. Trans. Ro. Soc. London, Ser. A*, *203*, 1-42, 1904.

Lay, T. Localized velocity anomalies in the lower mantle, *Geophys. J. R. Astron. Soc.*, *72*, 483-516, 1983a.

Lay, T., and D.V. Helmberger. A lower mantle *S*-wave triplication and the shear velocity structure of D'', *Geophys. J. R. Astron. Soc.*, *75*, 799-837, 1983b.

Lay, T., and D.V. Helmberger. The shear-wave velocity gradient at the base of the mantle, *J. Geophys. Res.*, *88*, 8160-8170, 1983c.

Lehmann, I. P', *Bur. Cent. Seismol. Int. A*, *14*, 3, 1936.

Li, X.-D., D. Giardini, and J.H. Woodhouse. Large-scale three-dimensional even-degree structure of the Earth from splitting of long-period normal modes, *J. Geophys. Res.*, *96*, 551-577, 1991a.

Li, X.-D., D. Giardini, and J.H. Woodhouse. The relative amplitudes of mantle heterogeneity in P velocity, S velocity and density from free-oscillation data, *Geophys. J. Int.*, *105*, 649-657, 1991b.

Masters, T.G., and P.M. Shearer. Structure of the Earth - mantle and core, *Rev. Geophys.*, *29*, 671-679, 1991.

Masters, T.G., H. Bolton, and P.M. Shearer. Large-scale 3-dimensional structure of the mantle (abstract), *EOS, Trans. AGU.*, *73*, 201, 1992.

Masters, T.G. Core models ring true, *Nature*, *366*, 629-630, 1993.

McSweeney, T.J. and K.C. Creager. Depth extent of inner-core anisotropy from PKP phases recorded at the Alaska Seismic Network, *EOS Trans.*, *AGU*, 74, 407, 1993.

Mellman, G.R., and D.V. Helmberger. High-frequency attenuation by a thin high-velocity layer, *Bull. Seismol. Soc. Am.*, *64*, 1383-1388, 1974.

Michelini A., and T.V. McEvilly. Seismological studies at Parkfield. I. Simultaneous inversion for velocity structure and hypocenters using cubic B-splines parameterization, *Bull. Seismol. Soc. Am.*, *81*, 524-552, 1991.

Morelli, A., A.M. Dziewonski, and J.H. Woodhouse. Anisotropy of the inner core inferred from PKIKP travel times, *Geophys. Res. Lett.*, *13*, 1545-1548, 1986.

Morelli, A., and A.M. Dziewonski. Topography of the core-mantle boundary and lateral homogeneity of the liquid core, *Nature*, *325*, 678-683, 1987.

Morelli, A., and A.M. Dziewonski. Body wave traveltimes and a spherically symmetric P- and S-wave velocity model, *Geophys. J. Int.*, *112*, 178-194, 1993.

Mortenson, M.E. *Geometric Modeling*, John Wiley & Sons, Inc., 113-125, 1985.

Mula, A.H., and G. Müller. Ray parameters of diffracted long period P and S waves and the velocities at the base of the mantle, *Pageoph*, *118*, 1272-1292, 1980.

Müller, G. Amplitude studies of core phases, *J. Geophys. Res.*, *78*, 3469-3490, 1973.

Nolet, G. (Ed.), *Seismic tomography* with application in global seismology and exploration geophysics, D. Reidel Publishing Company, Dordrecht, Holland, 1987.

Poupinet, G., R. Pillet, and A. Souriau. Possible heterogeneity of the Earth's core deduced from PKIKP travel times, *Nature*, *305*, 204-206, 1983.

Qamar, A. Revised velocities in the Earth's core, *Bull. Seismol. Soc. Am.*, *63*, 1073-1105, 1973.

Rial, J.A., and V.F. Cormier. Seismic waves at the epicenter's antipode, *J. Geophys. Res.*, *85*, 2661-2668, 1980.

Richards, P.G. Calculation of body waves, for caustics and tunnelling in core phases, *Geophys. J. R. Astron. Soc.*, *35*, 243-264, 1973.

Richards, P.G. Seismic wave propagation effects - Development of theory and numerical modeling, *Kerr, Ann U. The VELA Program; a twenty-five year review of basic research.* Def. Adv. Res. Projects Agency, Arlington, Va., 183-226, 1985.

Roudil, P., and A. Souriau. Liquid core structure and PKP station anomalies derived from PKP(BC) propagation times, *Phys. Earth Planet. Inter.*, *77*, 225-236, 1993.

Sacks, I.S., J.A. Snoke, and L. Beach. Lateral heterogeneity at the base of the mantle revealed by observations of amplitudes of PKP phases, *Geophys. J. R. Astron. Soc.*, *59*, 379-387, 1979.

Sayers, C.M. Seismic anisotropy of the inner core, *Geophys. Res. Lett.*, *16*, 267-270, 1989.

Shearer, P.M., K.M. Toy, and J.A. Orcutt. Axi-symmetric Earth models and inner-core anisotropy, *Nature*, *333*, 228-232, 1988.

Shearer, P.M., and G. Masters. The density and shear velocity contrast at the inner core boundary, *Geophys. J. Int.*, *102*, 491-498, 1990.

Shearer, P.M., and K.M. Toy. PKP(BC) versus PKP(DF) differential travel times and aspherical structure in the Earth's inner core, *J. Geophys. Res.*, *96*, 2233-2247, 1991.

Shearer, P.M. Constraints on inner core anisotropy from ISC PKP(DF) data, submitted to *J. Geophys. Res.*, 1994.

Song, X.D., and D.V. Helmberger. Velocity structure near the inner core boundary from waveform modeling, *J. Geophys. Res.*, *97*, 6573-6586, 1992.

Song, X.D., and D.V. Helmberger. Effect of velocity structure in D'' on PKP phases *Geophys. Res. Lett*, *20*, 285-288, 1993a.

Song, X.D., and D.V. Helmberger. Anisotropy of Earth's inner core, *Geophys. Res. Lett*, *20*, 2591-2594, 1993b.

Song, X.D., and D.V. Helmberger. A P-wave velocity model of the Earth's core, submitted to *J. Geophys. Res.*, 1994a.

Song, X.D., and D.V. Helmberger. Depth dependence of inner core anisotropy, submitted to *J. Geophys. Res.*, 1994b.

Souriau, A., and G. Poupinet. A Latitudinal pattern in the structure of the outermost liquid core, revealed by the travel times of SKKS-SKS seismic phases, *Geophys. Res. Lett.*, *17*, 2005-2007, 1990.

Souriau, A., and G. Poupinet. The velocity profile at the base of the liquid core from PKP(BC+C_{diff}) data: An argument in favor of radial inhomogeneity, *Geophys. Res. Lett.*, *18*, 2023-2026, 1991.

Stevenson, D.J. Limits on lateral density and velocity variations in the earth's outer core, *Geophys. J. R. Astr. Soc.*, *88*, 311-319, 1987.

Su, W.J., R.L. Woodward, and A.M. Dziewonski. Joint inversions of travel-time and waveform data for the 3-D models of the Earth up to degree 12 (abstract), *EOS, Trans. AGU.*, 73, 201-202, 1992.

Su, W.J., and A.M. Dziewonski. Towards consistent P and S 3-D models of the mantle, *EOS, Trans. AGU.*, 74, 213, 1993.

Su, W.J., and A.M. Dziewonski. Inner core anisotropy in three dimensions, submitted to *Nature*, 1994.

Tanimoto, T. Long-wavelength S-wave velocity structure throughout the mantle, *Geophys. J. Int.*, 100, 327-336, 1990.

Tromp J. Support for anisotropy of the Earth's inner core from free oscillations, *Nature*, 366, 678-681, 1993.

Vinnik, L., B. Romanowicz, and L. Breger. Anisotropy in the inner core from the broadband records of the geoscope network, submitted to *Geophys. Res. Lett.*, 1994.

Wessel, P., and W.H.F. Smith. Free software helps map and display data, *EOS Trans. AGU*, 72, 441, 445-446, 1991.

Widmer, R. W., G. Masters, and F. Gilbert. Observably split multiplets - data analysis and interpretation in terms of large-scale aspherical structure, *Geophys. J. Int.*, 111, 559-576.

Woodhouse, J.H., D. Giardini, and X.-D. Li. Evidence for inner core anisotropy from free oscillations, *Geophys. Res. Lett.*, 13, 1549-1552, 1986.

Wysession, M.E., E.A. Okal, and C.R. Bina. The structure of the core-mantle boundary from diffracted waves, *J. Geophys. Res.*, 97, 8749-8764.

Young, C.J., and T. Lay. Evidence for a shear velocity discontinuity in the lower mantle beneath India and the Indian Ocean, *Phys. Earth Planet. Inter.*, 49, 37-53, 1987.

Appendix A

Bézier Curves

A Bézier curve was used in Chapter 3 to model subtle P velocity gradients at the base of the outer core. Here I give a brief description of the curve, which is widely used in the computer aided design (CAD) industry. This might be helpful to understand why it allows a more flexible control on the velocity gradients at the lowermost outer core in constructing velocity models for the region. More details on Bézier curve and other curve design can be found in *Mortenson* [1985].

Without lose of generality, we consider only 3rd-order Bézier curve, which can be represented by a parametric cubic curve as follows, in a matrix form:

$$\mathbf{P}(t) = \begin{bmatrix} t^3 & t^2 & t & 1 \end{bmatrix} \mathbf{C}\mathbf{G} = \mathbf{F}\mathbf{G}. \tag{A.1}$$

Where $t \in [0,1]$ is the parametric variable; $\mathbf{C}$ is the conversion (or transformation) matrix (4x4); $\mathbf{G}$ is the matrix of geometric coefficients; and

$$\mathbf{F} = \begin{bmatrix} f_0 & f_1 & f_2 & f_3 \end{bmatrix} = \begin{bmatrix} t^3 & t^2 & t & 1 \end{bmatrix} \mathbf{C} \tag{A.2}$$

193

are called the blending functions.

The matrix of geometric coefficients (**G**) contains points on the curve and/or their derivatives. There are at least two ways to design a curve. One way is by interpolation, in which the curve passes through all the desired points (defined in **G**). In this case, the curve is represented by parametric polynomials. Many previous Earth models were expressed in this way, including PEM [*Dziewonski et al.*, 1975], PREM [*Dziewonski and Anderson*, 1981], and IASP91 [*Kennett and Engdahl*, 1991]. This approach has two main disadvantages for our purpose of modeling a local structure. One problem is that the shape of the curve is difficult to control. If one point is changed, the whole curve will change. Another problem is that polynomials are oscillatory.

Bézier curve provides another approach. A 3rd-order Bézier curve is controlled by two end points and their first derivatives. It is not affected by other curve segments. Specifically:

The transformation matrix

$$
\mathbf{C} = \begin{bmatrix} -1 & 3 & -3 & 1 \\ 3 & -6 & 3 & 0 \\ -3 & 3 & 0 & 0 \\ 1 & 0 & 0 & 0 \end{bmatrix}.
\tag{A.3}
$$

The matrix of geometric coefficients

$$\mathbf{G} = \begin{bmatrix} \mathbf{P}_0 \\ \mathbf{P}_a \\ \mathbf{P}_b \\ \mathbf{P}_1 \end{bmatrix} = \begin{bmatrix} \mathbf{P}_0 \\ \mathbf{P}_0 + \frac{1}{3}\mathbf{P'}_0 \\ \mathbf{P}_0 - \frac{1}{3}\mathbf{P'}_1 \\ \mathbf{P}_1 \end{bmatrix}. \tag{A.4}$$

Where $\mathbf{P}_0$, $\mathbf{P}_a$, $\mathbf{P}_b$, $\mathbf{P}_1$ are given. They are the control points of the Bézier curve. Note $\mathbf{P}_a$ and $\mathbf{P}_b$ are related to the end point derivatives $\mathbf{P'}_0$ and $\mathbf{P'}_1$, respectively.

From (A.1), the 3rd-order Bézier curve

$$
\begin{aligned}
\mathbf{P}(t) &= \begin{bmatrix} t^3 & t^2 & t & 1 \end{bmatrix} \begin{bmatrix} -1 & 3 & -3 & 1 \\ 3 & -6 & 3 & 0 \\ -3 & 3 & 0 & 0 \\ 1 & 0 & 0 & 0 \end{bmatrix} \begin{bmatrix} \mathbf{P}_0 \\ \mathbf{P}_a \\ \mathbf{P}_b \\ \mathbf{P}_1 \end{bmatrix} \\
&= \begin{bmatrix} (1-t)^3 & 3t(1-t)^2 & 3t^2(1-t) & t^3 \end{bmatrix} \begin{bmatrix} \mathbf{P}_0 \\ \mathbf{P}_a \\ \mathbf{P}_b \\ \mathbf{P}_1 \end{bmatrix} \\
&= (1-t)^3\mathbf{P}_0 + 3t(1-t)^2\mathbf{P}_a + 3t^2(1-t)\mathbf{P}_b + t^3\mathbf{P}_1.
\end{aligned}
\tag{A.5}
$$

It is trivial to verify that $\mathbf{P}(0) = \mathbf{P}_0$, $\mathbf{P}(1) = \mathbf{P}_1$, $\mathbf{P'}(0) = \mathbf{P'}_0$, $\mathbf{P'}(1) = \mathbf{P'}_1$.

A nice feature of the Bézier curve is that it can be recursively split into segments of Bézier curves of the same order. Figure A.1 shows how a Bézier curve can be divided into two Bézier curve segments at $t = \frac{1}{2}$. The original control points are $\mathbf{P}_0$, $\mathbf{P}_a$, $\mathbf{P}_b$, $\mathbf{P}_1$. The new control points are given by

$$
\begin{aligned}
\mathbf{P_0}' &= \mathbf{P_0} \\
\mathbf{P_a}' &= (\mathbf{P_0} + \mathbf{P_a})/2 \\
\mathbf{P_b}' &= (\mathbf{P_0} + 2\mathbf{P_a} + \mathbf{P_b})/4 \\
\mathbf{P_1}' &= (\mathbf{P_0} + 3\mathbf{P_a} + 3\mathbf{P_b} + \mathbf{P_1})/8.
\end{aligned}
\tag{A.6}
$$

Switching $\mathbf{P_0}$ and $\mathbf{P_1}$, $\mathbf{P_a}$ and $\mathbf{P_b}$, we can find the other segment. With this feature and standard difference schemes to deal with the cubic polynomials, smooth curves can be very effectively generated by recursions involving only integer additions.

Figure A.2 shows the Bézier curve representation of our P velocity profile in the lowermost outer core (Chapter 3). The control points (given in Appendix B) are shown in solid dots, connected by the dotted line. Solid lines show the approximations to the Bézier curve using 1, 2, 4, 8, 16 segments progressively. They converge very quickly. The velocity profile is thus obtained by the end points (cross) of the split Bézier curves, the number of which depends on the desired precisions.

Bézier curves described above can be considered to be special cases of cubic B-spline curves, used more frequently in representing velocity perturbations [e.g. *Michelini and McEvilly*, 1991; *Tromp*, 1993]. The basic difference is that a cubic B-spline curve can have more than four control points. If the number of the control points of a cubic B-spline is four, they are convertible from one to another. If the number of the control points is larger than four, local control of shape is possible even within the curve (without affecting other parts of the same curve). In this case, more than one Bézier curves are required to represent the curve. Thus, cubic B-splines are more convenient in representing velocity perturbations, often rapid and involving changes of signs. However, for our purpose of modeling local velocity gradients and smooth variations, Bézier curves are sufficient and effective. The way that Bézier
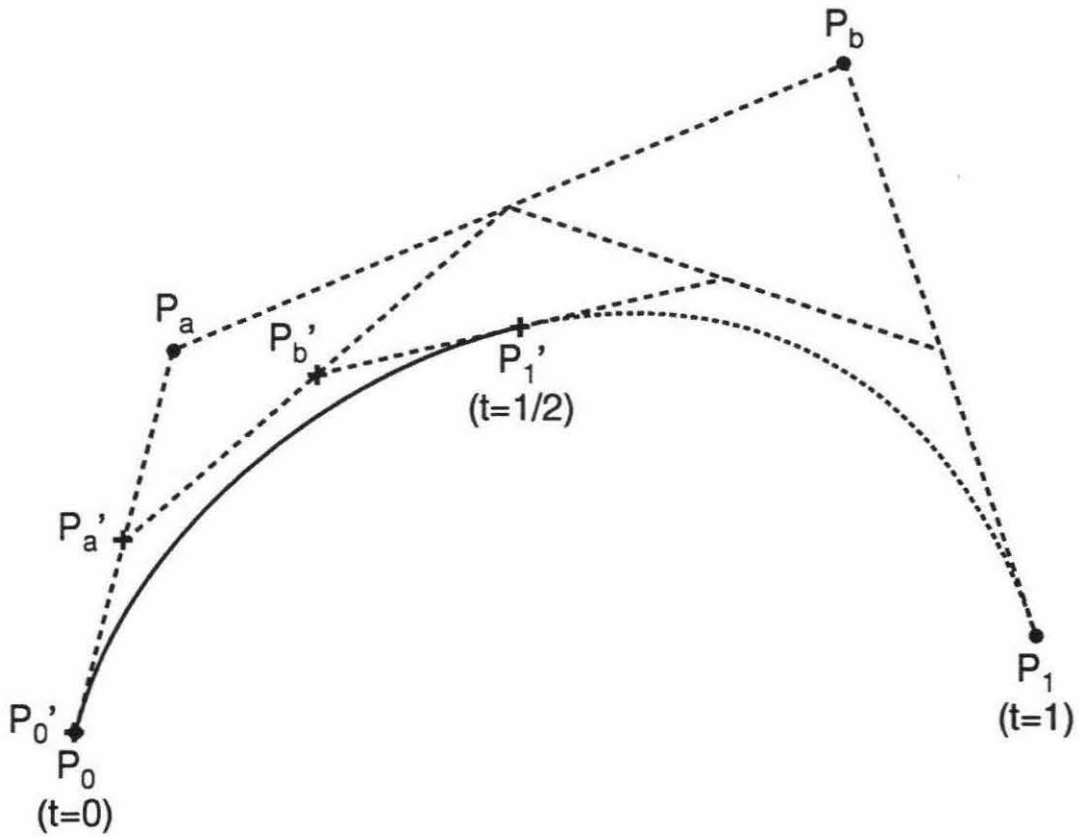
Figure A.1: A Bézier curve can be splitted into two Bézier curves by very simple relations (see text). This allows us to generate a Bézier curve very efficiently by recursions using computer.
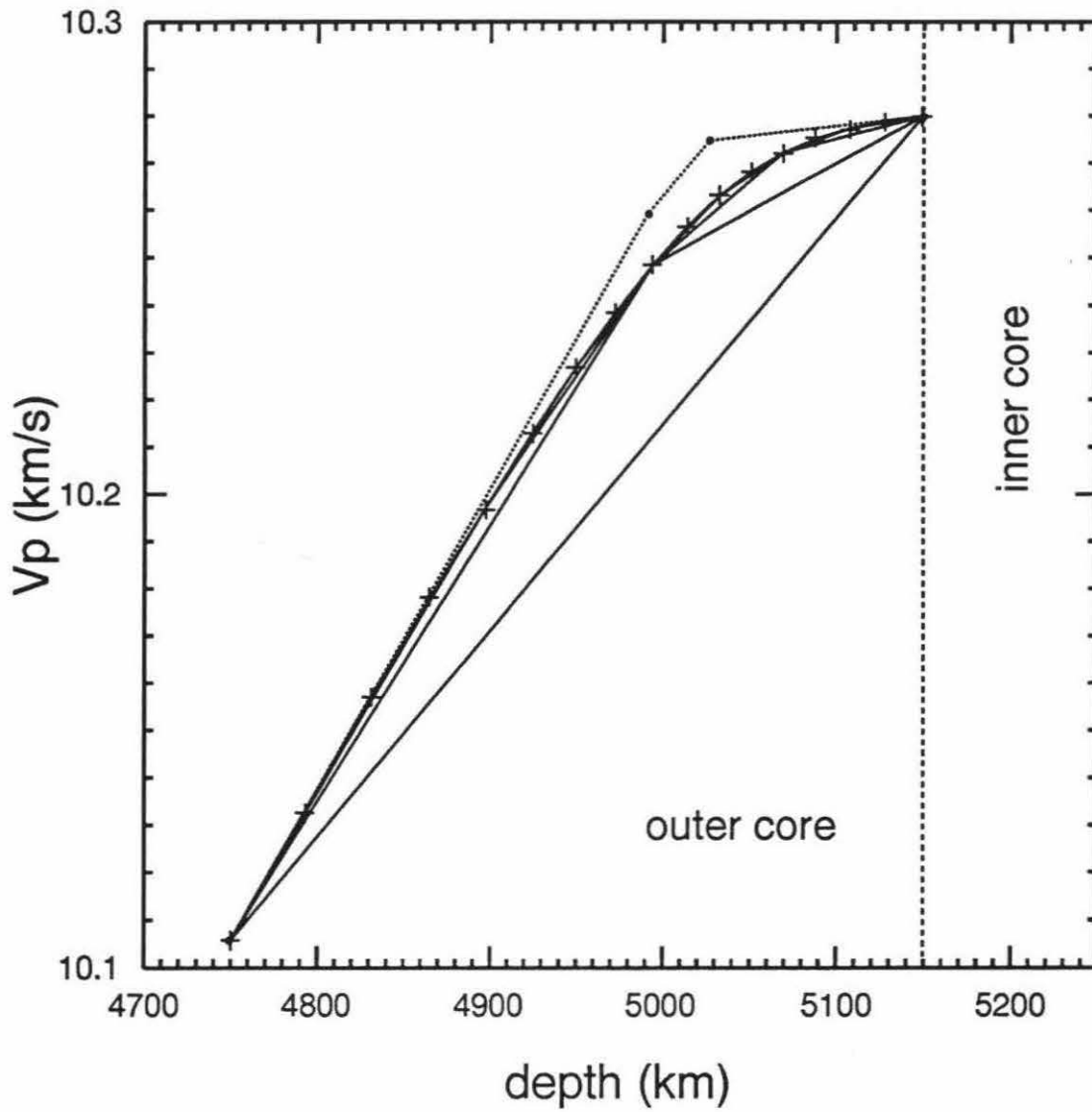
Figure A.2: The velocity profile from PREM2 model (Chapter 3) in the lowermost outer core represented by a Bézier curve. The velocity gradients are effectively controlled by the two middle control points.

curves determine the curve gradients at the end points is even more convenient for our construction of velocity models.

Appendix B

P Velocity of PREM2 Model

The P-wave velocity of the Earth's core model PREM2 is described in detail in Chapter 3. This table lists the P-wave velocity values of the model in about 10km intervals. The velocity at the lowermost outer core is calculated directly from a 3rd-order Bézier curve using the method described in Appendix A. The Bézier control points are as follows in (depth(km), velocity(km/s)):

$$
\begin{bmatrix} \mathbf{P}_0 \\ \mathbf{P}_a \\ \mathbf{P}_b \\ \mathbf{P}_1 \end{bmatrix} = \begin{bmatrix} (4749.5000, 10.1054) \\ (4991.3052, 10.2593) \\ (5026.7090, 10.2748) \\ (5149.5000, 10.2800) \end{bmatrix}.
$$

The polynomial represention of the model (with approximation at the lowermost outer core) is given in Table 3.1.

P velocity of PREM2

Radius, km	V_p, km/s	Radius, km	V_p, km/s	Radius, km	V_p, km/s	Radius, km	V_p, km/s
0.0	11.2622	331.5	11.2450	661.5	11.1936	991.5	11.1081
11.5	11.2622	341.5	11.2439	671.5	11.1915	1001.5	11.1049
21.5	11.2621	351.5	11.2428	681.5	11.1894	1011.5	11.1018
31.5	11.2620	361.5	11.2417	691.5	11.1872	1021.5	11.0999
41.5	11.2619	371.5	11.2406	701.5	11.1850	1031.5	11.0979
51.5	11.2618	381.5	11.2394	711.5	11.1828	1041.5	11.0959
61.5	11.2616	391.5	11.2382	721.5	11.1806	1051.5	11.0939
71.5	11.2614	401.5	11.2369	731.5	11.1783	1061.5	11.0919
81.5	11.2612	411.5	11.2357	741.5	11.1760	1071.5	11.0899
91.5	11.2609	421.5	11.2343	751.5	11.1737	1081.5	11.0879
101.5	11.2606	431.5	11.2330	761.5	11.1713	1091.5	11.0859
111.5	11.2603	441.5	11.2316	771.5	11.1689	1101.5	11.0839
121.5	11.2599	451.5	11.2302	781.5	11.1664	1111.5	11.0819
131.5	11.2595	461.5	11.2288	791.5	11.1640	1121.5	11.0799
141.5	11.2591	471.5	11.2273	801.5	11.1615	1131.5	11.0779
151.5	11.2586	481.5	11.2259	811.5	11.1590	1141.5	11.0759
161.5	11.2581	491.5	11.2243	821.5	11.1564	1151.5	11.0739
171.5	11.2576	501.5	11.2228	831.5	11.1538	1161.5	11.0720
181.5	11.2570	511.5	11.2212	841.5	11.1512	1171.5	11.0700
191.5	11.2565	521.5	11.2196	851.5	11.1485	1181.5	11.0680
201.5	11.2558	531.5	11.2179	861.5	11.1458	1191.5	11.0660
211.5	11.2552	541.5	11.2162	871.5	11.1431	1201.5	11.0640
221.5	11.2545	551.5	11.2145	881.5	11.1404	1211.5	11.0620
231.5	11.2538	561.5	11.2128	891.5	11.1376	1221.5	11.0600
241.5	11.2531	571.5	11.2110	901.5	11.1348	1221.5	10.2800
251.5	11.2523	581.5	11.2092	911.5	11.1319	1231.5	10.2795
261.5	11.2515	591.5	11.2073	921.5	11.1291	1241.5	10.2790
271.5	11.2506	601.5	11.2055	931.5	11.1262	1251.5	10.2783
281.5	11.2498	611.5	11.2036	941.5	11.1232	1261.5	10.2775
291.5	11.2489	621.5	11.2016	951.5	11.1203	1271.5	10.2766
301.5	11.2479	631.5	11.1997	961.5	11.1173	1281.5	10.2754
311.5	11.2470	641.5	11.1977	971.5	11.1142	1291.5	10.2739
321.5	11.2460	651.5	11.1957	981.5	11.1112	1301.5	10.2722

Table B.1: P-wave velocity values of the Earth's core model PREM2

P velocity of PREM2 (continued from previous page)

Radius, km	V_p, km/s	Radius, km	V_p, km/s	Radius, km	V_p, km/s	Radius, km	V_p, km/s
1311.5	10.2702	1641.5	10.0954	1971.5	9.8574	2301.5	9.5775
1321.5	10.2678	1651.5	10.0887	1981.5	9.8496	2311.5	9.5682
1331.5	10.2651	1661.5	10.0820	1991.5	9.8417	2321.5	9.5589
1341.5	10.2620	1671.5	10.0752	2001.5	9.8338	2331.5	9.5495
1351.5	10.2586	1681.5	10.0684	2011.5	9.8259	2341.5	9.5402
1361.5	10.2548	1691.5	10.0616	2021.5	9.8179	2351.5	9.5307
1371.5	10.2508	1701.5	10.0547	2031.5	9.8099	2361.5	9.5212
1381.5	10.2464	1711.5	10.0478	2041.5	9.8019	2371.5	9.5116
1391.5	10.2418	1721.5	10.0409	2051.5	9.7938	2381.5	9.5020
1401.5	10.2370	1731.5	10.0340	2061.5	9.7857	2391.5	9.4924
1411.5	10.2319	1741.5	10.0270	2071.5	9.7775	2401.5	9.4827
1421.5	10.2267	1751.5	10.0200	2081.5	9.7693	2411.5	9.4729
1431.5	10.2213	1761.5	10.0130	2091.5	9.7610	2421.5	9.4631
1441.5	10.2158	1771.5	10.0059	2101.5	9.7527	2431.5	9.4532
1451.5	10.2101	1781.5	9.9988	2111.5	9.7444	2441.5	9.4433
1461.5	10.2043	1791.5	9.9917	2121.5	9.7360	2451.5	9.4333
1471.5	10.1985	1801.5	9.9845	2131.5	9.7276	2461.5	9.4233
1481.5	10.1926	1811.5	9.9773	2141.5	9.7191	2471.5	9.4132
1491.5	10.1866	1821.5	9.9701	2151.5	9.7106	2481.5	9.4031
1501.5	10.1805	1831.5	9.9628	2161.5	9.7020	2491.5	9.3929
1511.5	10.1745	1841.5	9.9555	2171.5	9.6934	2501.5	9.3827
1521.5	10.1683	1851.5	9.9482	2181.5	9.6848	2511.5	9.3724
1531.5	10.1621	1861.5	9.9408	2191.5	9.6761	2521.5	9.3620
1541.5	10.1559	1871.5	9.9334	2201.5	9.6674	2531.5	9.3516
1551.5	10.1496	1881.5	9.9260	2211.5	9.6586	2541.5	9.3412
1561.5	10.1434	1891.5	9.9185	2221.5	9.6498	2551.5	9.3306
1571.5	10.1371	1901.5	9.9110	2231.5	9.6409	2561.5	9.3201
1581.5	10.1308	1911.5	9.9034	2241.5	9.6320	2571.5	9.3094
1591.5	10.1244	1921.5	9.8958	2251.5	9.6230	2581.5	9.2987
1601.5	10.1181	1931.5	9.8882	2261.5	9.6140	2591.5	9.2880
1611.5	10.1118	1941.5	9.8806	2271.5	9.6049	2601.5	9.2772
1621.5	10.1087	1951.5	9.8729	2281.5	9.5958	2611.5	9.2663
1631.5	10.1021	1961.5	9.8651	2291.5	9.5867	2621.5	9.2554

P velocity of PREM2 (continued from previous page)

Radius, km	V_p, km/s	Radius, km	V_p, km/s	Radius, km	V_p, km/s	Radius, km	V_p, km/s
2631.5	9.2444	2941.5	8.8730	3251.5	8.4353	3550.0	13.4943
2641.5	9.2334	2951.5	8.8600	3261.5	8.4200	3560.0	13.4921
2651.5	9.2223	2961.5	8.8469	3271.5	8.4046	3570.0	13.4899
2661.5	9.2111	2971.5	8.8337	3281.5	8.3891	3580.0	13.4877
2671.5	9.1999	2981.5	8.8204	3291.5	8.3735	3590.0	13.4855
2681.5	9.1886	2991.5	8.8071	3301.5	8.3579	3600.0	13.4833
2691.5	9.1773	3001.5	8.7937	3311.5	8.3422	3610.0	13.4811
2701.5	9.1659	3011.5	8.7803	3321.5	8.3263	3620.0	13.4789
2711.5	9.1544	3021.5	8.7668	3331.5	8.3105	3630.0	13.4767
2721.5	9.1429	3031.5	8.7532	3341.5	8.2945	3640.0	13.4745
2731.5	9.1313	3041.5	8.7395	3351.5	8.2784	3650.0	13.4723
2741.5	9.1196	3051.5	8.7258	3361.5	8.2623	3660.0	13.4701
2751.5	9.1079	3061.5	8.7119	3371.5	8.2461	3670.0	13.4680
2761.5	9.0961	3071.5	8.6981	3381.5	8.2298	3680.0	13.4658
2771.5	9.0843	3081.5	8.6841	3391.5	8.2134	3690.0	13.4636
2781.5	9.0724	3091.5	8.6701	3401.5	8.1969	3700.0	13.4614
2791.5	9.0604	3101.5	8.6560	3411.5	8.1804	3710.0	13.4592
2801.5	9.0484	3111.5	8.6418	3421.5	8.1638	3720.0	13.4570
2811.5	9.0363	3121.5	8.6275	3431.5	8.1471	3730.0	13.4548
2821.5	9.0241	3131.5	8.6132	3441.5	8.1303	3740.0	13.4526
2831.5	9.0119	3141.5	8.5988	3451.5	8.1134	3750.0	13.4504
2841.5	8.9996	3151.5	8.5843	3461.5	8.0964	3760.0	13.4482
2851.5	8.9872	3161.5	8.5698	3471.5	8.0793	3770.0	13.4460
2861.5	8.9748	3171.5	8.5551	3480.0	8.0648	3780.0	13.4438
2871.5	8.9623	3181.5	8.5404	3480.0	13.5097	3790.0	13.4416
2881.5	8.9498	3191.5	8.5257	3490.0	13.5075	3800.0	13.4394
2891.5	8.9371	3201.5	8.5108	3500.0	13.5053	3810.0	13.4372
2901.5	8.9245	3211.5	8.4959	3510.0	13.5031	3820.0	13.4350
2911.5	8.9117	3221.5	8.4808	3520.0	13.5009	3830.0	13.4328
2921.5	8.8989	3231.5	8.4657	3530.0	13.4987	3840.0	13.4306
2931.5	8.8860	3241.5	8.4506	3540.0	13.4965		

Appendix C

PKP Travel Times for PREM2 Model

The tables in the following pages list the travel times and the slowness ($dT/d\Delta$) of all branches of PKP waves (AB, BC, CD, DF). The PKP travel time curves for a surface focus can be found in Figure 3.2. Although no effort was made to fit the absolute travel, the travel time predictions from PREM2 are somewhat in between PREM [*Dziewonski and Anderson*, 1981] and IASP91 [*Kennet and Engdahl*, 1991]. For example, for a surface focus, the DF travel times are 0.91s later than PREM but 1.35s earlier than IASP91 at 120°. At 180° the DF travel times are 0.66s later than PREM but 1.01s earlier than IASP91.

PKP-AB

				focal depth (km)				
Δ (°)	0.	35.	70.	150.	250.	400.	550.	700.
				T (s) and dT/dΔ (s/deg)				
146.0	1181.13	1176.00	1171.85	1162.33	1150.64	1134.45	1119.79	1106.46
	3.82	3.83	3.84	3.87	3.90	3.95	3.99	4.04
147.0	1185.01	1179.88	1175.75	1166.25	1154.59	1138.44	1123.82	1110.54
	3.93	3.94	3.95	3.96	3.99	4.02	4.06	4.10
148.0	1188.98	1183.86	1179.73	1170.25	1158.61	1142.50	1127.91	1114.66
	4.01	4.01	4.02	4.04	4.06	4.08	4.12	4.15
149.0	1193.02	1187.91	1183.78	1174.32	1162.70	1146.61	1132.05	1118.83
	4.07	4.08	4.08	4.09	4.11	4.14	4.16	4.19
150.0	1197.12	1192.01	1187.89	1178.44	1166.83	1150.76	1136.23	1123.04
	4.12	4.13	4.13	4.14	4.16	4.18	4.20	4.23
151.0	1201.27	1196.16	1192.05	1182.60	1171.01	1154.96	1140.45	1127.28
	4.17	4.17	4.18	4.18	4.20	4.21	4.24	4.26
152.0	1205.45	1200.35	1196.24	1186.80	1175.22	1159.19	1144.70	1131.55
	4.21	4.21	4.21	4.22	4.23	4.25	4.27	4.28
153.0	1209.68	1204.58	1200.47	1191.04	1179.46	1163.45	1148.98	1135.85
	4.24	4.24	4.24	4.25	4.26	4.28	4.29	4.31
154.0	1213.93	1208.83	1204.73	1195.30	1183.74	1167.74	1153.28	1140.17
	4.27	4.27	4.27	4.28	4.29	4.30	4.32	4.33
155.0	1218.21	1213.12	1209.01	1199.60	1188.04	1172.05	1157.60	1144.51
	4.29	4.30	4.30	4.30	4.31	4.32	4.34	4.35
156.0	1222.52	1217.42	1213.32	1203.91	1192.36	1176.39	1161.95	1148.87
	4.32	4.32	4.32	4.33	4.33	4.34	4.36	4.37
157.0	1226.84	1221.75	1217.65	1208.25	1196.70	1180.74	1166.31	1153.25
	4.34	4.34	4.34	4.35	4.35	4.36	4.37	4.38
158.0	1231.19	1226.10	1222.00	1212.60	1201.06	1185.11	1170.69	1157.64
	4.36	4.36	4.36	4.36	4.37	4.38	4.39	4.40
159.0	1235.55	1230.47	1226.37	1216.97	1205.44	1189.49	1175.09	1162.04
	4.37	4.37	4.38	4.38	4.38	4.39	4.40	4.41
160.0	1239.93	1234.85	1230.75	1221.36	1209.83	1193.89	1179.50	1166.46
	4.39	4.39	4.39	4.39	4.40	4.41	4.41	4.42
161.0	1244.33	1239.24	1235.15	1225.76	1214.24	1198.31	1183.92	1170.89
	4.40	4.40	4.40	4.41	4.41	4.42	4.42	4.43
162.0	1248.74	1243.65	1239.56	1230.17	1218.65	1202.73	1188.35	1175.32
	4.41	4.41	4.42	4.42	4.42	4.43	4.43	4.44

(continued on next page)

Table C.1: Travel times of PKP-AB for PREM2 model

PKP-AB (continued from previous page)

Δ (°)	focal depth (km)							
	0.	35.	70.	150.	250.	400.	550.	700.
	T (s) and dT/dΔ (s/deg)							
163.0	1253.16	1248.07	1243.98	1234.60	1223.08	1207.16	1192.79	1179.77
	4.42	4.43	4.43	4.43	4.43	4.44	4.44	4.45
164.0	1257.59	1252.50	1248.41	1239.03	1227.52	1211.60	1197.23	1184.22
	4.43	4.44	4.44	4.44	4.44	4.45	4.45	4.46
165.0	1262.03	1256.94	1252.86	1243.48	1231.96	1216.06	1201.69	1188.69
	4.44	4.44	4.45	4.45	4.45	4.45	4.46	4.46
166.0	1266.47	1261.39	1257.31	1247.93	1236.42	1220.51	1206.15	1193.15
	4.45	4.45	4.45	4.46	4.46	4.46	4.47	4.47
167.0	1270.93	1265.85	1261.76	1252.39	1240.88	1224.98	1210.62	1197.63
	4.46	4.46	4.46	4.46	4.46	4.47	4.47	4.48
168.0	1275.39	1270.31	1266.23	1256.85	1245.35	1229.45	1215.09	1202.10
	4.47	4.47	4.47	4.47	4.47	4.47	4.48	4.48
169.0	1279.86	1274.78	1270.70	1261.32	1249.82	1233.92	1219.57	1206.58
	4.47	4.47	4.47	4.47	4.48	4.48	4.48	4.48
170.0	1284.33	1279.25	1275.17	1265.80	1254.30	1238.40	1224.05	1211.07
	4.48	4.48	4.48	4.48	4.48	4.48	4.48	4.49
171.0	1288.81	1283.73	1279.65	1270.28	1258.78	1242.89	1228.54	1215.56
	4.48	4.48	4.48	4.48	4.48	4.49	4.49	4.49
172.0	1293.29	1288.22	1284.13	1274.76	1263.26	1247.37	1233.03	1220.05
	4.48	4.48	4.48	4.49	4.49	4.49	4.49	4.49
173.0	1297.78	1292.70	1288.62	1279.25	1267.75	1251.86	1237.52	1224.54
	4.49	4.49	4.49	4.49	4.49	4.49	4.49	4.49
174.0	1302.27	1297.19	1293.11	1283.74	1272.24	1256.36	1242.01	1229.03
	4.49	4.49	4.49	4.49	4.49	4.49	4.49	4.49
175.0	1306.76	1301.68	1297.60	1288.23	1276.73	1260.85	1246.51	1233.53
	4.49	4.49	4.49	4.49	4.49	4.49	4.49	4.50
176.0	1311.25	1306.17	1302.09	1292.72	1281.23	1265.34	1251.00	1238.03
	4.49	4.49	4.49	4.49	4.49	4.50	4.50	4.50
177.0	1315.75	1310.67	1306.59	1297.22	1285.72	1269.84	1251.00	1238.03
	4.49	4.49	4.49	4.50	4.50	4.50	4.50	4.50
178.0	1320.24	1315.16	1311.08	1301.71	1290.22	1269.84	1251.00	1238.03
	4.50	4.50	4.50	4.50	4.50	4.50	4.50	4.50
	4.50	4.50	4.50	4.50	4.50	4.50	4.50	4.50
	4.50	4.50	4.50	4.50	4.50	4.50	4.50	4.50

PKP-BC

Δ (°)	focal depth (km)							
	0.	35.	70.	150.	250.	400.	550.	700.
	T (s) and dT/dΔ (s/deg)							
146.0	1180.44	1175.25	1171.03	1161.33	1149.40	1132.77	1117.54	1103.52
	2.98	2.96	2.95	2.92	2.88	2.82	2.80	2.73
147.0	1183.32	1178.12	1173.89	1164.17	1152.22	1135.54	1120.26	1106.18
	2.80	2.80	2.80	2.80	2.79	2.70	2.65	2.59
148.0	1186.07	1180.86	1176.62	1166.88	1154.90	1138.17	1122.84	1108.71
	2.67	2.66	2.65	2.63	2.60	2.56	2.52	2.48
149.0	1188.67	1183.45	1179.20	1169.44	1157.43	1140.67	1125.31	1111.14
	2.53	2.52	2.52	2.50	2.48	2.45	2.42	2.38
150.0	1191.14	1185.92	1181.66	1171.89	1159.86	1143.08	1127.68	1113.49
	2.42	2.42	2.41	2.40	2.38	2.36	2.34	2.31
151.0	1193.51	1188.29	1184.03	1174.25	1162.21	1145.40	1129.99	1115.77
	2.34	2.33	2.33	2.32	2.31	2.29	2.27	2.25
152.0	1195.82	1190.59	1186.33	1176.54	1164.49	1147.66	1132.23	1117.99
	2.27	2.27	2.27	2.26	2.25	2.24	2.22	2.20
153.0	1198.06	1192.83	1188.56	1178.77	1166.71	1149.87	1134.43	1120.17
	2.22	2.21	2.21	2.20	2.20	2.18	2.17	2.15
154.0	1200.25	1195.02	1190.75	1180.95	1168.88	1152.03	1136.57	1122.29
	2.16	2.16	2.16	2.15	2.14	2.13	2.11	2.10
155.0	1202.39	1197.15	1192.88	1183.07	1168.88	1152.03	1136.57	1122.29
	2.11	2.11	2.10	2.10	2.14	2.13	2.11	2.10

Table C.2: Travel times of PKP-BC for PREM2 model

PKP-CD

Δ (°)	focal depth (km)							
	0.	35.	70.	150.	250.	400.	550.	700.
	T (s) and dT/dΔ (s/deg)							
120.0	1131.09	1125.85	1121.57	1111.75	1099.65	1082.76	1067.26	1052.94
	1.96	1.96	1.96	1.97	1.97	1.97	1.97	1.97
121.0	1133.06	1127.82	1123.54	1113.72	1101.62	1084.73	1069.23	1054.91
	1.97	1.97	1.97	1.97	1.97	1.97	1.98	1.98
122.0	1135.03	1129.79	1125.51	1115.69	1103.60	1086.71	1071.21	1056.89
	1.98	1.98	1.98	1.98	1.98	1.98	1.98	1.98
123.0	1137.01	1131.77	1127.49	1117.67	1105.58	1088.69	1073.19	1058.88
	1.98	1.98	1.98	1.98	1.98	1.99	1.99	1.99
124.0	1139.00	1133.76	1129.48	1119.66	1107.57	1090.68	1075.18	1060.87
	1.99	1.99	1.99	1.99	1.99	1.99	1.99	1.99
125.0	1140.99	1135.75	1131.47	1121.65	1109.56	1092.67	1077.18	1062.87
	1.99	1.99	1.99	1.99	2.00	2.00	2.00	2.00
126.0	1142.98	1137.74	1133.47	1123.65	1111.56	1094.67	1079.18	1064.87
	2.00	2.00	2.00	2.00	2.00	2.00	2.00	2.00
127.0	1144.98	1139.75	1135.47	1125.65	1113.56	1096.68	1081.18	1066.88
	2.00	2.00	2.00	2.01	2.01	2.01	2.01	2.01
128.0	1146.99	1141.75	1137.48	1127.66	1115.57	1098.69	1083.19	1068.89
	2.01	2.01	2.01	2.01	2.01	2.01	2.01	2.01
129.0	1149.00	1143.76	1139.49	1129.67	1117.58	1100.70	1085.21	1070.91
	2.01	2.01	2.01	2.01	2.02	2.02	2.02	2.02

(continued on next page)

Table C.3: Travel times of PKP-CD (PKiKP) for PREM2 model

PKP-CD (continued from previous page)

Δ (°)	focal depth (km)							
	0.	35.	70.	150.	250.	400.	550.	700.
	T (s) and dT/dΔ (s/deg)							
130.0	1151.02	1145.78	1141.50	1131.69	1119.60	1102.72	1087.23	1072.93
	2.02	2.02	2.02	2.02	2.02	2.02	2.02	2.02
131.0	1153.04	1147.80	1143.52	1133.71	1121.62	1104.74	1089.25	1074.95
	2.02	2.02	2.02	2.02	2.02	2.03	2.03	2.03
132.0	1155.06	1149.83	1145.55	1135.73	1123.65	1106.77	1091.28	1076.98
	2.03	2.03	2.03	2.03	2.03	2.03	2.03	2.03
133.0	1157.09	1151.86	1147.58	1137.76	1125.68	1108.80	1093.31	1079.02
	2.03	2.03	2.03	2.03	2.03	2.03	2.03	2.04
134.0	1159.12	1153.89	1149.61	1139.80	1127.71	1110.84	1095.35	1081.05
	2.03	2.03	2.03	2.04	2.04	2.04	2.04	2.04
135.0	1161.16	1155.92	1151.65	1141.83	1129.75	1112.87	1097.39	1083.09
	2.04	2.04	2.04	2.04	2.04	2.04	2.04	2.04
136.0	1163.20	1157.96	1153.69	1143.87	1131.79	1114.92	1099.43	1085.14
	2.04	2.04	2.04	2.04	2.04	2.04	2.04	2.05
137.0	1165.24	1160.01	1155.73	1145.92	1133.84	1116.96	1101.48	1087.19
	2.04	2.05	2.05	2.05	2.05	2.05	2.05	2.05
138.0	1167.29	1162.06	1157.78	1147.97	1135.88	1119.01	1103.53	1089.24
	2.05	2.05	2.05	2.05	2.05	2.05	2.05	2.05
139.0	1169.34	1164.10	1159.83	1150.02	1137.93	1121.06	1105.58	1091.29
	2.05	2.05	2.05	2.05	2.05	2.05	2.05	2.05
140.0	1171.39	1166.16	1161.88	1152.07	1139.99	1123.12	1107.63	1093.34
	2.05	2.05	2.05	2.05	2.05	2.06	2.06	2.06

PKP-DF

| | focal depth (km) | | | | | | | |
| Δ (°) | 0. | 35. | 70. | 150. | 250. | 400. | 550. | 700. |
	T (s) and dT/dΔ (s/deg)							
120.0	1130.98	1125.74	1121.46	1111.64	1099.54	1082.63	1067.12	1052.78
	1.93	1.93	1.93	1.92	1.92	1.92	1.92	1.92
121.0	1132.91	1127.67	1123.39	1113.56	1101.46	1084.56	1069.04	1054.71
	1.92	1.92	1.92	1.92	1.92	1.92	1.92	1.92
122.0	1134.83	1129.59	1125.31	1115.48	1103.38	1086.48	1070.96	1056.63
	1.92	1.92	1.92	1.92	1.92	1.92	1.92	1.92
123.0	1136.75	1131.51	1127.23	1117.40	1105.30	1088.40	1072.88	1058.55
	1.92	1.92	1.92	1.92	1.92	1.92	1.92	1.92
124.0	1138.67	1133.43	1129.15	1119.32	1107.22	1090.32	1074.80	1060.47
	1.92	1.92	1.92	1.92	1.92	1.92	1.92	1.92
125.0	1140.59	1135.35	1131.07	1121.24	1109.14	1092.24	1076.72	1062.38
	1.92	1.92	1.92	1.92	1.92	1.92	1.91	1.91
126.0	1142.51	1137.27	1132.99	1123.16	1111.06	1094.15	1078.63	1064.30
	1.91	1.91	1.91	1.91	1.91	1.91	1.91	1.91
127.0	1144.42	1139.18	1134.90	1125.07	1112.97	1096.06	1080.54	1066.21
	1.91	1.91	1.91	1.91	1.91	1.91	1.91	1.91
128.0	1146.33	1141.09	1136.81	1126.98	1114.88	1097.97	1082.45	1068.11
	1.91	1.91	1.91	1.91	1.91	1.91	1.91	1.90
129.0	1148.24	1143.00	1138.72	1128.89	1116.78	1099.88	1084.35	1070.01
	1.90	1.90	1.90	1.90	1.90	1.90	1.90	1.90
130.0	1150.14	1144.90	1140.62	1130.79	1118.68	1101.78	1086.25	1071.91
	1.90	1.90	1.90	1.90	1.90	1.90	1.90	1.90
131.0	1152.04	1146.80	1142.52	1132.68	1120.58	1103.67	1088.15	1073.80
	1.90	1.90	1.90	1.89	1.89	1.89	1.89	1.89
132.0	1153.93	1148.69	1144.41	1134.58	1122.47	1105.56	1090.03	1075.69
	1.89	1.89	1.89	1.89	1.89	1.89	1.89	1.88
133.0	1155.82	1150.58	1146.29	1136.46	1124.36	1107.44	1091.92	1077.57
	1.88	1.88	1.88	1.88	1.88	1.88	1.88	1.88
134.0	1157.70	1152.46	1148.17	1138.34	1126.24	1109.32	1093.79	1079.44
	1.88	1.88	1.88	1.88	1.88	1.87	1.87	1.87

(continued on next page)

Table C.4: Travel times of PKP-DF (PKIKP) for PREM2 model

PKP-DF (continued from previous page)

Δ (°)	focal depth (km)							
	0.	35.	70.	150.	250.	400.	550.	700.
	T (s) and dT/dΔ (s/deg)							
135.0	1159.57	1154.33	1150.05	1140.21	1128.11	1111.19	1095.66	1081.31
	1.87	1.87	1.87	1.87	1.87	1.87	1.86	1.86
136.0	1161.44	1156.20	1151.91	1142.08	1129.97	1113.05	1097.52	1083.17
	1.86	1.86	1.86	1.86	1.86	1.86	1.85	1.85
137.0	1163.30	1158.05	1153.77	1143.93	1131.82	1114.90	1099.37	1085.01
	1.85	1.85	1.85	1.85	1.85	1.85	1.84	1.84
138.0	1165.14	1159.90	1155.62	1145.78	1133.67	1116.75	1101.21	1086.85
	1.84	1.84	1.84	1.84	1.84	1.84	1.83	1.83
139.0	1166.98	1161.74	1157.45	1147.61	1135.50	1118.58	1103.03	1088.67
	1.83	1.83	1.83	1.83	1.83	1.82	1.82	1.82
140.0	1168.80	1163.56	1159.27	1149.44	1137.32	1120.39	1104.85	1090.48
	1.82	1.82	1.82	1.82	1.81	1.81	1.81	1.80
141.0	1170.62	1165.37	1161.08	1151.24	1139.13	1122.20	1106.65	1092.27
	1.80	1.80	1.80	1.80	1.80	1.80	1.79	1.79
142.0	1172.41	1167.17	1162.88	1153.04	1140.92	1123.98	1108.43	1094.05
	1.79	1.79	1.79	1.78	1.78	1.78	1.77	1.77
143.0	1174.19	1168.94	1164.66	1154.81	1142.69	1125.75	1110.19	1095.81
	1.77	1.77	1.77	1.77	1.76	1.76	1.76	1.75
144.0	1175.95	1170.70	1166.41	1156.57	1144.44	1127.50	1111.94	1097.55
	1.75	1.75	1.75	1.75	1.74	1.74	1.73	1.73
145.0	1177.69	1172.44	1168.15	1158.30	1146.18	1129.23	1113.66	1099.27
	1.73	1.73	1.73	1.73	1.72	1.72	1.71	1.71
146.0	1179.41	1174.16	1169.87	1160.02	1147.89	1130.94	1115.36	1100.96
	1.71	1.70	1.70	1.70	1.70	1.69	1.69	1.68
147.0	1181.10	1175.85	1171.56	1161.71	1149.57	1132.62	1117.04	1102.63
	1.68	1.68	1.68	1.68	1.67	1.67	1.66	1.65
148.0	1182.76	1177.51	1173.22	1163.37	1151.23	1134.27	1118.68	1104.27
	1.65	1.65	1.65	1.65	1.64	1.64	1.63	1.62
149.0	1184.40	1179.15	1174.86	1165.00	1152.86	1135.89	1120.30	1105.88
	1.62	1.62	1.62	1.62	1.61	1.61	1.60	1.59

PKP-DF (continued from previous page)

Δ (°)	focal depth (km)							
	0.	35.	70.	150.	250.	400.	550.	700.
	T (s) and dT/dΔ (s/deg)							
150.0	1186.01	1180.76	1176.46	1166.60	1154.46	1137.48	1121.88	1107.45
	1.59	1.59	1.58	1.58	1.58	1.57	1.56	1.55
151.0	1187.57	1182.32	1178.02	1168.16	1156.01	1139.03	1123.42	1108.98
	1.55	1.54	1.54	1.54	1.54	1.53	1.52	1.51
152.0	1189.10	1183.84	1179.55	1169.68	1157.53	1140.54	1124.92	1110.47
	1.50	1.50	1.50	1.50	1.49	1.49	1.48	1.47
153.0	1190.58	1185.33	1181.03	1171.16	1159.00	1142.00	1126.37	1111.91
	1.46	1.46	1.46	1.46	1.45	1.44	1.44	1.43
154.0	1192.02	1186.77	1182.46	1172.59	1160.43	1143.42	1127.79	1113.32
	1.42	1.42	1.42	1.41	1.41	1.40	1.39	1.38
155.0	1193.42	1188.16	1183.86	1173.98	1161.82	1144.80	1129.16	1114.68
	1.37	1.37	1.37	1.37	1.36	1.36	1.35	1.34
156.0	1194.77	1189.51	1185.20	1175.32	1163.15	1146.13	1130.48	1115.99
	1.33	1.32	1.32	1.32	1.32	1.31	1.30	1.29
157.0	1196.07	1190.81	1186.50	1176.62	1164.45	1147.42	1131.76	1117.26
	1.28	1.28	1.27	1.27	1.27	1.26	1.25	1.24
158.0	1197.32	1192.06	1187.75	1177.87	1165.69	1148.65	1132.98	1118.48
	1.23	1.23	1.23	1.22	1.22	1.21	1.20	1.19
159.0	1198.53	1193.26	1188.96	1179.06	1166.88	1149.84	1134.16	1119.64
	1.18	1.18	1.17	1.17	1.17	1.16	1.15	1.14
160.0	1199.68	1194.41	1190.10	1180.21	1168.02	1150.97	1135.29	1120.76
	1.13	1.12	1.12	1.12	1.12	1.11	1.10	1.09
161.0	1200.78	1195.51	1191.20	1181.30	1169.11	1152.06	1136.36	1121.83
	1.07	1.07	1.07	1.07	1.06	1.06	1.05	1.04
162.0	1201.83	1196.56	1192.25	1182.35	1170.15	1153.09	1137.39	1122.85
	1.02	1.02	1.02	1.01	1.01	1.00	1.00	0.99
163.0	1202.82	1197.55	1193.24	1183.33	1171.14	1154.07	1138.36	1123.81
	0.97	0.97	0.96	0.96	0.96	0.95	0.94	0.94
164.0	1203.76	1198.49	1194.17	1184.27	1172.07	1154.99	1139.28	1124.72
	0.91	0.91	0.91	0.91	0.90	0.90	0.89	0.88

214

PKP-DF (continued from previous page)

Δ (°)	0.	35.	70.	focal depth (km) 150.	250.	400.	550.	700.
				T (s) and dT/dΔ (s/deg)				
	0.86	0.86	0.85	0.85	0.85	0.84	0.84	0.83
166.0	1205.47	1200.20	1195.88	1185.97	1173.76	1156.68	1140.95	1126.38
	0.80	0.80	0.80	0.80	0.79	0.79	0.78	0.78
167.0	1206.24	1200.97	1196.65	1186.74	1174.53	1157.44	1141.71	1127.13
	0.75	0.74	0.74	0.74	0.74	0.73	0.73	0.72
168.0	1206.96	1201.69	1197.37	1187.45	1175.24	1158.14	1142.41	1127.82
	0.69	0.69	0.69	0.69	0.68	0.68	0.67	0.67
169.0	1207.62	1202.35	1198.03	1188.11	1175.89	1158.79	1143.05	1128.46
	0.63	0.63	0.63	0.63	0.63	0.62	0.62	0.61
170.0	1208.23	1202.95	1198.63	1188.71	1176.49	1159.39	1143.64	1129.05
	0.58	0.57	0.57	0.57	0.57	0.57	0.56	0.56
171.0	1208.77	1203.50	1199.18	1189.26	1177.03	1159.93	1144.18	1129.58
	0.52	0.52	0.52	0.52	0.51	0.51	0.51	0.50
172.0	1209.26	1203.99	1199.67	1189.74	1177.52	1160.41	1144.65	1130.05
	0.46	0.46	0.46	0.46	0.46	0.45	0.45	0.45
173.0	1209.69	1204.42	1200.10	1190.17	1177.95	1160.83	1145.08	1130.47
	0.40	0.40	0.40	0.40	0.40	0.40	0.39	0.39
174.0	1210.07	1204.79	1200.47	1190.55	1178.32	1161.20	1145.44	1130.83
	0.35	0.35	0.35	0.34	0.34	0.34	0.34	0.34
175.0	1210.39	1205.11	1200.79	1190.86	1178.63	1161.52	1145.75	1131.14
	0.29	0.29	0.29	0.29	0.29	0.28	0.28	0.28
176.0	1210.65	1205.37	1201.05	1191.12	1178.89	1161.77	1146.01	1131.39
	0.23	0.23	0.23	0.23	0.23	0.23	0.23	0.22
177.0	1210.85	1205.57	1201.25	1191.32	1179.09	1161.97	1146.20	1131.59
	0.17	0.17	0.17	0.17	0.17	0.17	0.17	0.17
178.0	1210.99	1205.72	1201.39	1191.47	1179.24	1162.11	1146.35	1131.73
	0.12	0.12	0.12	0.12	0.11	0.11	0.11	0.11
179.0	1211.08	1205.80	1201.48	1191.55	1179.32	1162.20	1146.43	1131.81
	0.06	0.06	0.06	0.06	0.06	0.06	0.06	0.06
180.0	1211.11	1205.83	1201.51	1191.58	1179.35	1162.23	1146.46	1131.84
	0.00	0.00	0.00	0.00	0.00	0.00	0.00	0.00